ISSN 1068-3755, Surface Engineering and Applied Electrochemistry, 2008, Vol. 44, No. 2, pp. 81–86. © Allerton Press, Inc., 2008.
Original Russian Text © V.D. Shkilev, A.N. Adamchuk, V.G. Nedioglo, 2008, published in Elektronnaya Obrabotka Materialov, 2008, No. 2, pp. 4–10.

ELECTRICAL PRECISION TREATMENT OF MATERIALS

Electrodischarge Technology for Protecting Especially Important Documents

V. D. Shkilev, A. N. Adamchuk, and V. G. Nedioglo

Ministry of Information Development, ul. Pushkina 42, Kishinev, MD-2012 Republic of Moldova

Received November 5, 2007

Abstract—Electrodigital technology for formation of an individual matrix that allows building a database by combining the digital and wave approaches in a new mode is offered. It is shown that the electrodigital identification, having all the attributes of quantum identification, basically is not subject to counterfeiting and can be used as a protective technology for production of important documents including national currencies.

DOI: 10.3103/S1068375508020014

INTRODUCTION

Minimization of finance losses and dangers to the safety of the state caused by such phenomena as corruption, falsification of documents, production of unaccounted for and counterfeit goods and contraband, and illegal export and illegal migration using forged documents requires introducing information technologies into practice that can help to improve the quality of management in industrial and social spheres.

The experience of experts–criminalists shows that a text on an institution blank, along with a signature and seal, can be forged by malefactors who employ modern methods of computer graphics. Virtual documents can easily be protected with the assistance of a so-called electrodigital signature. Paper ones are protected using traditional methods such as special polygraphic products (excise marks and exacting blanks) and various kinds of holograms (unigrams), latent raster images, and markings utilizing machine-readable ordinal or occasional numbers. However, all these measures don't lead to a noticeable reduction of the damage caused by offences.

The modern level of state document circulation can be achieved only in the case when there is provided uniformity in the protection of documents—both virtual and analog (paper) ones. For that, it is necessary not only to impart every paper document, as a marketable product unit, with its own unique identification code assisting the control of its travel route during its whole life but also to safeguard the numeric code included into a database together with some unique matrix that can not be repeated twice. There exists such a faulty system of views that if some man makes anything another one can always repeat the same. Therefore, there appears the statement that it is impossible to construct a unique identifier that can not be replicated by the shadow economy. The necessity to create such a unique identifier is discussed from the point of view of philosophy in [1], and, in [2], there is presented the description of a patent permitting to one to obtain the best informational protection of an individual numeric code with the help of electrodischarge technology.

Such technology somewhat resembles new approaches to biometric identification [3], when, instead of typical patterns (papillary lines) on finger skin (classic dactyloscopy), another individual feature (location of skin pores situated between these lines) is introduced into the database. Unlike such approaches requiring the use of additional information programs removing distortion caused by the possible rotational deformation at the skin extension, the electrodischarge method of spot (pore) tracing on a metal or paper surface has no such drawbacks. When such an approach is used, the database is built not on graphical information but only taking into account the parameters (coordinates, area, shape, etc) of the obtained spots. Identification with a database consisting of millions of electrodischarge pictures can be carried out within a few seconds.

EXPERIMENTAL RESULTS

The nonreproductivity (individuality) of a matrix obtained with the help of electric discharges is examined in this work. The conduction scheme of the experiment is extraordinary simple (Fig. 1). Small holes are pierced in a piece of paper by the electrodischarge method. Then, the obtained specimens are scanned using the openings by an ordinary scanner with resolution of 600 dpi and kept in the JPG format. The pictures are read with a computer, and there is calculated the relative area of the pierced holes on the ring

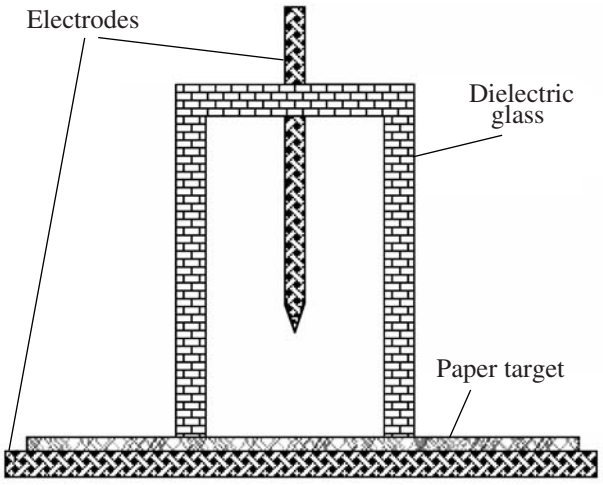

Fig. 1. The experiment conduction scheme.

with the matched diameter (see the mathematical treatment of the obtained results). The outcome is presented in the form of the area versus a ring number diagram.

Primary experiments carried out for the scheme with a positive point and a negative plane and vice versa showed that utilization of a high direct voltage source isn't optimum to obtain an individual pattern using paper, probably, owing to the accumulation of charges on the dielectric glass. Therefore, all the following information concerns a source with a high alternating voltage. The results obtained with the help of sphere-plane electrodes are not optimum as well (the number of pierced holes in the paper is many times less than the number of discharges; in other words, the discharge often follows the path of the previous discharge and doesn't cause the individual matrix complexification). The best results have been obtained with the help of point-plane electrodes. The majority of the experimental works in this sphere [4] describe the peculiarities of physical processes in the interelectrode space; the informational abilities of these technologies [2] haven't attracted sufficient attention of investigators.

To facilitate scanning the places of electric breakdown, there is printed a black circle on the paper. Inside this circle (hypothetically, the document of exacting detail being created), there is also drawn the individual numeric code. If this individual numeric code is absent it is impossible to build the database because of the insurmountable mathematical obstacles occurring at the discernment of the images. The database is constructed as a result of combining numeric and wave (individual matrix) information. The document is found in the database in accordance with its individual numeric code, and its authenticity is tested using the individual matrix. At electric discharge, there not only appears a hole in the paper (to register it with the help of a normal scanner is rather difficult) but also there occurs the evaporation of the conducting black paint (the estimation of the electron component photon emission density confirms this possibility) thus eliminating all the technological problems of recording.

Twelve targets were employed in every interelectrode space with a step of 2.5 mm for the purpose of statistics. A typical document containing an individual numeric code (generated, as a rule, with the help of a random number generator) and an individual picture obtained with the assistance of electric breakdowns shows up in the following way:

With the interelectrode space being small (the point-to-plane distance is 5 mm), the number of electrodischarge spots doesn't exceed 20–25. The quantity of the discharges is about 4000 as recorded with the aid of an oscillograph. This discordance is attributable to the fact that a discharge often hits a hole made by previous discharges. The identification mark treatment time is maintained constant and is about sixty seconds. If the interelectrode space increases up to 7.5 mm, the number of electrodischarge spots in the paper rises sharply. In Fig. 3, there is presented a typical individual picture (without a numeric code) for a gap of 7.5 mm; it is seen that not only the picture as a whole is unique but every spot as well.

Here is a short digression into the history of the physical experiment that resulted in the origin of quantum mechanics. It was T. Yung who observed the interference of light in two slits. C.D. Davison and L.H. Dgermer (and, independently, D.P. Thomson) viewed the diffraction of electrons on nickel single crystals (later on, these scientists received a Nobel prize in 1937 for these investigations). The nature of the observed periodic peaks was similar to the character of the peaks in the two-slit experiment.

Such tests were iteratively repeated, and hypotheses on the interaction of electrons were examined when electrons were "piecemeal" emitted with a time interval of 30 minutes, but the result remained the same; namely, there appeared an interferential pattern.

Physicists began to carry out experiments with larger particles. In 2003, there was conducted a classic two-slit experiment [5], and the interferential pattern on the simultaneous passage through two slits of a very big (for quantum measures) molecule of tetraphenylporphyrin was obtained. What is the principal distinction of our experiment from the previous ones? At first glance, there are no "slits." There is normal air under normal conditions between the source of the electrons and the target. However, there are always some fluctuations of the electric conductivity (tiny airborne particles, ionized zones of space radiation, nonuniformities of temperature and moisture, etc.) acting as "slits" in the

Fig. 2. Document with individual numeric code protection using the electrodischarge procedure.

test. Electron clusters (electron avalanches consisting of an infinite number of electrons) are analyzed instead of single electrons. Furthermore, we receive an interferential pattern again.

The mechanism of the spark passage generation (and, hence, of the spark discharge origin) is generally explained by the streamer theory of the gas electric breakdown. According to this theory, under certain conditions, there arise streamers (dimly luminous thin branched passages containing gas ionized atoms and segregated free electrons) from electron avalanches occurring in the discharge gap electric field. Lengthening, the streamers overlap the discharge gap and join the electrodes with uninterrupted conducting filaments; electric discharge, accompanied by a brightly luminous passage and sound effects, forms in the most developed streamer.

We are not going to state that the electric discharge hitting a particular target section (recorded with the aid of various equipment) behaves as a quantum particle,

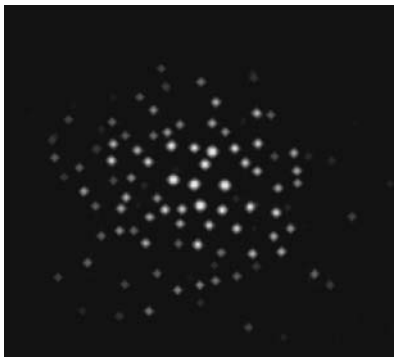

Fig. 3. Typical individual picture experimentally obtained using electrodischarge technology.

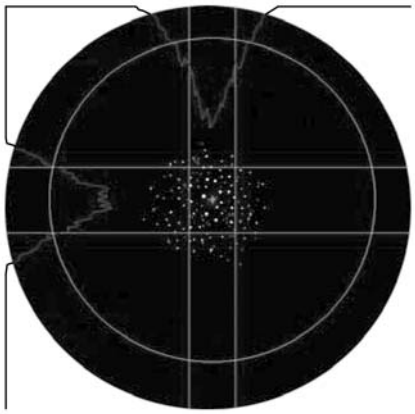

Fig. 4. Algorithm for mass center search.

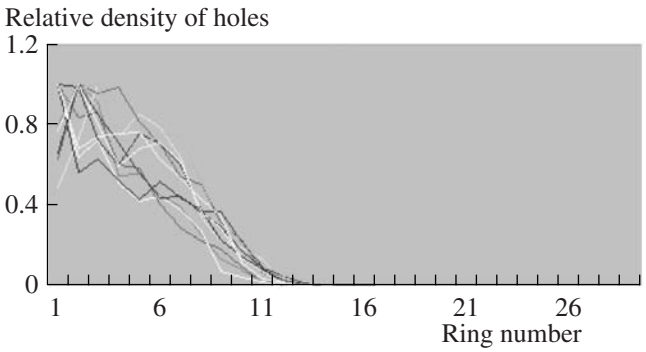

Fig. 5. Hole density distribution with a 5 mm gap.

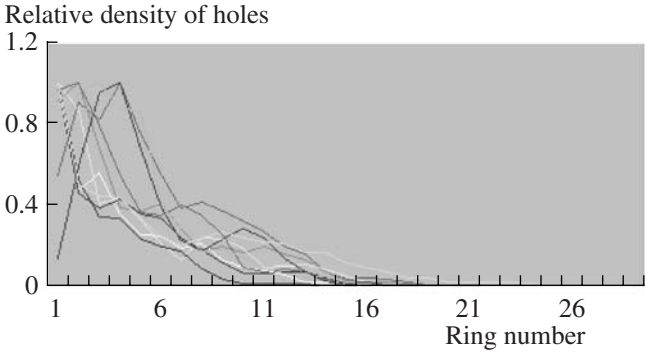

Fig. 6. Hole density distribution with a 7.5 mm gap.

but we can suppose that the preconduction streamer (which is impossible to register experimentally) is generated according to wave principles; namely, this fact ensures the interferential pattern on the matrix. The streamer, though, participates in the primary location of those "slits" through which the discharge will pass. The wave nature of the processes taking place at streamer discharge is noted by many authors [6-7]. The discharge itself develops along the trajectory formed previously by a streamer and behaves as a classic solid.

For state coherence demolition and interferential pattern disappearance, only the presence of information on which "slit" the streamer passed through is important. If there is no such data (or we have no such information), the interferential pattern will always arise on the target irrespective of whether a single electron flies and hits the target during 30 minutes or hundreds of millions of electrons do the same simultaneously as an electron avalanche. In other words, an interferential pattern can appear both in the study of microcosm phenomena (motions of a single electron through two "slits") and in the investigation of macrocosm phenomena (motions of an electron avalanche through many "slits," which was shown using the example of electrodischarge identification technology).

MATHEMATICAL TREATMENT OF THE OBTAINED RESULTS

To treat the obtained patterns, there has been written a program performing the following operations to imitate the classic experiment with the aim to verify Maxwell distributions.

Searching for the distribution center of the holes in order to correct the specimen's inaccurate centration at the breakdown in the device is carried out according to the following algorithm:

a) At first, the image projection on the X and Y axes is calculated.

b) Then, the point whose coordinates are the central values of the width interval in the maximum half on each axis is taken as the center.

Figure 4 shows that the physical center (the needle electrode is mounted over it) differs from the geometrical one, but the estimation of the needle electrode position error with respect to the target geometrical center doesn't go beyond the circle with a diameter of 1.5 mm allowing to us to state that the tip effects are minimum.

We separate the pattern into the mentioned number of rings with regard to the center found. In the calculation of the relative area of the holes on the ring with the given radius, we take into account not the spot as a unit but its contribution to the total area of the relevant ring spots.

We then output the results into a file for further manipulations.

The curves plotted for the obtained data are presented in the next figures. Every curve shows the result

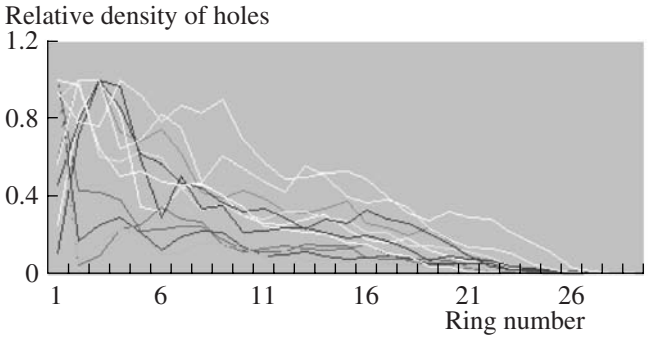

Fig. 7. Hole density distribution with a 10 mm gap.

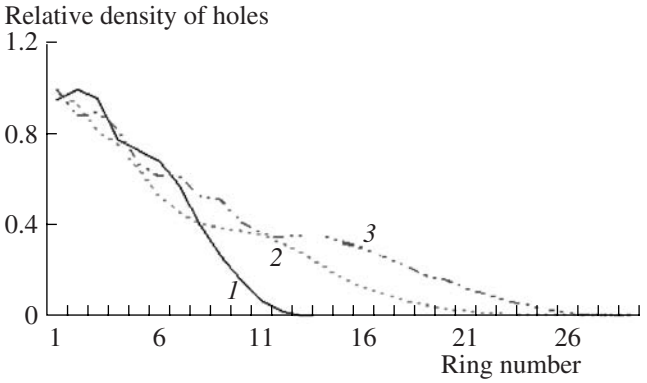

Fig. 8. The average distribution of the hole density at different gaps.

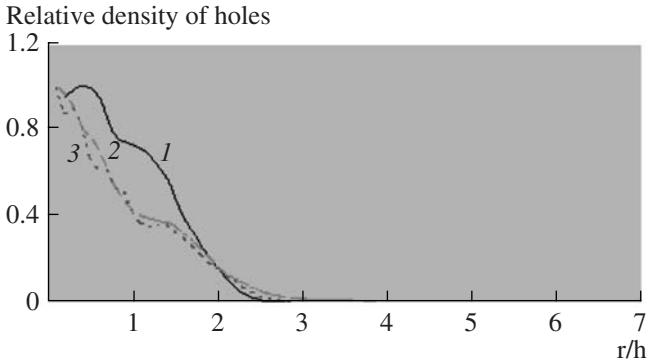

Fig. 9. The average distribution of the hole density at different gaps. Along the *X* axis, the ring radius is normalized in accordance with the interelectrode space value.

obtained for a new target with the electrode gap being the same.

DISCUSSION OF THE RESULTS

The obtained data show that the holes on the target are located irregularly, forming peaks in the curves. Owing to the algorithm used for determining the center of the distribution, there hits no spot onto the central ring whose diameter is small enough to explain the dip of the first point in some diagrams. The peaks in the curves don't disappear even after the great averaging shown in Fig. 8 (averaging for all the targets with the given gap). It is also seen that the distance between the electrodes increasing the curve slope diminishes turning from a bell-shaped one for small distances to a nearly straight one when the distance is large. After the averaged curves are rebuilt along the *X* axis and the radius is normalized for the interelectrode space value, it is seen that, at a gap of 5 mm, the curve trend differs from the behavior of the curves for other gaps. It is possible to explain this fact by the substantial change of the field distribution, in this case, as the scale of the plasma generation on the needle electrode becomes comparable with the gap size.

CONCLUSIONS

1. The electric discharge forms an individual matrix on the target permitting the creation of an irreproducible mark.

2. The simultaneous presence of the numeric code and the individual matrix in the identification mark allows one to quickly find the studied object in the database and to carry out its identification according to the coincidence (or noncoincidence) of the individual matrix (for instance, to recognize an illegal good).

3. Electrodischarge identification possessing all the features of quantum identification can not be tampered with and can be used as a protective technology in the process of creation of documents requiring strict control, even a national currency.

4. It is impossible in principle to produce two identical individual matrixes under a common code.

5. The presence of numeric and wave information in the identification mark allows one to build, in a new fashion, a multipurpose database of material resources (papers, metals, thin sheets of plastic, and so on).

6. The presence of the features of an interferential pattern in the target proves the streamer wave properties.

7. The presence of particular features in the form of an interferential matrix in the mark allows hoping that the numerical code (and the document as a whole) is fully protected.

REFERENCES

1. Shkilev, V.D., On Necessity of Forming the Unified Principles of Identification of the Accounted and Controlled Objects in the Framework of the National Information

System, *Proc. III Int. Conf. on Information Technologies*, 2003, pp. 56–60.

2. Shkilev, V.D., et al., Moldova Inventor's Certificate no. 3389, MD-BOPI, 2007, no. 8, p. 51.
3. Wang, L. and Wilson, R.G., Rotationally Invariant Statistics for Examining the Evidence from the Pores in Fingerprints, Coventry, 2007.
4. Raether, H., Electron Avalanches and Breakdown in Gases, London: Butterworths, 1964.
5. Hackermueller, L. et al., Wave Nature of Biomolecules and Fluorofullerenes, *Phys. Rev. Lett.*, 2003, vol. 91, pp. 23–35.
6. Basov, N.G., Molchanov, A.G., Nasibov, A.S., et al., Streamer Lasers on Solids, *Zh. Eksp. Teor. Fiz.*, 1976, vol. 70, no. 5, pp. 1751–1761.
7. Kuskova, N.I., Spark Discharges in Condensed Media, *Zh. Tech. Fiz.*, 2001, vol. 71, no. 2, pp. 51–54.

ISSN 1068-3755, Surface Engineering and Applied Electrochemistry, 2008, Vol. 44, No. 2, pp. 87–91. © Allerton Press, Inc., 2008.
Original Russian Text © A.M. Paramonov, A.V. Koval', 2008, published in Elektronnaya Obrabotka Materialov, 2008, No. 2, pp. 11–16.

ELECTRICAL SURFACE TREATMENT METHODS

New Potentials of the Electrospark Alloying Method for Prolonging the Service Life of Cutting Tools

A. M. Paramonov and A. V. Koval'

Institute of Applied Physics, Academy of Sciences of Moldova,
ul. Academiei 5, Kishinev, MD-2028 Republic of Moldova

Received January 18, 2007

Abstract—The analysis of basic defects of sewing cutters is carried out, and the technology of their elimination is designed. Results of a new method of hardening and increasing the service life of cutting blades are presented.

DOI: 10.3103/S1068375508020026

A wide variety of different steel tools are used industrially (in the woodworking industry, printing industry, tailoring industry, and so on). Their service life is considerably limited due to the occurrence of various defects during production or operation. The idleness of facilities caused by the replacement of tools and high cost of the equipment lead to significant production and material losses. Because of this, the search for solutions allowing increasing the service life of tools and thus diminishing these losses is rather urgent.

The process of developing measures preventing and eliminating the most commonly encountered cutting tool defects might be considered using the example of blades for fabric packet cutting out in the tailoring industry. They are used in vertical machines for cutting out cloth packets 60–250 mm in thickness (Fig. 1). The machines comprise a tabletop item with a built-in motor having a rotational speed of 3000–4000 revolutions per minute. The motor sets the cutting blade into vertical reciprocating motion with a controlled amplitude. Some machine models are provided with an adamantine disc to resharpen the blade and, after 30–40 grindings, it is replaced by a new one. The high demands on the blade quality (absence of warpage, high hardness, and surface fineness) and the machine-loaded mechanisms are the main factors defining its cost. With the machine cost of 400–700 dollars [1, 2], the assembly includes 1–2 blades. Any additional blade costs 20–30 dollars. Besides the original blades, one can purchase blades manufactured by other producers. They are cheaper (10–15 dollars), but their working life is shorter and they have various defects as they are made using a simplified technology. Thus, there arises the necessity of searching for methods permitting one to restore the working sizes of the blades, to increase the interval between the grindings, to reduce the material removed during sharpening through hardening of the cutting edge, and to optimize the blade wear in the course of the cutting. These methods shouldn't make the cost of the reworked blades higher than that of the original ones.

We chose the processing methods after a thorough analysis of the defects of blades 300 mm long (the cutting edge is 150 mm in length) used for cutting out fabric packets up to 100 mm thick. It is established that there exist industrial and working defects of the blades. The industrial defects are the result of breaking the blade production technology. They manifest themselves in the form of warpage and disruption of the guide profile quality (Fig. 2a). Working defects may include irregular wear of the cutting edge and the blade warpage because of the violation of the operation and grinding conditions (Fig. 2b), as well as "indents" on

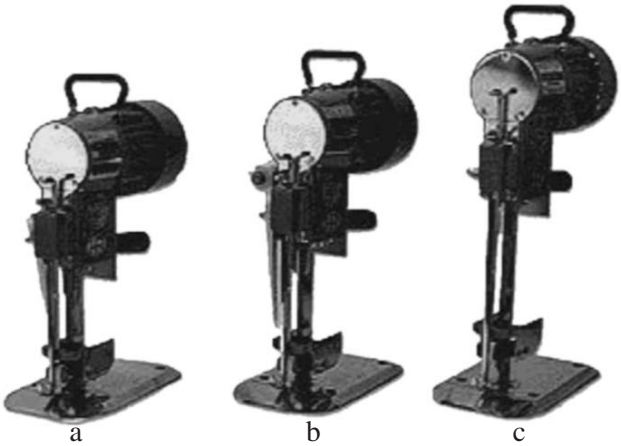

Fig. 1. Vertical cutting machines using blades with the following cutting edge lengths: a – 150 mm, b – 200 mm, and c – 250 mm.

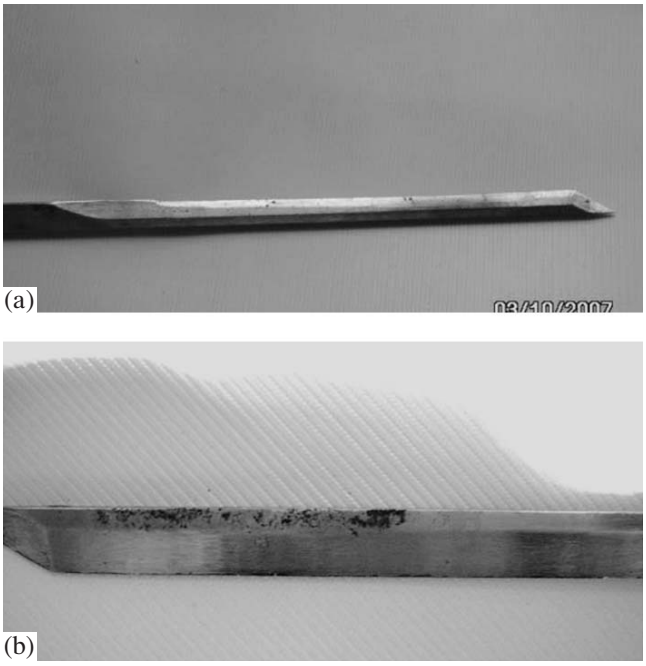

Fig. 2. The blades before processing.

the cutting edge occurring through the improper sharpening or occasional penetration of solid occlusions into the cutting area.[1]

The presence of the mentioned defects causes the following consequences. In the case when the blades are small in section (2 × 9 mm), their length is up to 400 mm for a fabric packet 200–250 thick being cut out. The big outreach of the cutting part results in the blade warpage even at minor overheats causing a sharp growth of the load on the blade back plane bearing on the machine supporting roller leading to the wear and breakage of the pilot and guides as well as to the blade rib chipping off. The same outcome is observed when there are indentations in the supporting section. As some of them are rather large, it results in cloth hooks, sharp reduction of the cutting quality, and the machine breakdown owing to the blade jamming in the guide.

The blade service life sharply diminishes as it is necessary to flatten the cutting edge on grinding. This is due to the irregular wear along the cutting edges and emerges when thin fabric packets are being cut out and only a part of the cutting edge works. The same result is observed when unequally worn adamantine discs are used to sharpen the blades causing nonsymmetrical shaping of the cutting edge. Consequently, in order to flatten it, it is necessary to remove much metal along its full length.

Thus, the analysis shows there is a need to solve two main problems. First, it is necessary to apply metal on the blades to revive the profile and harden the cutting edges. Second, it is required to repair blades having warpage.

By now, various electrophysical and electrochemical methods have been elaborated and are used to restore and harden the component parts.

The surface layer properties may be substantially improved through chemical-thermal processing because it increases the hardness, the heat stability, and the resistance to corrosion and, in some cases, reduces the friction coefficient. However, this kind of treatment isn't suitable for hardening existing blades as the thickness of the changed layer is very small and it is removed nearly completely from the working margins during sharpening.

Such surface modification methods as chemical deposition from the gaseous phase, thermal vacuum spraying, and vacuum ion-plasma coatings (nitration, alloying, and so on) have drawbacks: the high temperature of the part processing (350–2000ºC), the complexity, and the difficulty associated with the equipment. In addition, they are employed only for nonresharpened tools. Plasma and detonation application of powder material coatings is also limited because of the complicatedness of the process, the facility location, and the rather high temperature of the part heating (up to 200–2500°C). Moreover, often, the deposited layer is breakable and has a stratum structure; therefore, annealing is necessary [3].

It has become possible to considerably improve the surface wearing qualities thanks to the working out of industrial lasers. Due to the high density of the energy in the beam, there occurs quick heating of a thin surface layer of metal up to its melting. The following quick heat abstraction into the metal bulk results in the hardening of the surface layer and it becomes highly solid and wear resistant. Alloying through introduction of the substance powder into the beam is possible as well. The equipment complexity, inconvenience, large power consumption are the main drawbacks of this method [3, 4].

The electrospark alloying method (ESA) is one of the most innovative procedures. It is widely used to restore and change the physical and chemical properties of machine parts and tools. The low cost of the equipment, the low power expenditures, and small consumption of hard-alloyed tools are its principal advantages. Such ESA merits as the processing locality, the comparatively low roughness of the obtained layer, and the small heating of the operation zone are very important when working with a blade [5–8]. The modernized installation "Elitron-21M" was used for the alloying [9, 10]. Thanks to the presence of the step-by-step control of the power consumption and the good regulation of the spark pulses, the installation permitted producing separate formation of the coating thickness and quality. The deposited layer had a thickness up to 0.35–0.4 mm under energy-intensive conditions. The coatings were

[1] Paramonov, A.M., Koval', A.V. Elektronnaya obrabotka materialov, 2008, no. 2, pp. 11–16.

applied from the alloys T15K6, BK8, and nichrome. The coating smoothing (if necessary) was carried out with graphite plate electrodes. To remove the processed blade warpage, there was elaborated a special procedure: some conductors (a specific copper vise that allowed providing quick heat removal from the processing zone) were manufactured, and the required discreteness of the working was found ensuring the wanted time interval of the working zone cooling. This procedure allows removing the warpage of new blades as well.

The processing of 25 blades was conducted with 7 being new ones and 18 being used. For the new blades, there was removed warpage and closed "indents" on the bearing part and the cutting edge was hardened. For the used blades, the spotty wear was repaired, the cutting edge was hardened, and warpage was removed (if it occurred).

1. Electrospark alloying of new blades. First, the metal was deposited into the region of "indentations" on the blade bearing part. The processing was carried out under energy-intensive conditions with the spark pulse frequency being low. Steel wire, nichrome, and T15K6 alloy served as the electrodes. To apply the metal uniformly, the deposited layer was smoothed at regular intervals with graphite electrodes under low-energy high-frequency conditions. After the layer with the wanted thickness is applied, finish alloying and grinding was conducted. The cutting edge hardening is the next stage. The work consisted of alloying the margins forming the cutting edge. In this work, the alloying was conducted along one of the margins (Fig. 3a) under low-energy conditions with the frequency up to 1500 Hz. Such a method of the coating application permits one to reduce the processing time and to greatly increase the blade service life not only because of the diminution of the metal removal during sharpening but also due to the self-sharpening effect. Because, under these conditions, the electropulses possess little energy and special auxiliaries are used, it is possible to carry out alloying close to the cutting edge.

After processing, there was conducted grinding with adamantine discs to obtain the wanted sharpness of the cutting edge and restoration of its center.

As was mentioned above, considerable growth of the lifetime is reached with the aid of the self-sharpening effect. It manifests itself in the following way. After working of one margin as the blade wears during cutting, there is some shift of the cutting edge relative to the blade symmetry center sideways of the processed margin (Fig. 3b). After the cutting edge becomes blunt, the unprocessed margin is alloyed and the blade grinding is carried out. It should be emphasized that both margins are sharpened even though only one was worked before. Now, during cutting, the operating edge begins to shift sideways of the just processed margin. Consequently, by conducting alternate alloying of the margins, we can considerably lengthen the blade service life. This cutting edge shift doesn't influence the accuracy as it isn't more than 1–1.5 mm.

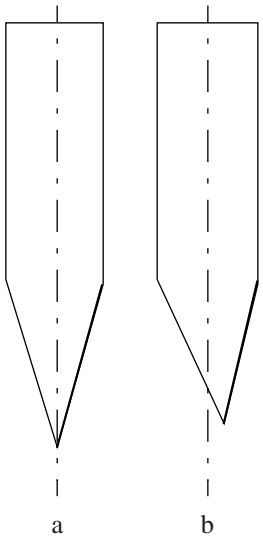

Fig. 3. View of the cutting edge: a – after hardening, b – during operation.

The self-sharpening effect also allows increasing the longevity of the adamantine discs used to sharpen the blades as the discs operate in turns (not simultaneously), and the removal of metal during the grinding is greatly lowered because it is only necessary to perform a small correction of the cutting edge.

2. Electrospark alloying of blades with spotty wear along their length. Restoration of the cutting edge was carried out in the regime of little energy consumption with the frequency of the spark pulses being up to 1000 Hz. The alloying was conducted by the step-by-step application of the covering on the worn part of the blade using electrodes made from steel and nichrome. The cover thickness was in the range of 0.10–0.15 mm. The applied layer was flattened at regular intervals by graphite electrodes under high-frequency conditions. After the restoration, the whole blade was ground to flatten both the processed and unprocessed parts over the height of the cutting edge profile. The hardening of one of the working margins along the whole length (as is described in part 1) by electrodes made from the alloys T15K6 and BK8 under high-frequency conditions with the frequency of the spark pulses being up to 1500 Hz appeared to be the last stage.

3. Improvement of warpage. As described above, the blade restoration and hardening was carried out in special jigs permitting one to avoid warpage during the treatment. They were used to improve the warpage of new blades. With this purpose in mind, graphite electrodes were employed under the high-frequency conditions with smooth control of the spark pulse frequency (up to 2000 Hz). The treatment was conducted in the following way. The blade was fixed in the jig in such a

Fig. 4. Blades after the bearing part surface has been restored.

way that it was placed with maximum tightness to its surface, and the length of the zone where the treatment occurred didn't exceed 2–3 cm. In order to obtain letting down, the processing was conducted on the concave side of the blade with carrying out repeating point treatment of its guide ribs. After the electrode touched the surface, the spark pulse frequency was smoothly increased until the electrode grew warm. The treatment lasted for 4–7 seconds, and then the electrode was taken away, the blade was cooled, and the alloying was conducted at another point. The treatment time periodicity was determined experimentally according to the blade heating degree and the time of its complete cooling. The processed parts of the blade ribs were ground with the aid of an adamantine tool to obtain the wanted quality of the surface.

The results concerning work on the restoration of the blade bearing part are shown in Fig. 4. The blades with a hardened cutting edge are presented in Fig. 5. It is seen that the quality of the processed surfaces is high enough.

After the restoration and hardening, there were carried out tests of the blades in a garment factory, and the following results were obtained:

1) The restored guide doesn't effect the machine operation.

2) The cutting edge hardening allows increasing the number of grindings.

3) The hardening and self-sharpening effect of the cutting edge extend the blade service life by 7–10 times.

4) The use of the self-sharpening effect raises the adamantine disc service life by 5–6 times.

Virtually one processed blade of an after-market fabricator can substitute for not less than 5–7 original blades.

Consequently, there has been elaborated a number of new technologies permitting one to carry out restoration and hardening of cutting tools using the method of electrospark alloying. The application of these methods for blades used to cut cloth packets made the following possible:

1. removing their warpage,

2. restoring the blade bearing part, and

3. raising the blade cutting edge durability by 6–8 times.

Taking into consideration the small cost of the equipment for ESA, the low power expenditures, and the small requirement for hard-alloyed electrodes, the use of the processed blades manufactured by after-market fabricators becomes economically efficient. The results of the investigations and their practical applica-

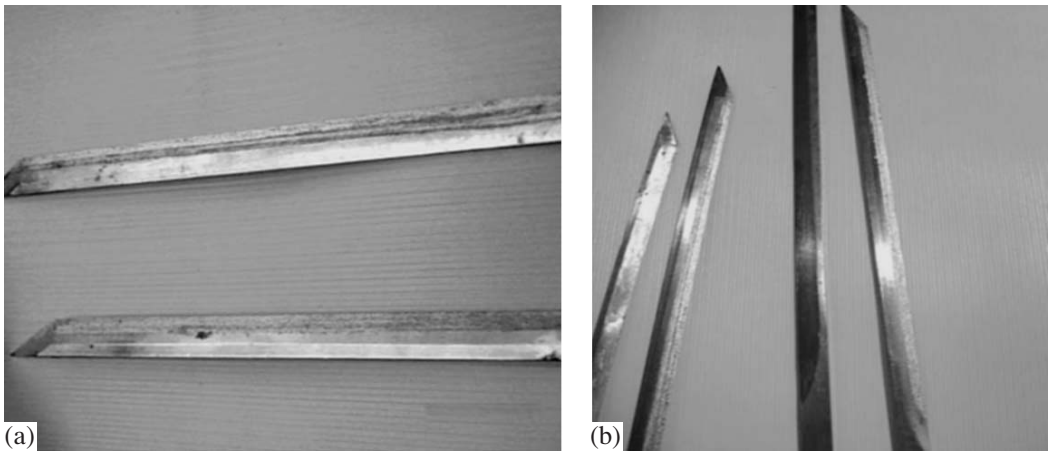

Fig. 5. Blades after the cutting edge has been hardened.

tions can be successfully employed to extend the service life of other cutting instruments as well.

REFERENCES

1. www.shanggong.ru
2. www.baroha.ru
3. Popilov, A.Ya., *Spravochnik po elektricheskim i ul'trazvukovym metodam obrabotki materialov* (Handbook on Electric and Ultrasonic Methods of Material Processing), Moscow: Mashinostroenie, 1983.
4. Arazamasov, B.N. et al., *Konstruktsionnye materially* (Construction Materials), (Reference-book), Moscow: Mashinostroenie, 1990.
5. Lazarenko, B.R. and Krasyuk, B.A., USSR Inventor's Certificate no. 68283, *Byull. Izobret*., 1947, no. 4, pp. 379–380.
6. Paramonov, A.M., Safronov, I.I., and Semenchuk, A.V., Study of Usage Prospects for Antivibration Electrospark Alloying, *Electron. Obrab. Mater.*, 1997, no. 5-6, pp. 28–32.
7. Paramonov, A.M., Regularities of Coating Formation at Electrospark Alloying at High Frequencies. Antivibration Electrospark Alloying, Report on SRW Inst. Applied Physics, Mold. Acad. Sci., no. 81019453, Kishinev, 1985.
8. Fursov, S.P., Paramonov, A.M., Dobynda, I.V., and Semenchuk, A.V., *Istochniki pitaniya dlya elektroiskrovogo legirovaniya* (Power Sources for Electrospark Alloying), Kishinev: Shtiintsa, 1983.
9. Glybach, K.V., Lyubchik, M.Ya., Paramonov, A.M., and Fursov, S.P., USSR Inventor's Certificate no. 318453, *Byull. Izobret*., 1971, no. 32, p. 47.
10. Paramonov, A.M., Fursov, S.P., Lyubchik, M.Ya., and Glybach, K.V., USSR Inventor's Certificate no. 390900, *Byull. Izobret*., 1973, no. 31, p. 94.

ISSN 1068-3755, Surface Engineering and Applied Electrochemistry, 2008, Vol. 44, No. 2, pp. 92–97. © Allerton Press, Inc., 2008.
Original Russian Text ©E.D. Pleshka, 2008, published in Elektronnaya Obrabotka Materialov, 2008, No. 2, pp. 17–24.

Adhesion of Iron Coatings with Steel and Cast Iron

E. D. Pleshka

Institute of Applied Physics, Academy of Sciences of Moldova,
ul. Academiei 5, Chisinau, MD-2028 Republic of Moldova
E-mail: bortzoi_tudor@yahoo.com

Received October 15, 2007

Abstract—The iron-plating process in methyl sulfate chloride electrolytes was investigated. The conditions of iron plating ensuring the coating adherence with steel and pig iron required in the technological processes of reconditioning and strengthening of machine pieces are determined. Process conditions ensuring the high coating adherence with steels 45, 15HGT, 40H, and grey and high-strength pig iron are found; they include steps: powering on of the polarizing current with the initial density of 0.15–0.5 kA/m^2 immediately after insertion of pieces in the electrolyte and raising of the current density up to the working level with a rate of 4–5 A/m^2 s. Metallographic, polarizing, and other research show the influence of the initial electrolysis conditions on the formation of the first layers of coverings and the process of iron electrocrystallization on structural phases of tempered steel and grey and high-strength pig iron.

DOI: 10.3103/S1068375508020038

INTRODUCTION

The strength of the iron coating adhesion to pieces of material depends on many factors and conditions of the technological processes. The determining influence on the adhesion is exerted by the chemical composition of the piece of material, its thermal treatment, the mechanical conditions of the electrochemical operations, and the initial and subsequent modes of electrodeposition [1–6].

The analysis of the methods of mechanical treatment of steel and cast iron pieces has shown that polishing, turning, and honing carried out for putting them into the relevant geometrical shape provide satisfactory adhesion [5, 7]. The modes of preliminary mechanical treatment must form the required degree of roughness and uniformity of the properties of the surface layer subject to electrochemical treatment at operations of iron electrodeposition.

Realization of the process of piece iron plating according to the conventional recommendations for chloride, sulfate, and other electrolytes provides satisfactory adhesion mainly in conditions of high electrolyte temperatures for green steel and cast iron. However, due to the variety of applied materials and the design features of pieces, the required adhesion and quality of their recovery or hardening are not obtained in industry in many cases. This is attributed to the instability of the process and the low reproducibility of the physicomechanical properties of iron coatings. The mentioned characteristics are determined in many instances by the composition and stability of the electrolyte properties as well as by the reasonable selection of the electrolysis conditions [5].

The aim of the present paper is to determine the electrolysis modes that provide high coating adhesion to various metallic materials and to study the process of formation of iron electrodeposits on phases of steel and cast iron structures in the initial and subsequent periods of electrolysis.

EXPERIMENTAL

It is of interest to study the strength of adhesion of iron deposits obtained in methyl sulfate chloride (MSC) and multicomponent methyl sulfate chloride (MSC3) electrolytes to materials made of steel 45, 40X, and 15XGN2T; gray cast iron; and high-grade cast iron VCh-50, which are most widely used in agricultural engineering (see Table 1). It was efficient to study the theoretical justification of the conditions for iron electrocrystallization and the formation of a transition layer and structures of various types as applied to the process of electrolysis in a methyl sulfate chloride electrolyte containing iron ions only. It allowed considering the physical and electrochemical phenomena with a lower quantity of influencing factors and studying the possibility to apply the found principles to the process of obtaining strongly adherent doped iron coatings in a multicomponent methyl sulfate chloride electrolyte containing nickel, manganese, and other elements.

The electrolysis conditions were selected within the range of pH = 0.8–1.8, of temperature 298–333 K, and

Strength of adhesion of the coatings obtained in multicomponent methyl sulfate chloride electrolyte to steel 45 (HRC 54-56): $D_{k.init.}$ = 0.25 kA/m^2; the rate of the current change at the starting operation is 5 A/(m^2 s); weighing at the connected voltage on the electrolyzer

Series no	Electrodeposition conditions			Adhesion strength	Character of the pin separation from the coating
	pH	T, K	D_k, kA/m^2	MN/m^2	
1	0.9	298	3.0	350	Break along the coating
2	0.9	333	6.0	423	There are coating particles on the pin; metal particle separation from the pin
3	1.3	298	3.0	360	Break along the coating
4	1.3	313	6.0	382	There are great coating particles on the pin
5	1.3	333	6.0	371	Breaking of metal particles from the pin
6	1.6	313	6.0	323	Breaking of great particles from the coating
7	1.6	333	6.0	362	There are coating particles on the pin

of current density 2–8 kA/m^2. The sample preparation and preliminary operations (fat removal, anode treatment, and initial conditions of electrolysis) were selected by the method presented in work [5]. The cycle of iron plating with a current density of 0.1–0.7 kA/m^2 in the initial electrolysis period was realized according to the diagram (Fig. 1). The time of the initial electrolysis period was 5 min with the subsequent starting

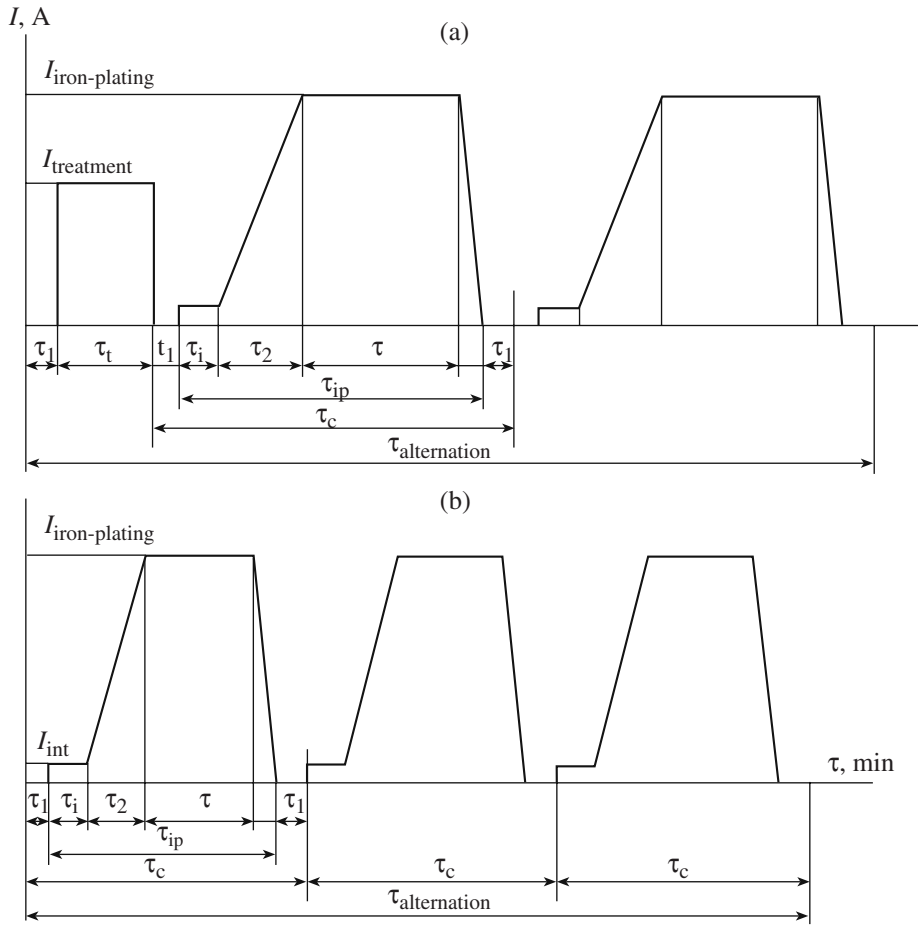

Fig. 1. Alternation cycles of iron plating of pieces: (a) in the electrolyte requiring current treatment; (b) in the MSC-3 electrolyte requiring no current treatment.

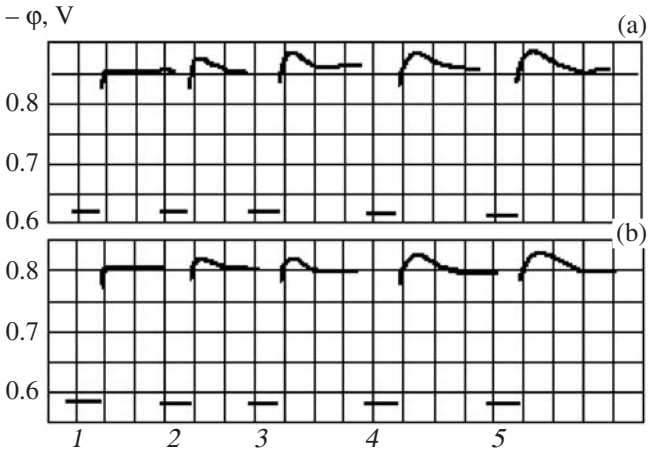

Fig. 2. Oscillograms of the cathode potential (steel 45) in MSC electrolyte: D_k = 2 kA/m^2; T = 313 K; pH = 1.3 (a), 0.9 (b). Currentless storage, s: 5 (*1*); 30 (*2*); 60 (*3*); 120 (*4*); 180 (*5*).

operation of the iron plating with a current change rate of 0.5–0.7 kA/(m^2 s). The sample iron plating for determination of the strength of the adhesion of the coatings obtained in the multicomponent MSC3 electrolyte was realized in a range of modes satisfactory in their reproducibility, quality, and the conditions of their possible practical application.

Metallographical tests were carried out using MBI-6, MIM-8, and PMT-3M microscopes. The structure of the materials and coatings was determined using conventional techniques with recommended and special etching solutions. The influence of the initial conditions on the adhesion was studied at the sample storage in the electrolyte after immersion for 0–180 s up to the electrolysis current connection. For the quantitative estimation of the adhesion strength, a coating with a thickness of 2–2.6 mm was deposited on the samples with pins 3 mm in diameter. The required coating thickness was determined on the basis of the condition of the correlation of the forces necessary for the pin separation and the coating layer shifting in the separation zone [5]. In realization of the experiments, for the qualitative estimation of the adhesion of the thickness of the coating on the steel and cast iron samples, the cylindrical form was 1 mm.

RESULTS AND DISCUSSION

In order to select reasonable modes, the influence of the currentless sample storage in the multicomponent MSC3 electrolyte and of the initial electrolysis conditions on the strength of the adhesion of the coatings deposited, steel 45 was studied first.

At the initial current density of 0.25 kA/m^2 with the operation of the currentless storage in the electrolyte being omitted (the initial current was connected immediately after the sample immersion into the electrolyte), the adhesion strength was 390 MPa. The currentless storage up to 30 s contributed to a decrease of the adhesion strength to 382 MPa. The increase of the duration of the currentless sample storage in the electrolyte for up to 120 s decreased the strength of the coating adhesion to the steel more significantly (down to 314 MPa). At the electrolyte acidity (pH = 1.6) the long-duration currentless sample storage (120 s) also decreases the adhesion strength. The coatings obtained at the same acidity and at the initial electrolysis current connection immediately after the sample immersion into the electrolyte had an adhesion strength of 323–362 MPa.

The worsening of the adhesion with increasing the currentless sample storage in the electrolyte is due to certain causes; according to the research data and suppositions of [1–5], the principal causes are the chemical dissolution of oxide compounds of iron, the formation of an incoherent layer of products of chemical reactions, and the increase of the thickness of the layer of adsorbed organic substances on the material surface. This is confirmed by the increase of the cathode potential pulse after connection of the polarizing current on the oscillograms "potential–time" measured at the currentless storage for 5–180 s (see Fig. 2).

The Negative influence of the long-duration currentless storage is also confirmed by the metallographic examinations of transverse microsections of the samples (see Fig. 3). After the chemical treatment of the microsections, the interface "coating–metal substrate" (1) is shown in the form of a continuous dark intercalation corresponding to the currentless storage time. Its thickness grows as the currentless storage duration increases; this was also observed at other electrolysis modes. A dark intercalation characterizing the layer of more imperfect metal structure saturated with impurities is also observed at various durations of the current disconnection in the process of the electrolysis (Fig. 2, pos. *2*).

According to the experiment results and proceeding from the previously stated suppositions and principles of the process realization, in order to obtain high adhesion strength, the currentless piece storage in the methyl sulfate chloride electrolyte before electrolysis starting is inefficient. Similar results were obtained at iron plating of steel and cast iron in chloride, sulfuric acid, and mixed electrolytes in laboratory conditions and at recovery of pieces in conditions of production.

At the initial density of the current of iron plating D_k = 0.2–0.5 kA/m^2, the adhesion strength was 387–392 MPa; at D_k = 0.7 kA/m^2, it decreases to 350 MPa. According to the results of the cathode polarization studies, at these current densities, the potential value is obtained at which, simultaneously with hydrogen evolution and organic component decomposition, there takes place sufficiently intense deposition of iron. In these conditions, the deposited crystals may be also

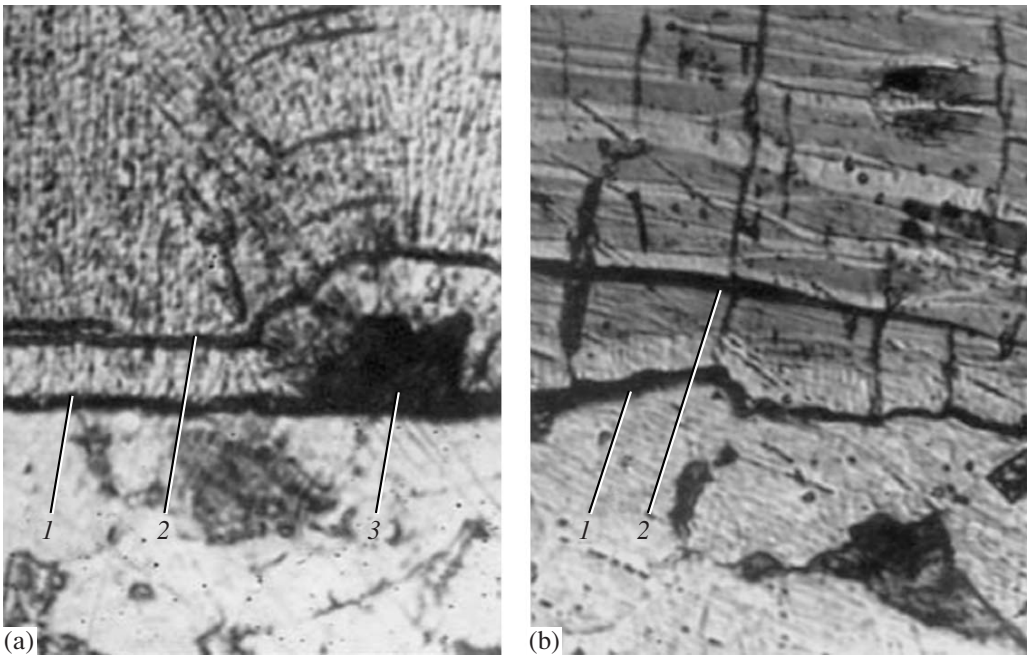

Fig. 3. Structure of the boundary layer of the coatings (1000 × 2) obtained in MSC electrolyte with currentless storage for 120 s at the following electrolysis modes: D_k = 2 kA/m^2; T = 313 K; pH = 0.9 (a), 1.6 (b).

formed on the passive cathode surface (see Fig. 3, poss. *1–3*); this causes formation of an imperfect metal structure. This is shown in the form of dark layers at chemical etching of microsections.

The metallographic examinations allowed finding that, at D_k = 0.2–0.5 kA/m^2, there occurs coalescence of the coating and the piece material (see Fig. 4). Crystals of the iron coating (pos. *1*) are a continuation of the cementite phase (pos. *2*), and, on the ferrite grains, steels exhibit more pronounced growth characterized by a fibrous or granular structure (pos. *3*). On the samples iron plated at a high initial current density of 0.7 kA/m^2, after chemical etching of microsections, the interface "coating–base" (see Fig. 5) is shown in the form of a thin dark transition layer. The subsequent boundary layer of the coating is characterized by a sufficiently perfect structure (see Fig. 4).

It was also found during the examination that the deposit layer formed in the initial electrolysis period at the current connection immediately after the sample immersion into the electrolyte has a strong adhesion to the base irrespective of the acidity in the range pH = 0.8–1.6.

On the basis of the obtained results of the deposit formation study, the peculiarities of the process of iron

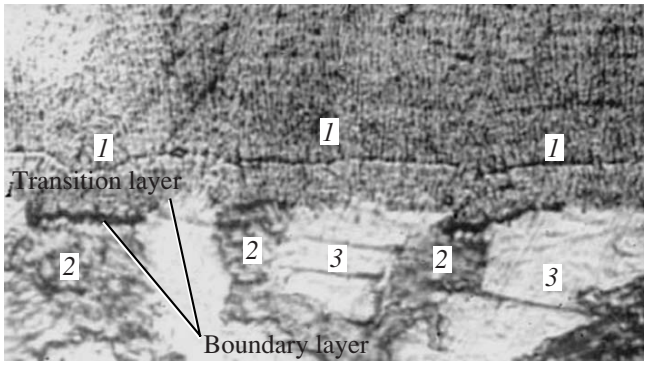

Fig. 4. Structure of the boundary layer of the coatings (1000 × 2) obtained in MSC electrolyte on hardened steel 45 at the following modes: D_k = 4 kA/m^2, T = 313 K, pH = 0.9.

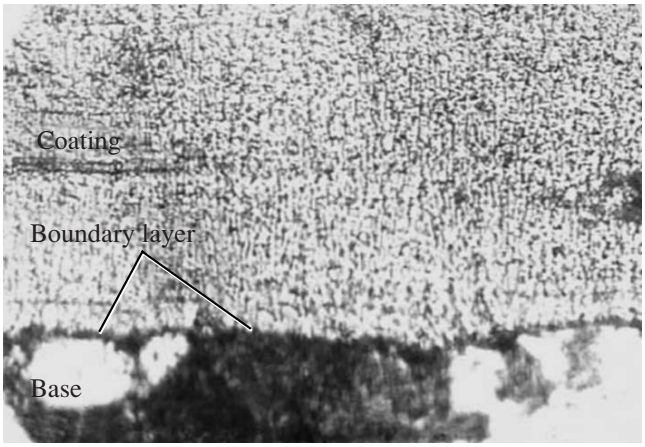

Fig. 5. Structure of the boundary layer of the coatings (1000 × 2) obtained in MSC electrolyte on hardened steel 45 at the following modes: D_k = 6 kA/m^2, T = 313 K, pH = 0.9.

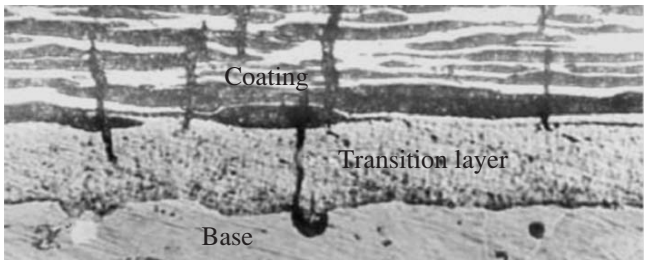

Fig. 6. Structure of the boundary layer of the coatings (1000 × 2) obtained in MSC electrolyte on hardened steel 45 at the following modes: D_k = 6 kA/m^2, T = 313 K, pH = 1.5.

electrodeposition in methyl sulfate chloride electrolytes may be presented as follows.

In the initial period at the polarizing current connection immediately after the sample immersion into the electrolyte, the chemical and electrochemical reactions contribute to intense hydrogen evolution on the cathode. Simultaneously, there take place destruction (decomposition) of the layer of oxides and denudation of the surface of the material structure phases, and, on their active places, crystallization centers nucleate.

At low overpotentials on the cathode (at a polarizing current of 0.1–0.5 kA/m^2), the rate of the iron electrocrystallization is apparently low. The concentration of the iron ions capable of discharging is sufficient for the growth of the first crystals and the subsequent growth of a polycrystalline deposit. Judging by the absence of cracks, the coatings are understressed and form a sticky transition layer, which is well adherent to the base material and characterized by small number of defects and impurities. This determines the high strength of the deposit adhesion to the base (see Figs. 4 and 5).

The cathode polarization increase up to the values of the current density corresponding to the operation mode is accompanied by a change of the ratio of the electrode reaction rates, an increase of the iron power yield, and a change of the crystallization conditions. The structure obtains a structure, growth habit, dispersion, and hardness characteristic of the given mode of electrolysis. A positive influence on the process of formation of electrolytic deposits of metals is apparently rendered by joint participation of ions of methyl sulfate and chlorine in cathode electrochemical reactions [5]. At pH = 0.9–1.3, deposits with a fewer number of defects are formed (see Figs. 4 and 5). They contain a small amount of hydrogen; they are less stressed; and, being characterized by high viscosity and strength, they resist destruction better [5]. At the sample deformation (by the compression method) by 25% length, they do not flake.

At pH = 0.9, the electrolyte temperature increase to 333 K contributes to the increase of the strength of the electrolytic iron adhesion to hardened steel St.45 from 350 MPa to 423 MPa. The same results were obtained at the electrolyte acidity pH = 1.3. The highest strength of the coating adhesion (348–423 MPa) was found in the multicomponent methyl sulfate chloride electrolyte with St.45 at pH = 0.9–1.3 and T = 313–333 K (see Table 1).

It should be noted that, in the studied multicomponent electrolyte, the strength of the doped iron coating adhesion to steel obtained by virtue of the selected initial conditions of the electrolysis and operation modes is not less than in the methyl sulfate chloride electrolyte [5].

The electrolyte acidity decrease to pH = 1.6 leads to the adhesion strength decrease to 323–382 MPa (see Table). At low electrolyte acidity (pH = 1.6 and more), due to the intensification of the process of penetration into the deposit of foreign particles, organic substances, and periodically deposited hydroxides, the deposit structure becomes layered and is characterized by specific cracking (see Fig. 6). At deformation by the compression method, the loss in weight of the deposits obtained at pH = 1.6, D_k = 4 kA/m^2, and T = 313 K due to brittle failure was 6.4–8.6%.

Analysis of the investigation results shows that the doped iron coatings characterized by a fibrous, granular, or layered structure and by adhesion strength equal or close to the strength characteristics of the materials selected for the test may be applied for recovery of pieces operating in various load conditions.

Thus, in order to obtain high strength of the coating adhesion to steel in the multicomponent MSC electrolyte, it is necessary to realize the following conditions:

1) The initial polarizing voltage (current) must be connected immediately after the piece immersion into the electrolyte.

2) An initial current density of 0.15–0.5 kA/m^2 must be maintained for 150–220 s.

3) The current increase at starting the operation must be realized with a rate of 4–12 kA/m^2 s.

The initial conditions found were adopted by us for investigation of the electrolysis mode influence on the strength of the coating adhesion to the steels 15XGN2T and 40X and grey and high-grade cast iron (see Figs. 7 and 8). The strength of the coating adhesion to the steel 15XGN2T at pH = 0.9–1.6 and T = 313–333 K was 272–377 MPa and that for the steel 40X with the BH of 230–270 was 348–376 MPa.

The data on the adhesion strength of the doped iron coatings containing carbon and other elements, as well as the modes of their obtaining in methyl sulfate chloride and multicomponent methyl sulfate chloride electrolytes, were applied for hardening and recovery of a wide nomenclature of pieces.

The development of the technology for recovery of pieces made of steel and cast iron was based on the

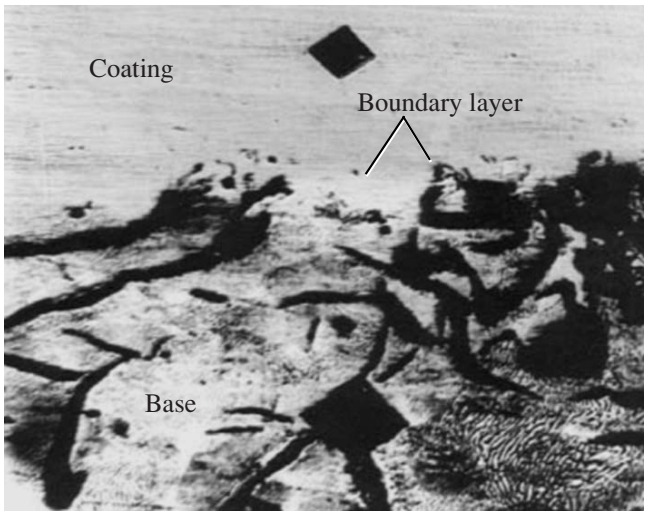

Fig. 7. Structure of the boundary layer of the coatings (500 × 2) obtained in MSC electrolyte on cast iron SCh 24–44 at the following modes: D_k = 6 kA/m^2, T = 313 K, pH = 1.3.

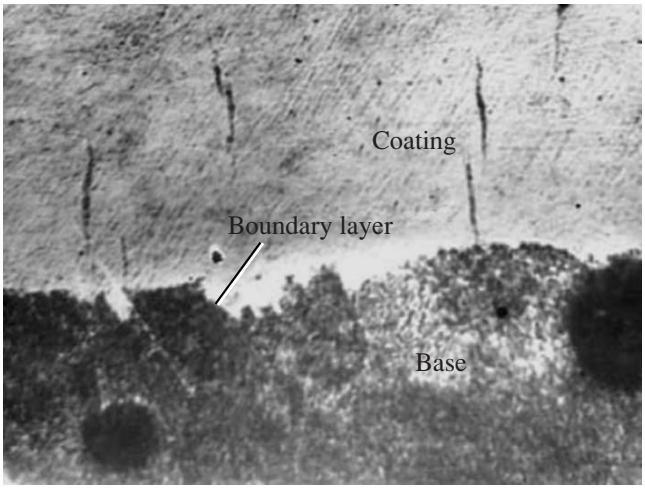

Fig. 8. Structure of the boundary layer of the coatings (500 × 2) obtained in MSC electrolyte on cast iron VCh 50 at the following modes: D_k = 4 kA/m^2, T = 313 K, pH = 1.3.

described principles of the process realization and on the experimentally confirmed initial and subsequent conditions in the studied range of electrolysis modes: pH = 0.8–1.6; T = 293–333 K; D_k = 2–8 kA/dm^2. The technology for recovery and hardening of pieces made of steel and cast iron was introduced in factories repairing agrimotors, automobiles, and other engines.

CONCLUSIONS

1. The process of electrolysis in methyl sulfate chloride electrolytes was studied and the ranges of modes providing strength of iron coating adhesion to steel and cast iron adoptable for technological processes of recovery and hardening of machine pieces were found.

2. Modes of iron plating in multicomponent methyl sulfate chloride electrolyte providing high strength of adhesion to steel St.45, 15XGN2T, and 40X and gray and high-grade cast iron were determined: connection of the polarizing current immediately after the immersion of the piece in the electrolyte, electrolysis at an initial current density of 0.15–0.5 kA/m^2 for 3–15 min, and the current density increase at starting of the operation at a rate of 4–5 A/m^2 s.

3. By virtue of metallographic and other methods, there was found the influence of the electrolysis initial conditions on the iron electrodeposition process on the phases of structure components of hardened steel and gray and high-grade cast iron, as well as on the formation and growth of strongly adherent coatings with fibrous, granular, and layered structures.

REFERENCES

1. Alekseev, V.P. and Petrov, Yu.N., Selection of Modes of Surface Preparation in Iron Sulfuric Acid Electrolyte, in *Trudy Kishinevskogo SKhI im. M.V.Frunze* (Writings of Frunze ACI, Chisinau), Chisinau, 1970, vol. 59, pp. 101–105.
2. Pankratov, M.P. *Issledovanie vliyaniya tekhnologicheskikh faktorov protsessa elektroosazhdeniya zheleza na stseplyaemost' pokrytii pri vosstanovlenii stal'nykh detalei mashin (*Study of Influence of Technological Factors of Iron Electrodeposition Process on Adhesive Capacity of Coatings at Recovery of Steel Machine Pieces), Kharkov: KhADI, 1964.
3. Andreeva, L.N. and Kalmutskii, V.S., Comparative Studies of Electrolytic Iron Adhesion Strength, *Trudy Kishinevskogo SKhI im. M.V.Frunze* (Transactions of Frunze ACI, Chisinau), Chisinau, 1970, vol. 59, pp. 45–55.
4. Melkov, M.P., *Tverdoe ostalivanie avtotraktornykh detalei* (Hard Steel–Plating of Motor–And–Tractor Pieces), Moscow: Transport, 1971.
5. Pleshka, E.D., Study and Development of Technology of Recovery of Motor–And–Tractor Pieces by Iron–Plating in Methyl Sulfate Chloride Electrolyte, *Cand. Sci. Dissertation*, Chisinau, 1979.
6. Mitryakov, A.V., Obtaining of Strongly Adherent Electrolytic Iron Coatings, in *Voprosy teorii i praktiki* (Problems of Theory and Practice), Saratov, 1985.
7. Advancement of Technology for Recovery of Worn–Out Motor–And–Tractor Pieces by Wear Resistant Electrolytic Coatings, in Otchet po NIR 09/11–20 (Report on Research Engineering 09/11–20), Chisinau, 1984, state registration no. 77024435 SRC of Chisinau AGI, Moscow, VNITI no. 02840018082.

ISSN 1068-3755, Surface Engineering and Applied Electrochemistry, 2008, Vol. 44, No. 2, pp. 98–105. © Allerton Press, Inc., 2008.
Original Russian Text ©S.A. Baranov, A.I. Dikusar, Yu.D. Gamburg, 2008, published in Elektronnaya Obrabotka Materialov, 2008, No. 2, pp. 25–34.

ELECTRICAL PROCESSES IN ENGINEERING AND CHEMISTRY

Microkinetic Model of Nucleation and Its Application in Electrochemistry

S. A. Baranov[a, b], A. I. Dikusar[a, b], and Yu. D. Gamburg[c]

[a]*Institute of Applied Physics, Academy of Sciences of Moldova, ul. Akademiei 5, Chisinau, MD-2028 Republic of Moldova*
E-mail: dikusar@phys.asm.md
[b]*Shevchenko Pridnestrovskii State University, ul. 25 Oktyabrya 128, Tiraspol', Republic of Moldova*
[c]*Frumkin Institute of Physical Chemistry and Electrochemistry, Russian Academy of Sciences, Leninskii pr. 31, Moscow, 117071 Russia*

Received November 5, 2007

Abstract—The phenomenon of electrochemical nucleation in micro- and nanoparticles was investigated. The theory of metastable nucleation was developed on the basis of the first principles of statistical physics.

DOI: 10.3103/S106837550802004X

INTRODUCTION

Preparation of micro- and nanoparticles is a new trend in the development of up-to-date methods of electrodeposition of metals (see, for example, [1,2] and references therein). Nucleation or incipient crystallization plays a decisive role in technological processes of making micro- and nanoparticles. Though the entire electrodeposition process is rather complicated, the formation of structures mainly depends on the kinetics of nucleation, which depend on the correct calculation of thermodynamic functions. To this end, the evaluation of the probable dimensions of the particles and their relation to the energy parameters are of primary interest. One may surely conclude that the solution of this problem proposed in [1] is evidently interesting and should be analyzed; generalized; and, probably, completed. This paper is devoted, in particular, to these theoretical problems of kinetics of nucleation process, and its main goal is to generalize our earlier results [3–5] into a unified system and to find the place of this general theory in the solution of the special problem of electronucleation.

The classical approach to the nucleation problem belongs to various degrees to Folmer, Bekker, Duhring, Frenkel, and Borelius. It is essential that, in their works, the kinetics of nucleation were treated as a self-organization process in which the values of the surface and bulk energies of the particle served as a driving force. We provide a simple relationship for the radius of the formed particle (which we cited earlier [6]) without discussing the known Frenkel theory in detail:

$$r_{cr} = K(\sigma/\mu), \quad (1)$$

where σ is the specific surface free energy, μ is the change in the chemical potential during the phase transition (at nucleation), and K is the particle form factor ($K = 1$ for a cylinder and $K = 2$ for a sphere). As we mentioned earlier, Eq. (1) is equivalent in its form to the known Gibbs–Tompson equation. This approach is primarily based on the possibility to rigorously divide the total energy of the system into the surface free energy and the bulk energy. This is a common, though rather conventional, method. The fact that the nucleus can be formed in a heterogeneous way, that is, on the surface of a macroscopic body or in its pores, essentially reduces to changes in the constants in Eq. (1), where the interaction of the cluster surface with the surface of the body is taken into account phenomenologically. The further generalization of the results of the thermodynamic relationships to the kinetic processes reduces to introduction of the equilibrium thermodynamic potential of the growing cluster taking into account Eq. (1) with application of the theory of fluctuations. This is understandable from the first principles, because the kinetics of formation of the nucleus can follow only in the fluctuation way. Hereafter, from the general principles of the fluctuation theory, we obtain the main equation of a more general theory that describes the nucleation phenomenon.

Examination of the kinetic phenomena reduces to the semiqualitative Frenkel consideration, according to which the rate of a stationary flux of formation of the most probable nuclei is defined as

$$J \sim \exp\{-\Delta E_{cr}/kT\}, \quad (2)$$

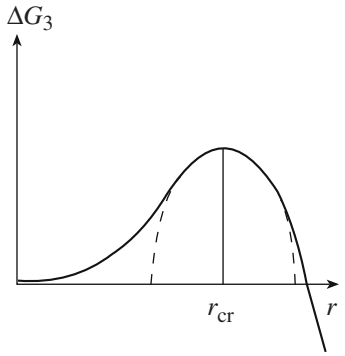

Fig. 1. Form of the function of free energy.

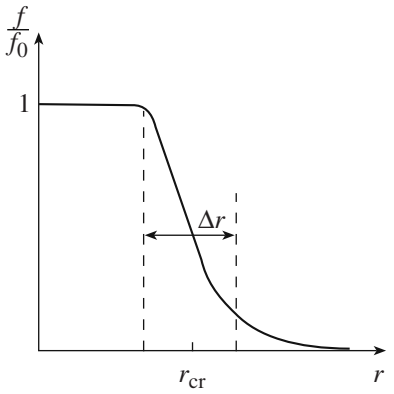

Fig. 2. Ratio of distribution functions f/f_0 vs. the particle radius.

where ΔE_{cr} is the activation energy of the nucleus formation. In Eq. (2), the preexponential factor is omitted, which we do not examine hereinafter. Then, the solution of the problem reduces to the determination of the free energy (see Fig. 1). It is also interesting to qualitatively present the ratio of the probability of a nonequilibrium process f owing to the flux J to the probability of the equilibrium distribution of nucleated particles f_0 vs. the radius of the particles r.

In this approximation, the free energy is defined (if we take into account only low temperatures) as

$$\Delta G_3 \sim \Delta E_{cr}, \tag{3}$$

where ΔE_{cr} is the activation energy of formation of the nucleus, and

$$E_{cr} \sim A(r_{cr})^2 - B(r - r_{cr})^2.$$

In this case, we obtain the simplified Landau theory exactly, which weakly works particularly in the nucleation region (see the Δr interval marked by dashed lines in Fig. 2). That is, particularly in the region where $\Delta r \sim (r - r_{cr})$, the theory cannot predict the probability of the nucleation process.

The present work is envisaged to go beyond the limits of the Landau theory, from which, as was pointed out, the Frenkel theory also follows (and Eq. (1), respectively).

Before proceeding to the general theory, we perform a critical analysis of the previous research. Thus, for example, the main conclusion, which follows from [1], is in fact a modification of the Frenkel theory and, hence, of Eq. (1), which can be now presented in the form where the parameter μ is changed by a respective parameter μ_1, which we write in the form

$$\mu_1 = A_e - A_k, \tag{4}$$

where A_e is the part of the electrochemical energy spent for the generation of the particle and A_k is the disclination energy that initiates the nucleation process (as is noted in [1]). An explicit presentation of these energies in a phenomenological model is given in [1], but note that it remains completely unclear in this approach what part of the electrochemical energy is spent for the formation of the particle. In [3–5], an instanton model was proposed, which involves, for example, microscopic parameters of the system, such as the energy of interaction of atoms in the nanoparticle. It is expedient to compare the results of these approaches, especially taking into account that an instanton model of disclinations already exists [7–8].

1. THERMODYNAMIC APPROACH TO THE NUCLEATION PROBLEM

Note that, earlier, we obtained a set of results similar to those discussed here, though on the basis of a general formal approach in the framework of the model of statistical nucleation [4, 5]. Naturally, the former approach and that proposed here are equivalent, though, methodically, it is interesting to obtain the result on the basis of other general principles, at least with the aim to prove its validity.

The nucleation process is a metastable process in its essence, and it is described as a state of a conventional extremum on a hypersurface of free energy in a multidimensional space. Naturally, the system can leave the specific metastable state and transfer into a state with another minimum overcoming the saddle point on the hypersurface of free energy separating the minima. The reverse processes are also probable. The specified saddle point defines the probability of the metastable processes. From general considerations of the statistical thermodynamics of quasi-equilibrium processes, the probability of this process is defined as

$$W \sim \exp(-Q/kT), \tag{5}$$

where Q is the thermodynamic activation potential, which involves both the activation energy of an elementary act and the energy expenses related to the change in the state configuration. The latter expenses for a number of processes can even exceed the former, but all the expenses are defined by the value of the free energy of the system F in the vicinity of the saddle point,

which, in essence, define the thermodynamic activation potential.

Let us consider a model topology of free energy in a certain generalized form:

$$F = F_n + F_k A/2(S')^2, \quad (6)$$

where F_n is the average value of the free energy near the saddle point as a function of some generalized coordinates of the system (we do not specify the form of the function here), which depends on the external forces that act on the system

$$F_k = A/2(S')^2, \quad (7)$$

and S' is the derivative of the energy state vector (this S vector characterizes the energy state of the "atom" with the specified r coordinate), which is a classical variant of the spin function.

It is convenient to pass from the function of free energy F to the thermodynamic potential Φ adding the function of the chemical potential multiplied by the number of particles. The variation of the thermodynamic potential should be equal to zero (the extremum condition). If we omit the variations of the external forces, which we consider hereafter, the obtained equation takes the form

$$\delta\Phi = \delta\int T(r)dv = 0, \quad (8)$$

this leads to the equation

$$S'' = 0.$$

Let us pass to a cylindrical coordinate system. Assume that the nucleus is a very long cylinder and the dependence of S on the z coordinate can be neglected. We use the variables θ and r as the standard variables of the cylindrical coordinate system instead of the coordinates x and y. Then, the spin function (with the accuracy to a constant) is presented as an angle function $\theta(\rho)$ counted from the axis **z**. The reverse transformation to the Cartesian coordinates has the form $S_x = S\sin\theta$, $S_y = S\cos\theta$. Then, we write the specified part of the free energy in these variables:

$$H_{g,c} = T(r) = A/2\{(\theta')^2 + (\sin\theta)^2/r^2\}, \quad (9)$$

where $\theta(r)$ is the angle between the cylinder axis and the spin vector (the magnetization vector in the theory of micromagnetizm (see [3–12] for more details)), and r is the radial coordinate. The model kinetic energy $T(r)$ is a classical analogue of the exchange (potential) energy in the Heisenberg model for the two-dimensional space (see [3–5, 7–13] for more details). Note, it is not occasional that $T(r)$ coincides in its form with the kinetic energy of the quasiparticle in spherical coordinates. This is associated with the fact that the nonlinear model under consideration admits solutions in the form of quasiparticles (nonlinear waves) called instantons [8–13]. Also note that the quasiparticles (instantons) are not dynamic particles in our case but topological formations [9–11]. Therefore, the kinetic energy $T(r)$ should be assumed to be virtual kinetic energy of the topological instanton.

These equations are nonlinear, but, for the case of a cylindrical particle, they possess an analytical solution, which was obtained for other physical problems [3–12]. For the generality of the consideration, we provide these equations, their solutions, and a detailed graphical analysis of the solutions.

Let us find the variation minimum in the integrand. Then, from (8) and (9), a known nonlinear equation follows

$$\theta''(\rho) + \theta'(\rho)/\rho - \sin\theta\cos\theta/\rho^2 = 0. \quad (10)$$

Here, it is convenient to introduce the relative coordinate $\rho = r/r_{cr}$ [3–5, 7–13] (because the theory should be scale-invariant [9–13]), which changes as $0 < \rho < 1$.

To find a nonhomogeneous solution that physically describes the nucleation, we specify the respective boundary conditions in the following form:

$$\theta(\rho) = 0 \text{ or } \pi \text{ (for convenience, we assume } \theta(\rho) = \pi) \text{ for } \rho = 0;$$
$$\theta(\rho) = \pi/2 \text{ for } \rho = 1. \quad (11)$$

A similar problem was examined earlier [3–5, 7–13], and its analytical solution was presented as

$$\tan\{\theta/2\} = 1/\rho. \quad (12)$$

A solution of this kind is called a two-dimensional soliton or instanton [3–5, 7–13], and it is a rare example of an accurate analytical solution of a nonlinear problem.

Now, the meaning becomes clear of the simplification of the real physical problem (variation of the exchange energy only, which assumes a low-temperature limit in the classical case). Owing to this simplification, an analytical solution can be obtained, which, in fact, only qualitatively corresponds to the real situation because of the simplified model and the zero temperature limit. However, the fact is substantial that, even in this simplified situation, the obtained solution does not allow one to clearly separate the energy of the system into the surface and bulk energy (hereafter, we provide a result that makes this conclusion more obvious); at the same time, one can suppose this conclusion to remain valid when the temperature increases. Consider then a general case that corresponds to the model with an accurate solution. This case allows one to find criteria when Eq. (1) can be adequately used.

It was shown earlier [3–5, 7–13] that the generalization of the model that takes into account electrochemical phenomena can be introduced as an electric field with a specific dependence on the radial coordinate ρ in the form B/ρ^2 (where B is a positive number, and the form of the potential energy we define hereafter). Therefore, by analogy with the problem from [3–5, 7–13], we introduce into consideration an equation in the form

$$\theta_a'' + \theta_a'/\rho - a^2 \sin(\theta_a)\cos(\theta_a)/\rho^2 = 0, \quad (13)$$

where the magnitude a^2 is (by analogy with the problem about a cylinder magnetization [3–5, 7–13]) the ratio of the energy of anisotropy (which, for the sake of certainty, orients $\theta_a(\rho)$ along the cylinder axis) to the constant of the exchange interaction A. That is, we define this parameter by the equation

$$a^2 = B/A. \quad (14)$$

For correlation with the previous statistical model (described by Eq. (9)), we should assume that, for $B = 1$, anisotropy is absent and, for $B > 1$, it appears (for the physical meaning of the anisotropy see below).

The solution to equation (13) takes the form [3–5, 7–13]

$$\tan\{\theta_a/2\} = 1/\rho^a. \quad (15)$$

Note that solution (15) for the tangent of the angle θ_a exhibits a power dependence on the parameter a. Since solutions (12) and (15) can be analytically joined, we further omit the index a at the function $\theta(\rho)$ and consider one general analytical solution.

Shown for illustration is a comparative graphical characteristic, which follows from the two statistical models considered above.

As can be seen in Fig. 3, in the first case (curve *1*, $a = 1$), it is difficult to separate the cylinder volume that can be attributed to the surface energy, because the angle θ changes smoothly as a function of ρ. For curve *2* ($a = 10$), a region can be chosen whose volume constitutes the surface energy of the cylindrical particle. In the framework of our qualitative examination, we conventionally can assume, for example, that the surface layer is counted beginning from $\rho = 0.8$. Making this choice, we only proceed from the graphical shape of curve *2* in Fig. 3, which falls sharply for $\rho > 0.8$. The volume defining the surface energy of the cylinder constitutes 36% of the cylinder volume. When a subsequently increases (curves *3* and *4* for a equal to 50 and 100, respectively), this volume then makes up less than 10 and 5% of the cylinder volume, respectively.

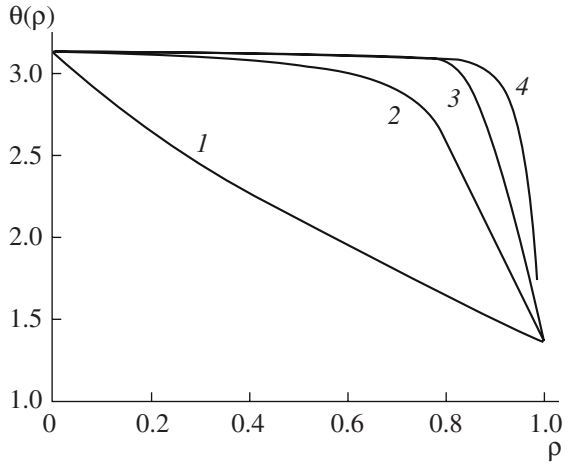

Fig. 3. Families of dependencies of the slope angle of the energy spin relative to the cylinder axis $\theta(\rho)$ (which characterizes the particle energy in the Heisenberg model in the from of the solution to Eq. (15)) vs. the reduced radius ρ of its coordinate and the parameter a, which changes taking the following values: (*1*) 1, (*2*) 10, (*3*) 50 and (*4*) 100 (explained in the text).

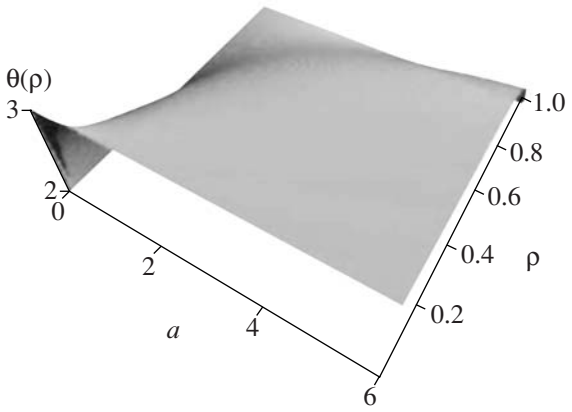

Fig. 4. 3D diagram of the dependence of the spin slope angle $\theta(\rho)$ (that is, "an energy spin" according to its physical meaning) relative to the cylinder axis, which characterizes the energy of the particle in the Heisenberg model, vs. the parameters a and ρ.

Concerning the three-dimensional diagram shown in Fig. 4, it can be clearly seen in it how smoothly the function $\theta(\rho)$ behaves when $a = 1$. On the other hand, when $a > 1$, $\theta(\rho)$ is constant virtually over the entire surface and approaches π. At the end only, when ρ approaches one, the function $\theta(\rho)$ tends to zero. Note that, in the three-dimensional diagram (Fig. 4), for our case, only a values exceeding one have a physical meaning. For a less than one, the solution $\theta(\rho)$ has no physical sense (it is shown only to illustrate the three-dimensional image).

One can conclude that, in the case when

$$a \gg 1, \quad (16)$$

as can be clearly seen in Figs. 3 and 4, the separation of the surface energy and, hence, Eq. (1) with all its consequences become valid. Thus, we can assert, for example, that, in this case, the region where the Landau theory is not applicable should contract (Fig. 2). Since, in a real system, a short-range interaction (in this case, it is defined by the exchange interaction, that is, by the interaction between elementary particles) and a far-range interaction are always present, which here define the anisotropy, the parameter a is the ratio of the far-range energies to the short-range energies (see [9, 10] for more details). Then, we return to a more thorough revision of the concept of the energy of the anisotropy. In the simple model examined here (that only qualita-

tively represents the real situation), a very strong dependence of θ vs. a was obtained. It can be presented as an exponential function of a unitless parameter a.

2. APPLICATION OF STATISTICAL THEORY FOR THE PROBLEM OF NUCLEATION

Prior to examining the specific problem of electrochemical nucleation, it is necessary to perform a brief review of the statistical methods that we already used earlier [3–5] and of their relation with the lattice (discrete) statistical models. There is a vast number of publications on this problem; therefore, we confine ourselves to a short survey only.

In 1925, E. Ising initiated the theory of statistical lattice models. He proposed a model that, in its isotropic version, presents the following Hamiltonian:

$$H_i = -A/2\sum_{i \neq j} s_{zi}s_{zj}, \tag{17}$$

where H_i is the Hamiltonian in the Ising model without an external field, s_{zi} and s_{zj} are the z components of the Pauli matrix (i and j are the numbers of particles (atoms)), and A is the constant of the exchange interaction ($A > 0$ for the case of ferromagnetism). Let us assume for simplicity that this constant does not depend on the particle number; this corresponds to the case when only the interaction between the nearest particles is examined. The meaning of the function A becomes clear when we discuss the covalent bond between two atoms. As is known, the magnitude of this bond exponentially decreases with the increase in the distance between the atoms. Therefore, in the sum of Eq. (2), only the nearest neighboring of "atoms" is taken into account, which is simulated by spin operators. The Ising model is related to the models of magnetic materials (a quantum model of two-dimensional magnetic films, for example). It was also successfully applied to explain the physics of phase transitions in a lattice gas. This allows one to describe binary mixtures, surface adsorption, DNA "melting," and other phenomena where phase transitions can be revealed. However, in a continuum approximation, the given model describes the surface well and is hardly applicable for the description of a cylindrical particle.

For our case, a more complicated model is appropriate (it will be discussed below) proposed by W. Heisenberg in 1928, in which, as differs from (17), the Hamiltonian has the form (for the simplest case of the isotropic exchange interaction and without the operator of the interaction with an external field)

$$H_g = -A/2\sum_{i \neq j} S_iS_j, \tag{18}$$

where, unlike the Ising model, S_i and S_j are represented by three-dimensional spin operators (that is, in the Hamiltonian, a scalar product of the projections of the spin matrices $S_iS_j = s_{xi}s_{xj} + s_{yi}s_{yj} + s_{zi}s_{zj}$ is present). This model is more realistic for a ferromagnet and an atom (in a lattice gas); however, it is difficult to obtain its analytical solution even for a one-dimensional case.

The Heisenberg model in a classical case of continuum approximation, as is shown hereafter, allows one, in particular, to also examine three-dimensional objects in the form of a cylindrical nuclei. Let us briefly substantiate this conclusion.

To obtain a classical analogue of Eq. (18) for a ferromagnetic Hamiltonian, we take an expression for field operators similar to (18)

$$H_g = -1/(2(2\mu_0)^2)\int dv\int A(r-r_1)M(r)M(r_1)dv_1, \tag{19}$$

where a double integration is performed over the volume of the space of the field magnetic operators $M(r)$, which are a classical analogue of spin operators with accuracy to the numerical constant $1/(2\mu_0)^2$, where μ_0 is the Bohr magneton

$$M(r) = 2\mu_0\sum S_1\delta(r-R_1), \tag{20}$$

where R_1 is the radius vector defining the position of the first lattice site ($\delta(r)$ is the Dirac delta function). This analogy is based on the fact that the commutation relations for $M(r)$ and S_1 are the same. Further, we assume the function $M(r)$ to be a classical analogue of the spin operator S. The next step to obtain a classical analogue of Hamiltonian (18) is to expend the function $M(r_1)$ in the Taylor series to the second derivative (with respect to the variable $(r - r_1)$). The first product of $M(r)$ by the zero term of the expansion gives a constant energy shift, which is not interesting in our case. The second product of $M(r)$ by the first term of the expansion gives zero as a result of integration, since each lattice site is a symmetry centre; the integrand possesses the first power with respect to the variable $(r - r_1)$, and we have an integral of an odd function over a symmetric interval.

Only items in the form of $M(r)$ M"(r) give a nonzero input (two primes denote the second derivatives with respect to the coordinates x, y, and z). Further, we integrate by parts and obtain a symmetrical term of the exchange interaction in the form

$$H_{g,c} = A/2\sum (S_k')^2, \tag{21}$$

where A is the exchange interaction in the continuum approximation, and S_k is the classical analogue of the spin function component (k is x, y, and z). Further, as the given function, we assume the energy state of the particle with the coordinates x, y, and z (in the model of a continuum medium). Since we examine a classical analogue of the theory, the function S_k has a continuous spectrum. We pass to a cylindrical coordinate system (similar to [3–5]) and assume the nucleus to be a very

long cylinder, so the dependence of S on the z coordinate can be neglected. We use the variables θ and r as the standard variables of the cylindrical coordinate system instead of the variables x and y. Then, the spin function is represented (with accuracy to a constant) by an angle function $\theta(\rho)$ counted from the axis z. The reverse transformation to the Cartesian coordinates has the form $S_x = S\sin\theta$, $S_y = S\cos\theta$. Write down the Hamiltonian in these variables using the conversion coefficients (Lame coefficients)

$$H_{g,c} = T(r) = A/2\{(\theta')^2 + (\sin\theta)^2/r^2\}, \qquad (22)$$

where $\theta(r)$ is the angle between the cylinder axis and the magnetization vector and r is the radial coordinate. The model kinetic energy $T(r)$ is a classical analogue of the exchange (potential) energy in the Heisenberg model for a two-dimensional space. Note, it is not occasional that $T(r)$ coincides in its form with the kinetic energy of the particle in spherical coordinates. This is related with the fact that the examined nonlinear model admits solutions in the form of quasiparticles (nonlinear waves) named instantons. Also note that, because the quasiparticles (instantons) are not dynamic particles in our case but topological formations, the kinetic energy $T(r)$ should be treated as the virtual kinetic energy of a topological instanton. That is we obtain the equation that was earlier obtained by other methods.

Hence, we return to Eqs. (10) and (13) and their analysis, which was already performed in the previous section, and to solutions in the form of (12) and (15).

3. CALCULATION OF THE FREE ENERGY OF CYLINDRICAL PARTICLES

To evaluate how the free energy changes in the direction from the centre of the particle to its surface, let us examine the change of the free energy of a cylindrical particle layer by layer. The formula for energy that we used to obtain the equation of motion has the form

$$E(\rho) = T + W, \qquad (23)$$

where T is defined by Eqs. (9) and (22), and $W = B/2(\sin\theta^2)/\rho^2$ is the anisotropy that represents the potential energy in our case.

Substituting the solution to Eqs. (10) and (13) in the form of (12) and (15) in the expression for T and W, we obtain

$$T = W \qquad (24)$$

(note that this is a consequence of the virial theorem) and

$$T + W = 2A(a^2/\rho^2)[(\rho)^{2a}/(1+\rho^{2a})^2]. \qquad (25)$$

Then, we analyze Eq. (25) both analytically and graphically. For a particular case, for example, when $a^2 = 1$, we obtain the relationship

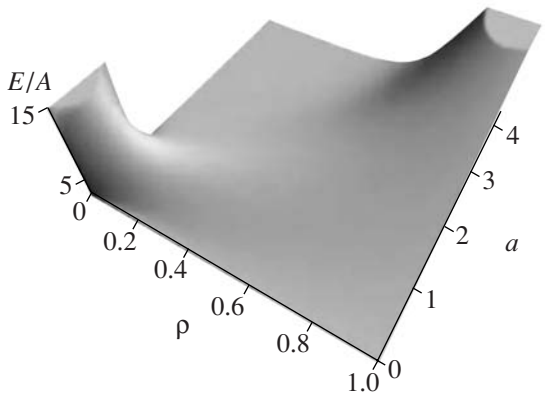

Fig. 5. 3D diagram of the energy dependence vs. the parameters a and ρ.

$$T_1 + W_1 = 2A/(1+\rho^2)^2, \qquad (26)$$

from which it can be seen that the energy tends to A (for $\rho^2 = 1$) on the cylinder surface. In the case when $B > 0$, the energy on the cylinder surface tends to Aa^2 (that is to B), and this tendency is revealed more drastically for greater B values. Hence, in particular, one can consider this parameter to be a respective parameter for the thermodynamic surface energy involved in Eq. (1). Note, it is denoted as σ there.

The energy inside the particle tends to $2A$ in the case of (26); however, in the same passage to the limit, it tends to zero in the case of (25). This specific step of the free energy is characteristic for a phase transition that occurs in the system in the case when an infinitely small anisotropy appears. Similar phase transitions are known, and here they were obtained as a result of the analysis of rather simple expressions.

Below, we provide graphs that clearly demonstrate the existence of phase transitions.

Note that, in the diagrams in Figs. 5 and 6, a nonphysical case is shown when the parameter a is less than one. Therefore, the maximum in the region $0 < a < 1$ has no physical meaning. The energy step has a quite different real meaning, which we interpret as a phase transition for $a > 1$.

As was clearly demonstrated, the consequences of the discussed model reduce to the fact that the energy may be divided into the bulk energy and the surface energy if an anisotropy exists in the system, which substantially exceeds the isotropic short-range exchange interaction. In this case, a steplike energy $E(\rho)$ increase occurs in the system, which corresponds to the phase transition related to the nucleation of the particle.

For example, regarding the physical nature of the examined anisotropy, we can note (see, for example, [5]) that, in the case of electrochemical crystallization, this anisotropy can be induced by the distribution of the electric field in the near-electrode layer, because the dimensions of the particles become compa-

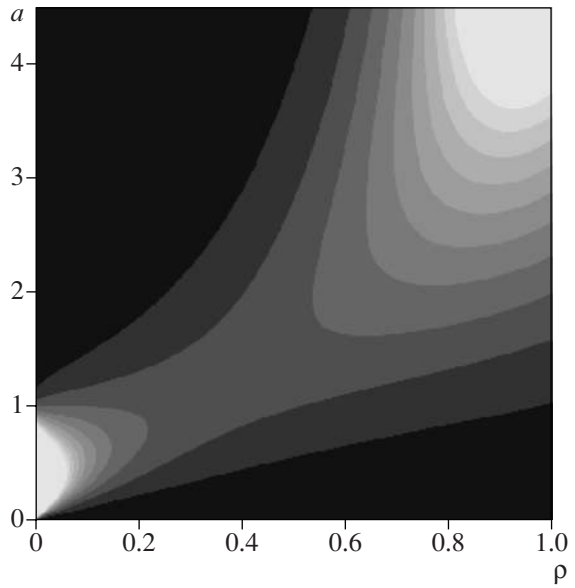

Fig. 6. Diagram of levels of the energy dependence vs. the parameters *a* and ρ.

rable with the dimensions of the layer. Note that ideas to examine the near-cathode layer as a source of free energy of the particles were proposed earlier (see, for example, [14]). This idea was quantitatively implemented in [5]. The present paper is, in particular, devoted to the idea of the possibility to transfer from the traditional approach (with complete separation of the energy into the surface and bulk energy) to the general case when this rigorous separation is not necessary.

CONCLUSION

With decreasing of the dimensions of a body, the thermodynamic state of its surface plays a greater role in the description of its thermodynamic state. The simplest model given above demonstrates that, in this case, it becomes more and more difficult to separate the thermodynamic functions into the surface and bulk quantities. We have found at least a qualitative criterion that reduces mathematically to a rather large parameter *a* representing the ratio of far-range energies to short-range energies when it is possible to perform a similar separation.

Topological ideas applied, in particular, in the theory of field and elementary particles and later in the theory of magnetism have lead to a number of new results in statistical physics as well. One of these results obtained in [3] is a fundamental solution in the form of instanton waves [3, 5, 9–13], which are already used to describe the physical behavior of magnetic materials [15, 16] and nematic liquid crystals [7].

While investigating the problems of applied character, in particular, magnetization of a cast amorphous microwire (that is, a long cylinder with its diameter of micro- and nanodimensions), these ideas allowed obtaining definite new results [9–13]. The aforementioned ideas were also transferred to the study of nucleation phenomenon [3, 5]; they are presented in the most full scale in the given paper.

For example, in this research, as far as was possible, we did not examine the mathematical problems discussed in [9–13]. Here, the greater attention was given to the application of these mathematical solutions to the problems of electrochemical nucleation.

A weakness of the examined model is that a cylindrical symmetry was used instead of a spherical symmetry. We had to examine only examples of very elongated nanoparticles whose geometrical properties can be well approximated by an infinite cylinder. Actually, such particles are often obtained by an electrochemical method. Synthesis of sphere-shaped particles is also interesting. However, in the case of spherical symmetry, it is not possible to obtain analytical solutions, but we put forward hope for the development of approximate numerical calculation methods.

ACKNOWLEDGMENTS

This work was supported by the Program RFFI-Moldova, grant no. 06.11CRF.

REFERENCES

1. Yasnikov, I.S. and Vikarchuk A.A., Evolution of Formation and Growth of a Cavity in Pentagonal Crystals of Electrolytic Origin, *Fizika Tverdogo Tela*, 2006, vol. 48, no. 8, pp. 1352–1357.
2. Khachaturyan, A.G., *Teoriya fazovykh prevrashchenii i struktura tverdykh rastvorov* (Theory of Phase Transitions and Structure of Solid Solutions), Moscow: Nauka, 1974.
3. Baranov, S.A., Statistical Model for Analyzing Nucleation in the Electrochemical Processes, *Surf. Eng. Appl. Electrochem.*, 2005, no. 4, pp. 1–4.
4. Baranov, S.A., The Theory of Nucleation, *Moldavian Journal of the Physical Sciences*, 2006, vol. 5, no. 2, pp. 209–210.
5. Baranov, S.A., Gamburg, Yu. D., and Dikusar, A.I., Kinetic Model of Electrochemical nucleation, *Surf. Eng. Appl. Electrochem.*, 2007, vol. 43, no. 2, pp 107–109.
6. Gamburg, Yu.D., *Elektrokhimicheskaya kristallizatsiya metallov i splavov* (Electrochemical Crystallization of Metals and Alloys), Moscow; Yanus-K, 1997.
7. Chandrasekhar, S., Liquid Crystals, Cambridge, New York: Cambridge Univ. Press, 1977.
8. Katanaev, M.O., Geometrical Theory of Defects, *UFN*, 2005, vol. 175, no. 7, pp. 705–733.
9. Belavin, A.A. and Polyakov, A.M., Metastable States of a Two-Dimensional Isotropic Rerromagnetic, *Pis'ma Zh. Eksp. Teor. Fiz.*, 1975, vol. 22, no. 10, pp. 503–506.
10. Perelomov, A.M., Instanton-Type Solutions in Chiral Models, *Usp. Fiz. Nauk*, 1981, vol. 134, no. 4, pp. 578–609.

11. Rozhkov, S.S., Topology, Manifolds and Homotopy: Main Concepts and Applications to n-Field Models, *Usp. Fiz. Nauk*, 1981, vol. 134, no. 4, pp. 578–609.
12. Kosevich, A.M., Ivanov, B.A., and Kovalev, A.S., Neline-inye volny namagnichennosti. *Dinamicheskie i topologicheskie solitony* (Non-Linear Waves of Magnetization. Dynamic and Topological Solitons), Kiev: Naukova Dumka, 1983.
13. Izyumov, Yu.A. and Skryabin, Yu.N., *Statisticheskaya mekhanika magnitouporyadochennykh sistem* (Statistical Mechanics of the Systems with Magnetic Ordering), Moscow: Nauka, 1987.
14. Frumkin, A.N., Petrii, O.A., and Damaskin, B.B., The Concept of the Charge of an Electron and the Lippman Equation, *Elektrokhimiya*, 1970, vol. 6, no. 4, pp. 614–630.
15. Baranov, S.A. and Vazquez, M., A Thin Microwire with Negative Magnitostriction in a Zero Magnetic Field, *Pis'ma Zh. Eksp. Teor. Fiz.*, 2004, vol. 30, no. 23, pp. 36–38.
16. Baranov, S.A., Laroze, D., Vargas, P., Vazquez, M., On Micromagnetic Theory of Thin Cast Amorphous Microwires, *Physica B*, 2006, vol. 372, pp. 320–323.

ISSN 1068-3755, Surface Engineering and Applied Electrochemistry, 2008, Vol. 44, No. 2, pp. 106–109. © Allerton Press, Inc., 2008.
Original Russian Text © L.A. Kuz'micheva, Yu.V. Titova, A.I. Maksimov, 2008, published in Elektronnaya Obrabotka Materialov, 2008, No. 2, pp. 35–38.

ELECTRICAL PROCESSES IN ENGINEERING AND CHEMISTRY

Investigation of Atmospheric-Pressure Gliding Discharge Action on an Electrolyte Solution

L. A. Kuz'micheva, Yu. V. Titova, and A. I. Maksimov

Institute of Solution Chemistry, Russian Academy of Sciences, ul. Akademicheskaya 1, Ivanovo, 153045 Russia

E-mail: jvt@isc-ras.ru

Received November 1, 2007

Abstract—The effect of atmospheric-pressure gliding discharge action on an electrolyte solution was studied. The hydrogen peroxide yields in the solutions were defined after the discharge treatment, as well as the pH and elecrtoconductivity values. Gliding discharge was shown to be more effective than glow discharge for H_2O_2 formation in the electrolyte solution.

DOI: 10.3103/S1068375508020051

INTRODUCTION

Interaction between atmospheric-pressure gas-discharge plasma and electrolyte solutions initiates chemical redox processes in the liquid phase and can find application for solving various applied problems (e.g., for purification and sterilization of water, solutions, and articles). While selecting the discharge type for practical purposes, the chemical activity of the later and the features of the devices designed for the implementation should be taken into consideration.

Atmospheric-pressure nonstationary gliding discharge between two metal electrodes, considerably allowing reduction of the erosion of the electrodes, was offered by A. Chernikhovskii [1]. Research of the given discharge type chemical action when two metal electrodes are close to a solution surface was carried out in work [2]. Gliding discharge in a metal electrode–solution surface system was used for the first time in [3, 4]. In these works, the oxidizing action of gliding discharge on dye solutions and salts of variable valency metals was studied.

The basic role in initiation of redox reactions is played by formation of primary chemically active particles H, OH, e_{solv} in the solution superficial layer under the action of ionic bombardment. As the results presented in works [5, 6] show, in spite of the very small thickness of the solution superficial layer (hundredths of a micron), the primary active particles have time to react within this thin layer. As a result, oxidizing processes can proceed with the assistance of OH radicals in the cathode spot and of these radicals' dimerization product—hydrogen peroxide—within the rest of the volume of the solution [5]. The ratio between the contributions of these paths depends on the rate constants of the corresponding reactions.

The object of the work is to study the efficiency of hydrogen peroxide accumulation as a steady secondary oxidizing agent under the action of gliding discharge on an electrolyte solution as compared with glow discharge. The changes in the physical and chemical characteristics of the solution as a result of the glow discharge treatment have been investigated as well.

EXPERIMENTAL

Glow discharge was induced between the anode—a point in the gas phase—and the solution surface. The

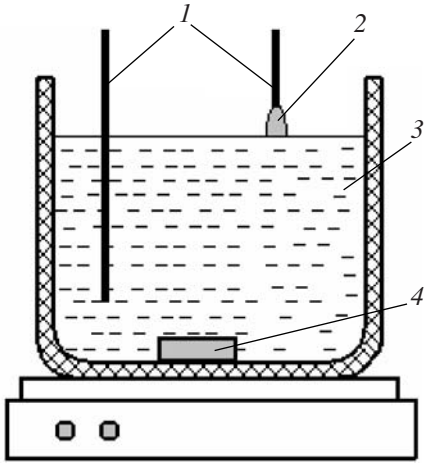

Fig. 1. Glow discharge cell. (*1*) electrodes; (*2*) plasma zone; (*3*) electrolyte solution; (*4*) magnetic stirrer.

scheme of the cell is presented in Fig. 1. The distance from the anode to the solution surface was 0.4 cm.

The gliding discharge struck between an electrode of variable curvature and the electrolyte solution (Fig. 2). An air stream moved above the solution surface in the direction of increasing the discharge gap. The plasma zone was formed in the field of the minimal gap and shifted under the action of the air stream alongside the electrode until the interelectrode distance exceeded the critical one at which the discharge quenched. Immediately, the discharge struck again within the least gap zone. The process repeated and became quasiperiodic. The interelectrode distance was 4–8 mm.

The concentration of hydrogen peroxide in the solution was defined by the iodometric titration method using the standard procedure with addition of $(NH_4)_2MoO_4$ as a selective catalyst of the H_2O_2 reaction with iodide-ion [7]. As the process solutions, distilled water and solutions of Na_2SO_4 with concentrations of 0.001 and 0.01 mole/l served. The volume of the process solution was 100 ml, and the discharge currents were 10 mA. Simultaneously with the H_2O_2 concentration, the pH and electroconductivity of the solutions were controlled.

RESULTS AND DISCUSSION

The dynamic current–voltage characteristics of gliding and glow discharge with an electrolyte cathode were obtained (Fig. 3, 4). They indicate that the nature of these discharges is similar and that their influence on the physicochemical properties of the solution may be expected to be similar as well. Really, changing the electrolyte solution pH under the action of gliding discharge is practically similar to the action of the glow one (Fig. 5) with the only difference that, under otherwise equal conditions, the influence of the gliding discharge on the solution increases the electrolyte acidity and, correspondingly, the solution electroconductivity to a greater extent. Reducing the solution pH under the action of glow discharge, as shown in work [8], is unequivocally connected with synthesis of nitrogen oxides in the plasma zone and their dissolution in water to afford nitric acid. In the case of gliding discharge, in the presence of an air stream, the formation of nitrogen oxides in the gas phase proceeds more intensively and, therefore, their greater amount can pass into the liquid phase. However, their significant quantity is carried by the same stream out the cell; therefore, the difference in the acidity of the solutions treated with glow and gliding discharge is insignificant.

Accumulation of hydrogen peroxide under the action of glow and gliding discharge was investigated for two modes: 1—the solution was stirred only after the termination of the plasma treatment, and the average concentration of H_2O_2 formed during the effecting discharge was defined; 2—the solution was stirred dur-

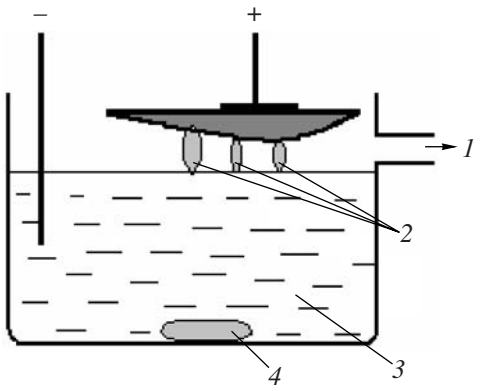

Fig. 2. Gliding discharge cell. (*1*) air stream; (*2*) plasma zone moved with air stream; (*3*) electrolyte solution; (*4*) magnetic stirrer.

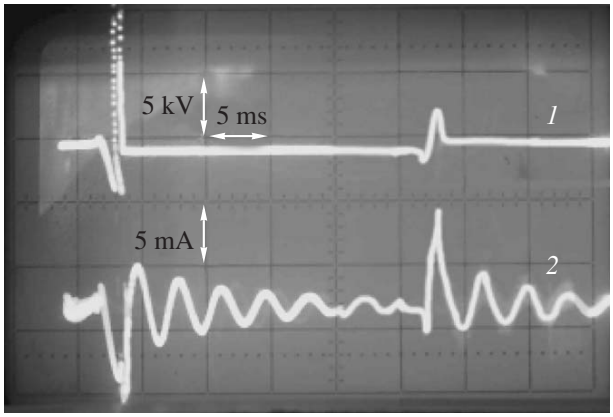

Fig. 3. The dynamic current – voltage characteristics of the gliding discharge.

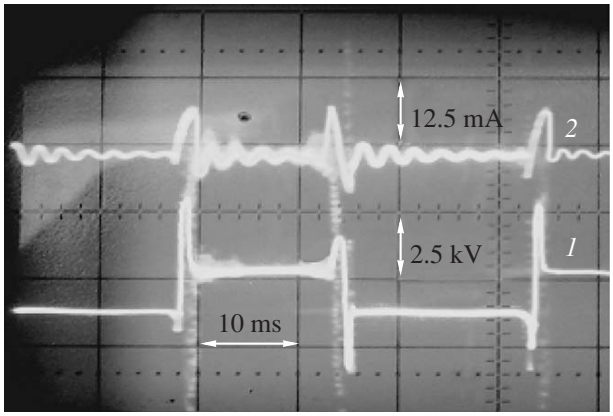

Fig. 4. The dynamic current – voltage characteristics of glow discharge.

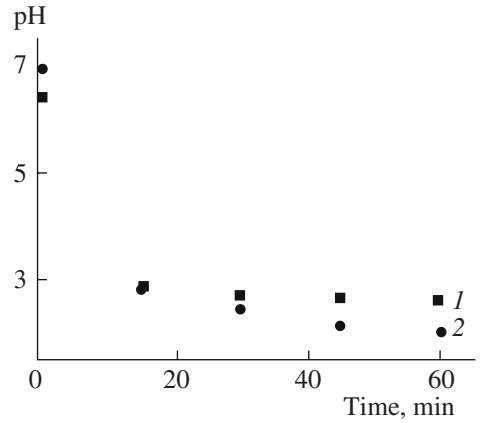

Fig. 5. Changing solution acidity under the action of gliding (*1*) and glow (*2*) discharges. Solution volume – 100 ml; discharge current – 10 mA; electrolyte – water.

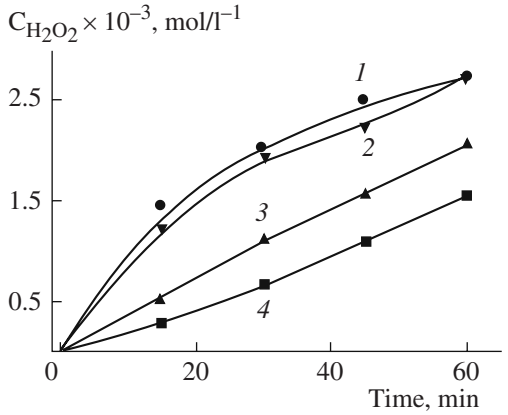

Fig. 6. Accumulation of hydrogen peroxide in water under the action of plasma treatment; (*1*) and (*2*) gliding discharge without stirring and with stirring, respectively; (*3*) and (*4*) glow discharge without stirring and with stirring, respectively. Solution volume—100 ml; current—10 mA.

ing the plasma treatment, and, after its termination, the average concentration of H_2O_2 was defined. Stirring the solution during treatment appeared to exert an essential influence on the accumulation of hydrogen peroxide only in the case of glow discharge.

The kinetic curves of H_2O_2 accumulation in water are presented in Fig. 6. From the initial regions of the kinetic curves for various solutions, the initial rates of hydrogen peroxide formation and H_2O_2 current outputs (the quantity of hydrogen peroxide molecules formed under the action of ionic bombardment of the solution surface counting upon one singly charged falling ion) were calculated. The data are presented in the Table. It may be noted that, when gliding discharge is used, the yield of H_2O_2 considerably exceeds the yield of hydrogen peroxide in the plasma–solution system with the stationary glow discharge. It is shown in works [3, 4] that, at the initiation of oxidizing processes (in this case, by oxidation of organic dye and formation of MnO_2 from Mn^{2+}), the efficiency of gliding discharge appears to be essentially higher than the glow one. Most likely, it was connected with the fact that, at the initiation of the gliding discharge, a lot of hydrogen peroxide is formed in the solution.

We assume that such a difference is caused by the processes of H_2O_2 decomposition in the solution superficial layer under discharge action. Glow discharge is stationary, and hydrogen peroxide is formed in the cathode spot zone, which is permanently exposed to plasma action. If the solution is not stirred up, then H_2O_2, formed in the field of the cathode spot, decomposes under the discharge action, without having time to diffuse into the solution volume. If the solution is stirred up, then a considerably larger amount of hydrogen peroxide is transferred from the cathode area into the solution volume depending on the mode of stirring. Since gliding discharge (unlike the glow one) is quasi-periodic, the zone of plasma contact with the solution permanently moves. The H_2O_2 that is formed has time to diffuse from the cathode area into the solution vol-

Initial rates of formation and current output of hydrogen peroxide in solutions under action of plasma treatment

Solution	Initial rate of H_2O_2 generation, mol/(l s)	Initial output of H_2O_2, mol/Φ	Experimental conditions
Glow discharge			
H_2O	3.002×10^{-7}	0.289	Without stirring
H_2O	6.427×10^{-7}	0.619	With stirring
0.001 M Na_2SO_4	3.778×10^{-7}	0.364	Without stirring
0.01 M Na_2SO_4	3.347×10^{-7}	0.322	Without stirring
Gliding discharge			
H_2O	1.531×10^{-6}	1.474	Without stirring
H_2O	1.333×10^{-6}	1.284	With stirring
0.001 M Na_2SO_4	1.250×10^{-6}	1.204	Without stirring
0.01 M Na_2SO_4	9.351×10^{-7}	0.900	Without stirring

ume before the discharge strikes in the former place. Thus, it is possible to draw the conclusion that the efficiency of the H_2O_2 accumulation in the considered plasma–solution systems is defined mainly by the processes of hydrogen peroxide decomposition under the discharge action, which should be taken into account while selecting the discharge type and developing individual plasma–solution devices for practical problem solving.

REFERENCES

1. Rusanov, V.D., Petrusev, A.S., Potapkin, B.V., Fridman, A.A., Chernikhovskii, A.A., and Shapel', O.Zh., O vozmozhnosti podderzhaniya sil'no neravnovesnoi plazmy v dugovykh razryadakh atmosfernogo davleniya (About Possibility of Strongly Nonequilibrium Plasma in Atmospheric-Pressure Arc Discharges), *Dokl. Akad. Nauk*, 1993, vol. 322, pp. 306–308.
2. Janowski, T. and Stryczewska, H.D., Ranaivosoloarimanana, A., Czernichowski, A., Industrial trials of the glidarc plasma reactor, *12th Int. Symp. on Plasma Chemistry,* Minneapolis, 1995, vol. 2, pp. 825–830.
3. Janca, J., Kuzmin, S., Maximov, A., and Titova, J., Czernichowski, A., Investigation of the chemical action of the gliding and "point" arcs between the metallic electrode and aqueous solution, *Plasma Chemistry and Plasma Processing*, 1999, vol. 19, no. 1, pp. 53–67.
4. Maximov, A.I. and Titova, J.V., The Investigation of Chemical Action of Gliding and Glow Discharges Between Metallic Electrode and Aqueous Solution, *Elektron. Obrab. Mater.*, 2002, vol. 213, no. 1, pp. 64–68.
5. Maksimov, A.I., Titova, Yu.V., and Kuz'micheva, L.A., Kineticheskaya model' okislitel'nykh reaktsii, initsiiruemykh v rastvorakh elektrolitov tleyushchim razryadom (Kinetic Model of Oxidative Reactions Initiated in Electrolyte Solutions with Glow Discharge), *Gorenie i plazmokhimiya* (Combustion and Plasmochemistry), 2005, no. 3, pp. 247–250.
6. Kutepov, A.M., Zakharov, A.G., and Maksimov, A.I., Vakuumno-plazmennoe i plazmenno-rastvornoe modifitsirovanie polimernykh materialov (Vacuum–Plasma and Plasma–Solution Modification of Polymer Materials), Moscow: 2004.
7. Skoog, D. and West, D., *Osnovy analiticheskoi khimii* (Fundamentals of Analytical Chemistry), Moscow: Mir, 1979, vol. 1, p. 97.
8. Kuz'micheva, L.A., Titova, Yu.V., and Maksimov, A.I., Vliyanie gazofaznykh protsessov, initsiiruemykh tleyushchim razryadom, na svoistva rastvorov elektrolitov (Influence of Gas Phase Processes Initiated with Glow Discharge on the Properties of Electrolyte Solutions), *Elektron. obrab. mater.*, 2006, no. 3, pp. 148–152.

ISSN 1068-3755, Surface Engineering and Applied Electrochemistry, 2008, Vol. 44, No. 2, pp. 110–114. © Allerton Press, Inc., 2008.
Original Russian Text ©V.D. Kalugin, O.V. Sidorenko, N.S. Opaleva, V.E. Keilin, I.A. Kovalev, 2008, published in Elektronnaya Obrabotka Materialov, 2008, No. 2, pp. 39–44.

ELECTRICAL PROCESSES IN ENGINEERING AND CHEMISTRY

Method of Obtaining Superconducting Phase $Nb_3Ge_xAl_{1-x}$ by Thermal Diffusion in the Electrolytically Formatted Multilayer Metal Structure Nb/Ge/Al

V. D. Kalugin, O. V. Sidorenko, N. S. Opaleva, V. E. Keilin, and I. A. Kovalev

Kharkov V.N. Karazin National University, Scientific Research Institute of Chemistry, pl. Svobody 4, Kharkov, 61077 Ukraine

E-mail: Alexandre.D.Rochal@univer.kharkov.ua

Received October 22, 2007

Abstract—Formation of the stable superconducting (SC) phase of intermetallide $Nb_3Ge_xAl_{1-x}$ ($x \cong 0.2$–0.30) by thermal annealing of multilayer structures of Nb/Ge/Al-like specimens under T = 1213 ± 20K in vacuum has been studied. The multilayer structures have been obtained by the method of electrochemical concretion of Ge and Al layers on Nb (Nb is a structural foundation). The critical (I_c) currents that flow inside the specimens at the temperature of He in magnetic fields $H >> H_{C2(Nb)}$ have been measured; the critical densities of the current (j_c) have been rated. The nature of the (j_c) dependence on the time of annealing, the magnetizing force H(Tl), the layer thickness of Ge -h_{Ge} (mcm) (at $h_{Al} \approx$ const), and the layer thickness of Al-h_{Al}(mcm) (at $h_{Ge} \approx$ const) have been determined. A conclusion on the technological expediency of the electrochemical method of obtaining multilayer Nb/Ge/Al-like structures for the purpose of SC intermetallides formation by means of the thermal-diffusion method has been reached.

DOI: 10.3103/S1068375508020063

According to [1], the intermetalloid compound Nb_3Ge with an A-15-type structure is a superconductor (SC) characterized by a high temperature of transition into the T_c (22.7–23.2 K) superconducting state, a high value of the critical current density of $j_c > (3–5) \times 10^6$ A/cm^2, a rigid hardness, and a tolerance to spontaneous decomposition; i.e., it does not react with the environmental components (O_2, H_2O) in a cycling range of 4.2–298 K and preserves its critical parameters. All the known methods of obtaining intermetallide Nb_3Ge are expensive and require making use of special devices that ensure high cooling rates (1073–1273 K c^{-1}) for latching the SC-phase at $T < 800$ K. Therefore, we have taken another way of SC-phase formation on the basis of Nb and Ge, namely, the introduction into the initial two-component system (Nb-Ge) of a third component (a metal) that fulfills the function of a stabilizer of the Nb_3Ge SC-phase and simultaneously somewhat decreases its critical parameters [1].[1] In connection with using such a kind of approach, which was tested on metallurgical specimens, for Nb_3Ge SC-phase stabilizing, it is necessary to examine the diagrams of the state and composition: the critical temperature T_k of alloys of (Nb) *d*-element with *p*-elements of III (Al) and IV (Ge) of the main subgroups of the periodic table [1].

The characteristic feature of the Nb–Al alloys diagram is the presence of "low" and "high" (T_c) of the alloys with a small (up to 18 at %) Al content and the average one (in the range of 10–38 at %). For Nb–Al alloys, the SC-phases have a maximal $T_c \approx 18$ K, an A-15 structure, and an Nb_3Al composition. The superconductivity of Nb alloys with a small Al content (up to 10–15%) also results from Nb's own superconductivity in magnetic fields with $H \ll H_{C2(Nb)}$ (where H is the magnetic induction or magnetic field intensity); therefore, the Nb's own SC can be excluded by carrying out measurements at $H \gg H_{C2(Nb)}$.

In the process of plating an Al metal stabilizer over a very thin layer of Ge, which stabilizes the metastable SC-phase of the metal, a thermal diffusion of the atoms theoretically must lead to Nb_xAl_y SC-phase formation, the T_k of which is ≅6–7 K (the Al content is 10–20 at %). Therefore, after the process of Al plating on Nb and the subsequent annealing, there forms the SC-phase, which in He_{zhe} is necessarily characterized by a definite value of the I_c critical current.

According to the diagram of the state for the Nb–Ge system, the presence of a metastable Nb_3Ge SC-phase with the greatest degree of probability appears in the range of the Ge concentration of ≈10–30 at %. How-

[1] Kalugin, V.D., Sidorenko, O.V., Opaleva, N.S., Keilin, V.E., Kovalev, I.A., Electronnaya obrabotka materialov, 2008, no. 2, pp. 39–44.

ever, ts phase gets entirely destroyed under the small cooling rate conditions of the specimens after annealing, and no other SC-phases were found to appear at all at concentrations of Ge > 30 at. Therefore, there is a very high probability that the Al stabilizing effect of the metastable phase (under the condition of Al and Ge atoms diffusion into the Nb mass) occurs in the same Ge concentration range (up to 25–30 at %). Such a hypothesis is confirmed by the idea of the existence of the intermediate SC-phase of $Nb_3Ge_{0.2}Al_{0.8}$ with T_c equal to 20 K [2]. In accordance with the Nb–Ge diagram, the Ge concentration in the $Nb_3Ge_{0.2}Al_{0.8}$ phase corresponds to 6.6–10.0 at %; i.e., at the presence of Al, superconductivity occurs in a phase with a small content of Ge (up to 10 at %) or there stabilizes a metastable Nb_3Ge phase at temperatures lower than 1273 K. The latter appears to be quite real, since the effect of stabilizing at the presence of an active metal is necessarily accompanied by Ge-component loss (Ge concentration reduction in the SC-phase) and its transfer into a phase that lacks superconducting properties in He_{zhe}.

Thus, the diagram analysis results concerning the state and composition of T_c alloys of Nb–Al and Nb–Ge made us add to the experimental program of SC-phase formation, which comprises the initial structures of Nb/Ge and Nb/Ge/Al and the tests on the formation of Nb/Al/Ge and Nb/Al, in order to prove by our experiments the fact of formation of SC-phases of various chemical nature both in the presence and in the absence of a Ge sublayer on Nb.

In the technology of a multilayer deposition of different metals including a component of the SC-phase, electrochemical methods were used (ECM). In the process of thermal diffusion treatment of multilayer metal structures, there form thin (~10^{-6} m) layers of SC-phase from Nb_3Ge intermetallides (a metastable phase—MSP) and $Nb_3Ge_xAl_{1-x}$ (a stable phase—SP). The processes of electrolytical formation of a multilayer metal structure include a successive electrodeposition on the Nb base (a constructional frame of a specimen) of the second component of a metal SC-phase Ge and of the third component (Al) from nonaqueous solutions of electrolytes. The SC-phase formation of $Nb_3Ge_xAl_{1-x}$ occurs in the process of high temperature annealing (at $T = 1213 \pm 20$ K) in vacuum with a period of annealing equal to 10–36 hours.

The task of determination of certain transformations among the components Nb, Ge, and Al during the annealing with formation of intermetallides of various composition was not our aim, since it is not new. In [2], one can find thorough information on the fact that, for the metallurgic specimens of Nb–Ge–Al (Al is a stabilizer for the SC-phase of Nb–Ge), the only stable SC-phase has proved to be $Nb_3Ge_xAl_{1-x}$ (at $x \approx 0.2$–0.3), which has every reason for existence with availability of phase X-ray analysis. On the basis of the present data, it has become obvious that, should the multilayer metal system Nb–Ge–Al formatted according to the "layer-by-layer" method of electric deposition be exposed to thermal annealing, the occurrence of $I_c(j_c)$ at a temperature of 4.2 K (He_{zhe} definitely reveals the presence of only the $Nb_3Ge_xAl_{1-x}$ phase itself (at $T_c \approx 20.6$ K), since no other phases of triple intermetallides are superconducting. By the way, such an implicit statement cannot be referred to the Nb_3Sn SC-phase, because, according to the diagram of the Nb–Sn state, intermetallide SC-phases exist within the entire range of compositions [1].

Quite naturally there arises a question about the role of the Nb base as a superconductor in the Nb/Ge/Al multilayer system and the $Nb_3Ge_xAl_{1-x}$ SC-phase, since T_c(Nb) = 9–10 K (at H_{C2} up to 0.2 Tl) [1]. Also, one can actually consider that the I_c values for the triple superconducting phase Nb–Ge–Al may belong first of all to Nb. To avoid such a fatal error, in the experiment, it is possible by carrying out the measurements of the critical I_c current of the specimens on the basis of Nb in magnetic fields with H and big values of the second critical magnetic field for Nb (H_{C2}). I_c (Nb) reduces to zero when $H_{crit.}(H_{C2})$ is for Nb ≥ 0.2 Tl [1]. Only under these conditions of the experiment (H = 1–7 Tl) may I_c be referred entirely to the $Nb_3Ge_xAl_{1-x}$ superconducting phase. By the way, such a means of Nb-base SC exclusion was successfully used previously by the authors of [3] for the system Nb–Sn (Nb is a structural foundation, a carrier of a thin Nb_3Sn SC layer). All the above mentioned show that the results of I_c measurements for the specimens of Nb/Ge/Al in the fields of 1–7 Tl can only be referred to the $Nb_3Ge_xAl_{1-x}$ SC-phase.

The purpose of the present investigation is the experimental determination of practical realization of electrochemical methods of Ge and Al deposition from previously studied electrolytic germanizing [4–8] and aluminizing solutions [9, 10] for the creation of multilayer metal structures and their following thermal diffusion transformation into the SC-phase (of $Nb_3Ge_xAl_{1-x}$ type) with regard to the measurement data of the critical current (I_c) values and the calculated critical current density (j_c) values of the SC-phase in magnetic fields of various intensity (H).

For the experimental investigations, we used plate-type Nb specimens 0.2×10^{-3} m thick. The transition width between the two base foundations with apertures for rigid mounting of electric contacts of the measuring circuit was 5×10^{-2} m. After the stages of electrodeposition on Nb–Ge–Al, the multilayer structure annealing, and the successive plating of compensating (stabilizing) copper and tin layers in accordance with the recommendations in [3], the obtained specimens theoretically represent multilayer systems that can be written as follows in their sectional view:

1) Nb/Nb_3Ge (MSP)/$Nb_3Ge_xAl_{1-x}$ (SP)/Ge/Al/Cu/Sn (the initial structure—i.s.: Nb–Ge–Al),

2) Nb/Nb_3Al (SP)//$Nb_3Ge_xAl_{1-x}$ (SP)/Ge/Cu/Sn (i.s.: Nb–Al–Ge);

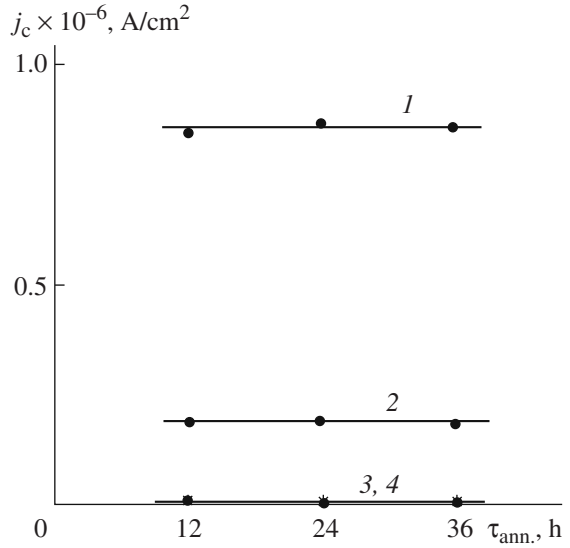

Fig. 1. The values of the critical current density j_c of the $Nb_3Ge_xAl_{1-x}$ SC-phase obtained by annealing of various multilayer metal structures with regard to the $\tau_{ann.}$ annealing time. The magnetic field intensity H = 1Tl; h(Ge) ≈ 1.5×10^{-6} m; h(Al) ≈ 1.0×10^{-6} m. Structures: *1* – Nb/Ge/Al (Cu/Sn); *2* – Nb/Al/Ge (Cu/Sn); *3* – Nb/Ge (Cu/Sn); *4* – Nb(Cu/Sn).

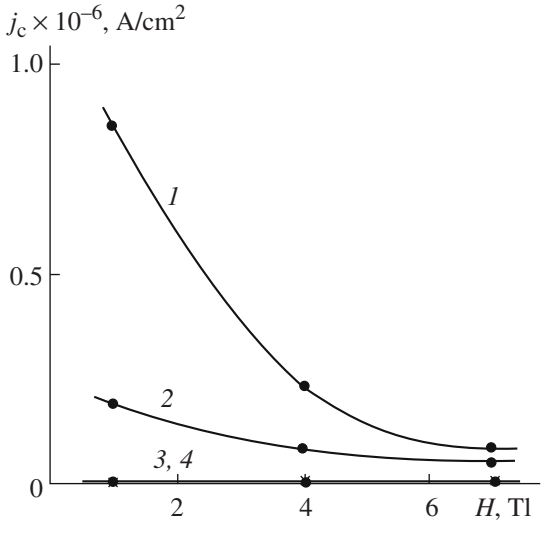

Fig. 2. The values of the critical current density j_c of $Nb_3Ge_xAl_{1-x}$ SC-phase obtained by annealing of various multilayer metal structures in magnetic fields of different intensity H. $\tau_{ann.}$ = const = 24 h; h(Ge) ≈ 1.5×10^{-6} m. Structures: *1* – Nb/Ge/Al (Cu/Sn); *2* – Nb/Al/Ge (Cu/Sn); *3* – Nb/Ge (Cu/Sn); *4* – Nb (Cu/Sn).

3) Nb/Nb_3Ge/Cu/Sn (i.s.: Nb–Ge), and

4) Nb/Cu/Sn (i.s.: Nb).

For the critical current I_c measurements, we used a device with a high direct current source, which was described in [3]. The current–voltage characteristics were read in the external magnetic field up to 7 Tl (transversely to the specimen surface) at a liquid helium temperature of 4.2 K.

In connection with the discovered possibility of electric deposition of Ge from alcohol solutions containing additives of H_2O (up to 5–8%) [4, 6, 8], the technological conditions of this process are performed in a bath with a Ge anode at the contact of the electrolytic solution with the atmosphere. The Ge anode use ensures stabilizing of the Ge(IV) concentration in the solution.

In the case of the aluminizing process on Ge or Nb from a xylene solution, it is shown in [10] that, in order to initiate a discharge of less energy-consuming Al(III)-containing electroactive particles, to generate a voltage drop in the bath, to ensure realization of the process under conditions of contact of the electrolytic solution with the atmosphere, and to provide for the solution lifetime extension (to prevent it from separation), it should be periodically electrolytically processed by Al electrodes. The initial electrolytic processing was ~5A che/el (i_k = 2 mA/cm^2).

Thus, the technologic conditions of the multilayer Nb/Ge/Al structure formation comprise complex results of the laboratory methods of Nb specimens preparation prior to the electric deposition of Ge and Al from the alcohol and xylene solutions, correspondingly, along with the developed additional technological stabilizing means of the electrolytic solution compositions and determination of the possibility of Ge, Al electrodeposition processes realization in the baths under conditions of the solution–atmosphere contact (a considerable cost reduction of the technologic process).

The conditions of the annealing process of Nb articles (with Ge, Al coatings) in a vacuum furnace have been studied well [1]; therefore, they are not presented in this paper.

At the annealing stage, across the Nb-base surface and in the mass of the multilayer Nb/Ge/Al structure, there forms the SC-phase. After the annealing stage, on the surface of the SC-phase of the work specimen, it is necessary to apply the compensating (Cu) and tin (and then indium) layers (for compensating for the SC breakdown current and ensuring reliable electric contact during the I_c measuring process) [3].

The electric deposition of the Cu layer comprises baths for degreasing, rinsing, copper coating (successively from the pyrophosphate and sulfuric electrolytic solutions), final rinsing, and drying of the article [3]. Electrolytic tinning is performed in accordance with [3] recommendations.

The calculation results of the j_c critical current density of the $Nb_3Ge_xAl_{1-x}$ intermetallide SC-phase for various multilayer structures are presented in Figs. 1–4. One can see from Fig. 1 that, for a pure Nb and Nb/Ge structure (without a stabilizing Al layer), the j_c values for both the (Nb) structural foundation and the Nb_3Ge metastable phase are equal to zero. These results explicitly show that the SC-phase of the Nb_3Ge intermetallide that is formed in the process of annealing

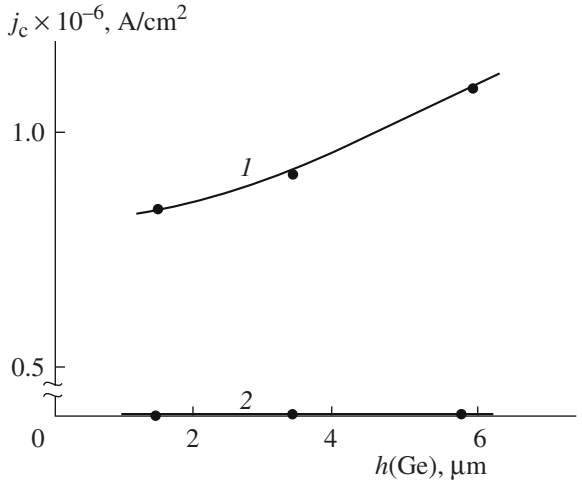

Fig. 3. The values of the critical current density j_c of $Nb_3Ge_xAl_{1-x}$ SC-phase obtained by annealing of various multilayer metal structures with regard to the thickness of the Ge-layer h(Ge) in a magnetic field of intensity H = 1Tl. $\tau_{ann.}$ = 12 h, h(Al) ≈ (10–12) × 10^{-6} m. Structures: *1* – Nb/Ge/Al (Cu/Sn); *2* – Nb/Ge (Cu/Sn).

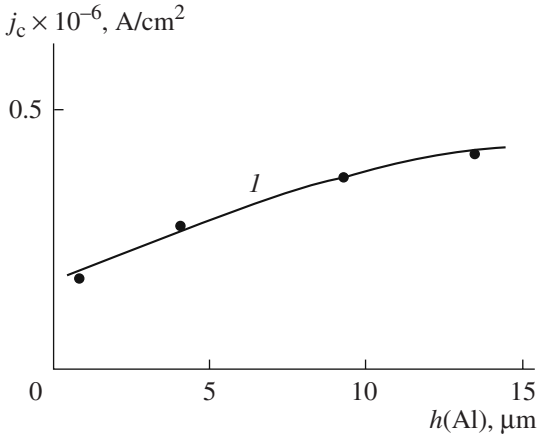

Fig. 4. The change of the critical current density j_c of the multilayer Nb/Al/Ge structure with regard to the Al-layer thickness (h(Al)) in a field of 1 Tl $\tau_{ann.}$ = 12 h; h(Ge) ≈ 7.7 × 10^{-6} m.

structure 3 (Fig. 1) destructs entirely while being slowly cooled, reaching $T \approx 878 \pm 20$ K [1, 2]. The tests with Nb specimens (the annealing takes place under standard conditions) in fields of 1–7 Tl also display the absence of the Nb SC-state at 4.2 K. As follows from Fig. 1, the presence of Al (a stabilizer of the Nb_3Ge SC-phase) in a multilayer structure results in the occurrence (after annealing) of SC properties (dependencies 1, 2; Fig. 1) that weakly change with increasing of $\tau_{ann.}$ At the same time, the succession of Ge and Al deposition on Nb is of major importance for the j_c values. In the case when the metal stabilizer (Al) is plated on Ge, Al obviously exhibits certain screening (protective) properties (besides the SC-phase stabilizer function) towards the Ge layer. The SC-phase formation rate and its mass increase are much greater in this case, so the j_c values in the case of system 1 are 4 times systematically more than for the SC-phase that forms in structure 2. It is not improbable that, in the annealing process of structure 2, there are mainly forms of the Nb_3Al SC-phase whose critical current density is several times lower than that for the phase of $Nb_3Ge_xAl_{1-x}$ [5]. The above-mentioned weak change of the j_c value character with the increase of $\tau_{ann.}$ shows that, already at $\tau_{ann.}$ = 12 h, the surface Nb layer and the Ge, Al layers interdiffuse and further annealing becomes unnecessary for the technological process.

The results shown in Fig. 2 confirm a well-known regularity for the metal superconductors concerning the j_c decrease with the H increase [3]. It can be roughly estimated that, in the fields H = 1–7 Tl, the system *1* j_c decreases by 12–13 times and, for the system *2*, by 3.5–4.0 times. It is evident that, in the absence of the possibility for SC-phases formation (dependencies *3*, *4*; Figs. 1 and 2), there is no need to say anything about the character of the dependence on τ_{ann} and H.

The presented experimental data show (Figs. 1, 2) that identification of the SC-phase of the $Nb_3Ge_xAl_{1-x}$ intemetallide by the criterion of the presence of superelectric conductivity (by means of measuring j_c), provided this property is fully suppressed in the (Nb) base, is explicitly possible in magnetic fields of H = 1–7 Tl.

The process of formation of intermetallide stabilized SC-phase in the regime of the component thermal diffusion can be traced according to the j_c value increase, depending on the Ge-layer thickness (the Ge_0 atoms concentration), under conditions of the thickness permanency of the stabilizing (Al) layer in a multilayer initial structure. Figure 3 presents the results of the j_c change with the increase of h(Ge) at h(Al) = const, which confirm that the formation rate of the Al stabilized intermetallide phase is close to a linear dependence (curve *1*). When the multilayer Ge-containing system lacks the stabilizing Al layer (dependence *2*), the critical current of the SC-phase is absent, since it is metastable at $T \le 800$ K and, in the process of slow cooling up to room temperatures, it is not observed.

The kinetics of formation of Nb_3Al and $Nb_3Ge_xAl_{1-x}$ intermetallides in the multilayer Nb/Al/Ge structure is obviously crucially influenced by the process of Nb_3Al formation, since, in the case of the behavior of the $Nb_3Ge_xAl_{1-x}$ phase formation process, the values of j_c should be close to the values of j_c = (0.8–1.1) × 10^{-6} A/cm^2 (Fig. 3, dependence *1*) typical for this intermetallide. However, (see Fig. 4) the actual j_c values for the annealed Nb/Al/Ge system turn out to be three times less than for the case when a metal stabilizer is applied on the Ge sublayer. This allows one to claim that, in the case of the Nb/Al/Ge system, there mainly takes place the Nb_3Al intermetallide SC-phase formation process. The quantity of $Nb_3Ge_xAl_{1-x}$ phase turns out to be small; therefore, on the curve of Fig. 4 at

$h(\mathrm{Al}) > 10 \times 10^{-6}$ m, a tendency of constancy of j_c on h(Al) is traced. In the last event, it is necessary, perhaps, to increase the period of annealing of the specimens in order to form a more compact mass of Nb_3Al alloy, which is accompanied by the additional increase of the j_c value.

The results of Figs. 3 and 4 represent a special interest for the technology of electrochemical Ge and Al coating formation on Nb. It follows from the results that, in order to exclude ballast Ge and Al metals (unused for SC-phase formation) on Nb articles, it is recommended to apply Ge and Al layers of optimal thickness $h(\mathrm{Ge}) \approx (3–6) \times 10^{-6}$ m and $h(\mathrm{Al}) \approx (10–12) \times 10^{-6}$ m for ensuring j_c values of the $Nb_3Ge_xAl_{1-x}$ intermetallide phase (where $x \cong 0.2–0.3$) at the level of values of $(0.8–1.1) \times 10^6$ A/cm^2. Under the conditions of technological realization on Nb specimens of suggested thicknesses of Ge and Al coatings, the latter are determined by the time of electrochemical deposition (with constancy of all the rest of the process parameters) [8, 10].

Thus, on the basis of the laboratory investigation results, there have been proposed the technological conditions of the electrochemical method for Nb/Ge/Al multilayer structure formation from nonaqueous electrolytic solutions, and a thermal diffusion processing of these specimens has been carried out for the purpose of $Nb_3Ge_xAl_{1-x}$ intermetallide SC-phase formation. In the magnetic fields of various intensity (at $H \gg H_{C2(Nb)}$), the transport currents I_c have been measured and the critical j_c current densities of $Nb_3Ge_xAl_{1-x}$ superconducting phase layers have been rated (for instance, at H = 4Tl, $j_c = 0.24 \times 10^6$ A/cm^2).

Experimentally defined regularities of the j_c value change of the $Nb_3Ge_xAl_{1-x}$ SC-phase in accordance with the type of the initial multilayer metal structure and the time of annealing allow one to conclude that the electrochemical method of the initial structure formation (a successive electric deposition of Ge and Al from nonaqeous media on Nb sublayers) is expedient and more available and therefore fit for practical implementation in the production of articles and devices used in the regime of superconductivity at the temperatures of liquid hydrogen (20.3 K) and liquid helium (4.2 K) or cycling in the temperature range of 4.2(20.3)–298 K.

REFERENCES

1. Savitskii, E.M., Efimov, Yu.V., Kruzhlyak, Ya., et al., *Fiziko-khimicheskiye osnovy polucheniya sverkhprovodyashchikh materialov* (Physical and Chemical Fundamentals of Obtaining Superconducting Materials), Moscow: Metallurgiya, 1981, p. 480.
2. Zalikman, A.N., Korshunov, B.G., Elyutin, A.V., and Zakharov, A.M., *Niobii i tantal* (Niobium and Tantalum), Moscow: Metallurgiya, 1990, p. 296.
3. Kalugin, V.D., Pereverzev, E.B., Kozinets, V.V., Kovalev, I.A., and Pavin, D.B., Influence of Electrolyte Nature of Niobium Tinning on Superconducting Phase Formation and its Current Carrying Property, *Sverkhprovodimost'. Phys. Chem. Tech.*, 1992, vol. 5, no. 8, pp. 1534–1540.
4. Opaleva, N.S., Sidorenko, and O.V., and Kalugin, V.D., Electrolytic Processes in Alcohol Aqueous Solutions of Germanitizing. *Vopr. Khim. Khim. Tekhnol*., Dnepropetrovsk: UDKHTU, 1999, no. 1, pp. 259–261.
5. Pereverzeva, E.B., Sidorenko, O.V., Opaleva, N.S., Larin, V.I., and Kalugin, V.D., Elektroliticheskoe osazhdenie component sverkhprovodyashchikh faz intermetallidov so strukturoi A-15 (Electrolytic Deposition of Superconducting Phase Components of A-15 Structure Intermatallides), *Tesisy dokladov Mezhdunarodnoi konferentsii i vystavki "Elektrokhimiya, gal'vanotekhnika i obrabotka poverkhnosti"* (Abstracts of Papers of Int.Conf. and Exhibition "Electric Chemistry, Galvanic Technichs and Surface Treatment"), Moscow: MGU, 2001, p. 190.
6. Kalugin, V.D., Naumenko, T.A., and Svyatskaya, T.N., Physico-Chemical Analysis of Ethylene-glycol Solutions of Germanitizing and the Kinetics of the Process on Niobium cathode. *Ukr. Khimi. Zh*., 1995, vol. 61, no. 10, pp. 108–114.
7. Sidorenko, O., Opaleva, and N., Larin, V., *Kinetichni ta tekhnologichni parametry protsessu elektrolitichnogo osazhdennya germaniyu na niobii zi spirtovykh rozchiniv z dodatkami vody* (Kinetic and Technological Parameters of Electrolytic Depositon of Germanium on Niobium from Alkohol Solutions with Water Additives), L'viv: *Visnik L'vivs'kogo universitetu, Seria khimichna*, issue 42, Ch. 2, 2002, p. 48–51.
8. Sidorenko, O.V., Larin, V.I., and Opaleva, N.S., Elektroliticheskoe osazhdenie germaniya iz spirtovykh rastvorov s dobavkami vody (Electrolytic Deposition of Germanium from the Alcohol Solutions with Water Additives), *Visnik Natsional'nogo Tekhnichnogo Universitetu "Kharkivskii Politekhnichnyi Institute"*. Kharkiv: NTU "XPI", 2006, no. 13, pp. 160–167.
9. Sidorenko, O.V., Opaleva, N.S., and Larin, V.I., Kineticheskie parametry korozionno-elektrokhimicheskikh protsessov na alyuminii i ego splave v rastvorakh elektrolitov razlichnoi prirody (Kinetic Parametres of Corrosive Electric Chemical Processes on Al and its Alloy in Electrolytic Solutions of Various Nature), *Vestn. Khark. Nats. Univ.* Khimiya, 2002, issue 8 (31), no. 549, pp. 176–181.
10. Sidorenko, O.V., Larin, V.I., and Opaleva, N.S., Osobennosti kinetiki i predstavleniya o mekhanizme protsessa elektroliticheskogo alyuminirovaniya v ksilol'nykh rastvorakh (Peculiarities of Kinetics and Ideas on the Mechanism of the Process of Electrolytic Aluminizing in Xylene Solutions), "*Sistemi obrobki informatsii"*. Kharkiv: Kharkivskii Universitet Povitryanykh Sil, 2006, issue 2(51), pp. 116–127.

ISSN 1068-3755, Surface Engineering and Applied Electrochemistry, 2008, Vol. 44, No. 2, pp. 115–122. © Allerton Press, Inc., 2008.
Original Russian Text © V.N. Tsurkin, Ya.V. Kreptiuk, V.M. Grabovyi, Yu.N. Degtev, N.K. Gumanenko, A.V. Ivanov, 2008, published in Elektronnaya Obrabotka Materialov, 2008, No. 2, pp. 45–54.

ELECTRICAL PROCESSES IN ENGINEERING AND CHEMISTRY

Simulation of the Physical Processes in Liquid Metal at Electrohydropulse Treatment and Its Complexing with Magnetodynamic Treatment of Melt

V. N. Tsurkin, Ya. V. Kreptiuk, V. M. Grabovyi, Yu. N. Degtev, N. K. Gumanenko, and A. V. Ivanov

Institute of Pulse Processes and Technologies, National Academy of Sciences of Ukraine, Oktyabr'skii pr. 43-a, Nikolaev, 54018 Ukraine

E-mail: iipt@iipt.com.ua

Received October 25, 2007

Abstract—By the method of simulation using transparent liquids, physical processes in metallic melts during electrohydropulse treatment and in complexation with magnetodynamic treatment are explored. The value of the rate of moving cavitation clouds and rates of nonstationary hydrodynamic streams at electrohydropulse treatment are determined, and the efficiency of the waveguide immersion at a depth of 1/3 the height of the liquid column in the reservoir is confirmed. The dependence of the cavitation area volume on the parameters of the complex treatment is found. The schemes of the complex treatment that provide the maximal degree of gas removal from the model liquid are determined.

DOI: 10.3103/S1068375508020075

INTRODUCTION

Technological methods of out-of–furnace melt treatment are considered as techniques of liquid metal preparation for casting and as one of the tools for controlling the quality of cast products. Taking into account the multifunctionality of these methods, it is necessary to abide by the principle of physicochemical integration of the melt treatment processes at their technological differentiation [1]. Algorithms for product quality control are constructed at the decision-making level more efficiently if more experimental data on the functional dependences between the internal structure-kinetic changes in the metal and the external structure-forming parameters of the treatment are accumulated.

Joint research carried out earlier at the PTIMA and IPPT of the National Academy of Sciences of Ukraine has shown that complex out-of-furnace melt treatment in one technological module, including magnetodynamic treatment (MHDT) and electrohydropulse treatment (EHPT), may be successfully applied in cast production for liquid metal preparation for casting [2, 3]. A scheme of the complex metal loading used in real conditions of MHDT and EHPT is shown in Fig. 1. At EHPT, discretely repeating high-power polyfrequency pressure pulses are introduced into the melt. Its functional capabilities are determined by multifactor interdependent acoustic and hydrodynamic processes proceeding in the melt in the form of volume acoustic cavitation and hydrodynamic flows [4, 5]. Their role is crucial in obtaining in such treatments such effects as homogenization and finishing of the melt and reconstruction of its structure up to the atomic one [4, 6]. The processes taking place in the melt at MHDT partially coincide with those proceeding at EHPT; however, they develop by other mechanisms [7].

Earlier, in works [2, 3], the physical and technological capabilities of a module constructed on the principle of combination of MHDT and EHPT have been studied. The efficiency of the complex treatment was

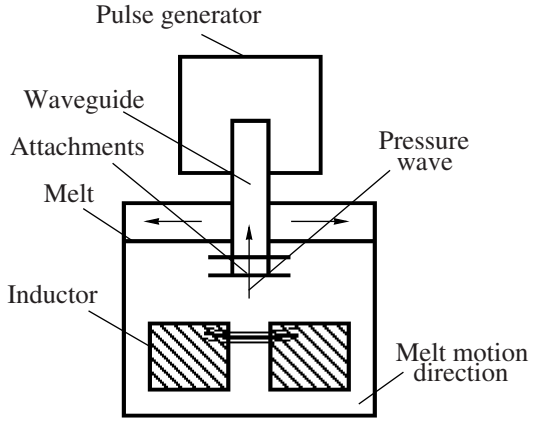

Fig. 1. Scheme of the complex melt treatment (MHDT + EHPT).

studied in experiments with application of the metal-science analysis techniques for examination of cast samples. This approach allows estimating the treated metal quality; however, it does not give direct data on the physical processes taking place in the liquid in the course of the complex treatment. Thus, we find it relevant to obtain additional experimental information, which will not only allow understanding the mechanisms of the complex impact on the liquid medium but will also be a base for further construction of algorithms for control of these physical processes and, therefore, the cast product quality.

In the present work, the problem was solved by the method of physical simulation using a transparent liquid. As the model medium, we selected water heated to 50°C, which is often used for solution of the problems of physical simulation of high-temperature metallurgical processes. Here, it should be noted that complete simulation of hydrodynamic and acoustic processes in liquid metal faces serious difficulties that do not allow constructing a set of basic dynamic similarity criteria accepted in hydrodynamics and acoustics. In the majority of cases, there are no reliable experimental data on the most important (in this statement of the problem) properties of liquid metals and alloys; experimental confirmations of the self-similarity of the processes with respect to one or another similarity criterion are absent. There are no science-based data on the cooperative action of the forces appearing in nature (inertial; induction; hydrodynamic; forces of gravity, pressure, viscosity, and of surface tension); this complicates the determination of the conditions of simulation compatibility. As was mentioned in [8], such an uncertainty allows considering models to be analogous, not similar to the original; that is, when there is a possibility to recalculate the data obtained on the model to the data of nature by virtue of similarity criteria and selected scales. Nevertheless, even partial satisfaction of the complete set of basic similarity criteria allows prediction of scenarios of the process proceeding in nature according to the data of simulation studies with accuracy to their analogy.

Let us analyze the similarity capabilities of the processes under study.

As was shown earlier [3, 7], the results of melt treatment depend on schemes of liquid metal circulation in the MHD-facility, its temperature T, and the rate G, as well as on the EHPT parameters (the single pulse stored energy W_0 and the pulse repetition frequency f). As is mentioned in [9], the EHPT efficiency may be increased using attachments on the waveguide face–end. A key role is assigned to them in the formation of the volume acoustic cavitation zone and its geometrical sizes depending on the area of the piston disturbing the liquid. At invariable energy parameters of EHPT and the waveguide face–end area S_B, an attachment of an area of $S_H > S_B$ will allow increasing the volume of the cavitation cloud formation zone. However, an excessive increase of S_H due to an increase of the adjoined liquid mass will lead to a decrease of the rate and value of the waveguide face–end displacement; this will weaken the cavitation formation effect. Besides, two or more attachments placed at certain distance from each other will allow obtaining a turbulation zone between them due to coupling of compression and tensile waves. Thus, it is possible to obtain the effect of an acoustic pump favoring additional loading of the melt.

The above-stated conditions were used as a basis for construction of simulation stands. The experiment involved two stages of studies; this significantly reduced the total number of expensive experiments necessary for accumulation of statistics and allowed considering the processes characterizing each of the used methods of treatment individually using the differentiation principle. At the first stage, only physical processes at EHPT were studied. At the second stage, the processes of the complex treatment MHDT + EHPT were investigated.

SIMILARITY CONDITIONS

The geometrical similarity was reduced to the condition of geometrical scale equality due to maintenance of the equality of the sizes of the waveguide, the treated reservoir, and the active zone of the MHD-facility for the model and real life. Equality to one of the rate scale was provided in a similar way due to maintenance of equality of the linear rate of circulation (m/s) in the MHD-facility channel of real life and the model and equality of the rates of the waveguide face–end motion. The time scale was provided by comparison of the characteristic periods of time, for example, the time of the pressure pulse action at EHPT in nature and in the model at equal energy parameters of the EHPT.

The dynamic similarity was considered for each of the basic hydrodynamic similarity criteria.

The Strouchal number Sh characterizes the inertial hydrodynamic forces appearing at nonstationary motion

$$\mathrm{Sh} = L/u_0 t, \qquad (1)$$

where L are the sizes of the bodies, m; u_0 are the characteristic rates of the bodies, m/s; and t are the characteristic periods of time, s.

The above-mentioned simulation conditions provided equality of $\mathrm{Sh_M}$ and $\mathrm{Sh_H}$. From now on, the indexes "H" and "M" show an attribute to nature or to the model.

The Froude number is considered at wave formation on the surface; however, since, in our case, only hydrodynamic and acoustic processes in the melt volume depth were studied, the Froude criterion was not taken into account.

The Euler number Eu takes into account the correlation of the forces of pressure and inertia. It is not determining for separation-free motion. In the case of the

Table 1. Physical properties of natural alloys near the melting point

Alloy	ρ, kg/m^3	η, mN s/m^2	σ, J/m^2	σ/ρ, m^3/s^2
Iron based alloys	6600–8170 7390	3.8–6.3 5.15	1.65–1.90 1.78	2.4×10^{-4}
Aluminum based alloys	2380–2410 2400	1.0–1.8 1.4	0.85–0.95 0.9	3.7×10^{-4}
Pure aluminum	2386	1.3	0.914	3.8×10^{-4}
Pure iron	7050	5.4	1.856	2.6×10^{-4}

Note: The spread of the reference data is given above the line, and the average value is given below the line.

Table 2. Physical properties of water at various temperatures

t, °C	20	30	40	50	60	80
ρ, kg/m^3	0.9982	0.9952	0.9922	0.9902	0.9882	0.9718
η, mN s/m^2	1004	829	655	562	470	357
σ, J/m^2	72.58	70.99	69.41	67.72	66.04	62.50

appearance of the cavitation processes, it may be reduced to the cavitation number κ [8, 10]:

$$\kappa = 2\frac{P_\infty - P_\Pi}{P_a}, \quad (2)$$

where P_∞ is the static pressure of the undisturbed medium, P_Π is the pressure inside the cavitation bubble, and P_a is the acoustic wave pressure.

The correspondence of P_∞ for the model and nature was taken in the form $P_{\infty H} = P_{\infty M}$.

The value of P_Π for water is determined by the saturated vapor pressure [10] and, for nature, by the gas pressure, which may exceed the saturated vapor pressure by orders of magnitude. Therefore, in our opinion, the comparison of the pressure values in a bubble in water and a melt is a speculative problem. The acoustic pressure is determined by the correlation

$$P_a = \rho C u_0, \quad (3)$$

where ρ is the medium density, and C is the sound velocity.

It is technically impossible to provide the equality of the acoustic impedances ρC of the model and natural liquids at equality of the piston motion rates u_M and u_H. Thus, it is also impossible to provide equality of κ_M and κ_H at geometrical and time scales equal to one.

The Weber number We is the ratio between the surface tension forces and the inertial forces, which is determined in studies of the dynamics of flushes, splashes, capillary processes, and cavity formation; it is equal to

$$We = \sigma/(\rho u_0^2 L), \quad (4)$$

where σ is the surface tension at the liquid–gas interface.

Since the geometric scale is equal to one, the abovementioned conditions provided the equality $We_M = We_H$.

The equality of the Reynolds numbers Re, in our case, was provided by the equality of the dynamic viscosities of the model and nature $\eta_M = \eta_H$ in the relation

$$Re = \frac{u\rho D}{\eta}, \quad (5)$$

where D is the diameter of the MHD-facility channel, and u is the liquid motion rate.

Let us add that the hydrodynamic situation in the melt volume satisfied the condition $M < 1$, where M is the Mach number.

For observation of the mentioned similarity criteria, there were analyzed the ratios of the following characteristics of the properties of the natural situation and the model: the dynamic viscosity, density, and surface tension. For metal melts, the values of these properties were selected at the melting temperature according to [10–14] (Table 1), and their average values were used in the calculations.

The same properties for water are given in Table 2.

Thus, the data of Tables 1 and 2 show that, under the condition of equality to 1 of the scales of the geometry, time, and the rate for the water heated in the temperature range of 35–60°C and the melt near the melting point, the equalities of the Re, Sh, and We numbers are satisfied. It is impossible to provide equality of the E_u number. That is, it is impossible to obtain complete dynamic similarity under the selected conditions.

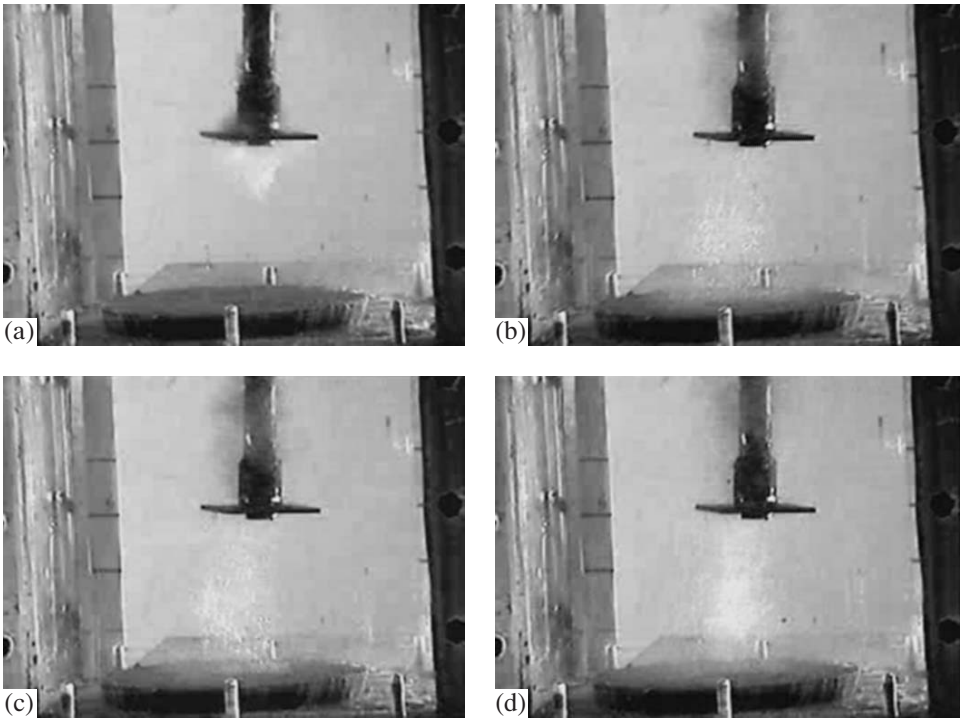

Fig. 2. Physical processes in the model liquid at EHPT (single pulse dynamics): (a) 0.05 s; (b) 0.25 s; (c) 0.5 s; (d) 0.6 s.

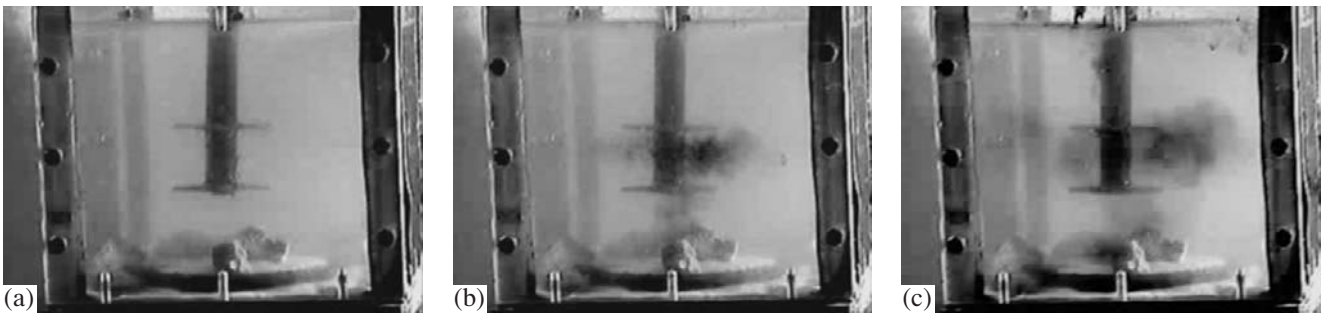

Fig. 3. Characteristic "throwing" of colored liquid at EHPT: (a) 0 s; (b) 2 s; (c) 4 s.

FIRST STAGE EXPERMENTAL RESULTS AND DISCUSSION

In the composition of the experimental stand for simulation of the physical processes in the melt at EHPT, the ladle with the melt was replaced by a transparent chamber filled with water (Figs. 2 and 3). There were applied waveguides of diameters of 50 and 20 mm with attachments of various diameters welded on the face–end and the ones with two attachments spaced at the value of their diameter. The distance from the waveguide face–end to the chamber bottom was varied. For obtaining a more complete picture of the processes taking place during EHPT, at first the treatment was realized with pure water and then sand and fireclay particles were placed on the chamber bottom and the liquid was colored. It was specified that W_0 = 1.25 kJ and f = 1.5 Hz; the treatment duration was 1 min. Videotaped footage was digitized by the program DrDivX11 and was block-by-block searched by virtue of the program Light Alloy 2.9.

Results of the first-stage experimental studies have shown that the attachment on the waveguide face–end significantly activates the cavitation processes and macroflows with their maximum level corresponding to the ratio between the attachment diameter and the waveguide diameter ~2.5. The characteristic motion of the liquid at a single pulse is shown in Fig. 2. One can observe how the cavitation cloud formed by the fed pulse (Fig. 2a) is thrown to the bottom of the treated reservoir (Figs. 2b and 2c). In the time ~0.6 s, the cavitation cloud starts to decompose (Fig. 2d).

The water coloring allowed us to estimate the rates of flows from the waveguide face–end to the chamber bottom and to find that pronounced turbulent flows appear between the two attachments spaced at the value of their diameter. Above the upper attachment and below the lower attachment, with a certain time lag, there appear intense cavitation zones consisting of large bubbles with diameters up to several millimeters. At the very first pulse from the attachment zone, the intense "throwing" of the colored liquid to the bottom and sidewards with a rate of about 0.25 m/s is observed (Fig. 3). Further motion of the colored liquid front occurs with a rate of 0.05 m/s.

At the frequency of the pulse repetition $f = 2$ Hz, the time of complete turbidity of the treated reservoir with water did not exceed 30 s. One can estimate the time of stirring of the metallic liquid that fills the metallurgical reservoir of the same volume using the relation

$$m = \frac{\pi d^2}{4}\rho u, \quad (6)$$

where m is the water mass in the chamber, and d is the characteristic size of the reservoir.

Taking into account the similarity scales, one can calculate that the metal melt with the volume equal to that of the model liquid will be stirred for a time exceeding 30 s by a factor of ρ_H/ρ_M. Thus, the melt of aluminum alloy will be stirred for 72 s and that of iron–carbon alloy, for 210 s. An increase of the frequency of the pulse repetition will decrease this time pro rata.

Using the sand and fireclay placed on the chamber bottom, the depth of the electrohydropulse impact was studied. Visual observation has shown that a pronounced cavitation cloud under the waveguide face–end is thrown to the chamber bottom with a rate of about 0.25 m/s. Immediately after the first pulse, a crater is formed in the sand and gas is actively evolved from the fireclay pieces, even from those located not under the waveguide. After several pulses, their shaking over the whole chamber bottom area is observed. This indirectly confirms the fact of gradual involvement of the whole liquid volume into the flow process; the shaking of the fireclay pieces counts in favor of the availability of nonstationary flows.

It is known from experience of EHPT application in cast production that the waveguide immersion depth must be such that the maximum volume of melt can be treated without the reservoir bottom destruction, for example, casting ladle fettling. Therefore, in the real technological process of EHPT of melts, the waveguide immersion depth is, as a rule, selected equal to 1/3 the height of the liquid metal. The metal-science studies confirm that, in this case, the aftereffect on the cast structure and the mechanical properties of the cast products is the best.

The present studies have shown that, at the waveguide immersion depth less than 1/3 of the height of the liquid column, the effect of intense wave formation on its surface is observed. A crater in the sand practically does not appear, although there is observed unstable gas removal from the remaining motionless fireclay pieces strictly under the waveguide face–end. Active influence on the chamber bottom begins at the waveguide immersion depth equal to 1/3 of the liquid column. At immersion at a depth of 1/2 or more, after several pulses, the sand exhibits oscillation forms characteristic of oscillations of plates; this counts in favor of intense influence on the bottom. Thus, the efficiency of the waveguide immersion precisely at a depth of 1/3 of the height of the liquid column in the reservoir is confirmed.

Table 3. Parameters of the complex treatment MHDT + EHPT

Varied parameter	Experiment number			
	1	2	3	4
G, l/s	0.068–0.21	0.17	0.17	0.17
f, Hz	1.5	1.5–8	1.5	1.5
W_0, kJ	1.1	1.1	0.6–1.6	1.6
Complex treatment scheme	A	A	A	A, B, C

SECOND STAGE EXPERMENTAL RESULTS AND DISCUSSION

At the second stage, the complex MHD + EHP treatment of the melt was simulated. The experimental stand consisted of a laboratory installation for EHPT and a model of the MHD facility that provided complete geometrical and kinematic similarity to real conditions. The stand also contained a system regulating the supply, circulation, and discharge of the liquid, as well as lighting and registering equipment. A waveguide with a diameter of 20 mm with an attachment was applied. There were used three of nine complex treatment schemes studied earlier in work [3] (Fig. 4), which provided significantly different changes of the structure and properties of the cast metal. The rate of the liquid circulation in the model MHD facility G, the stored energy W_0, and the frequency of the pulse repetition f were varied (Table 3). If it was necessary, for better visualization of the processes proceeding during the treatment, colored liquid was used.

One can estimate the processes taking place in the liquid at the complex treatment according to scheme A (MHD charging + EHPT) from Fig. 5a. At EHPT in the model MHD facility, according to this scheme, after each pulse, there appears a cloud of cavitation bubbles below and above the waveguide attachments. The greatest cloud (~40 cm^3) is formed under the waveguide face–end. The appearing bubbles are removed by the flow upwards from the channel. On the face–end of the waveguide with an attachment, along the waveguide, in the region of the walls of the

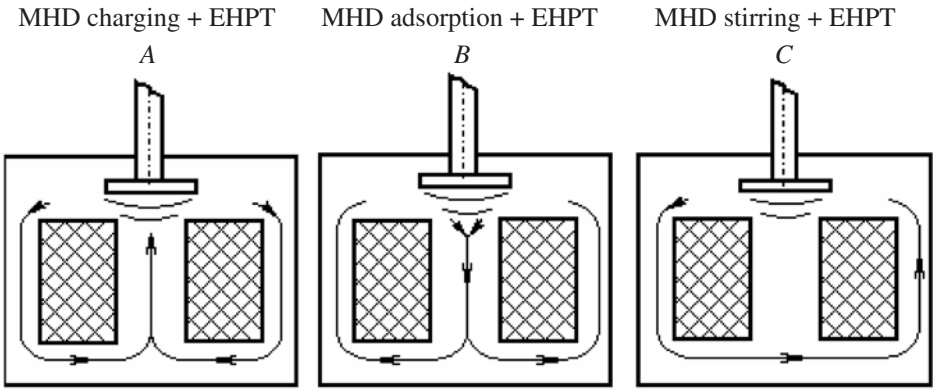

Fig. 4. Schemes of the complex melt treatment (the arrows show the liquid motion direction).

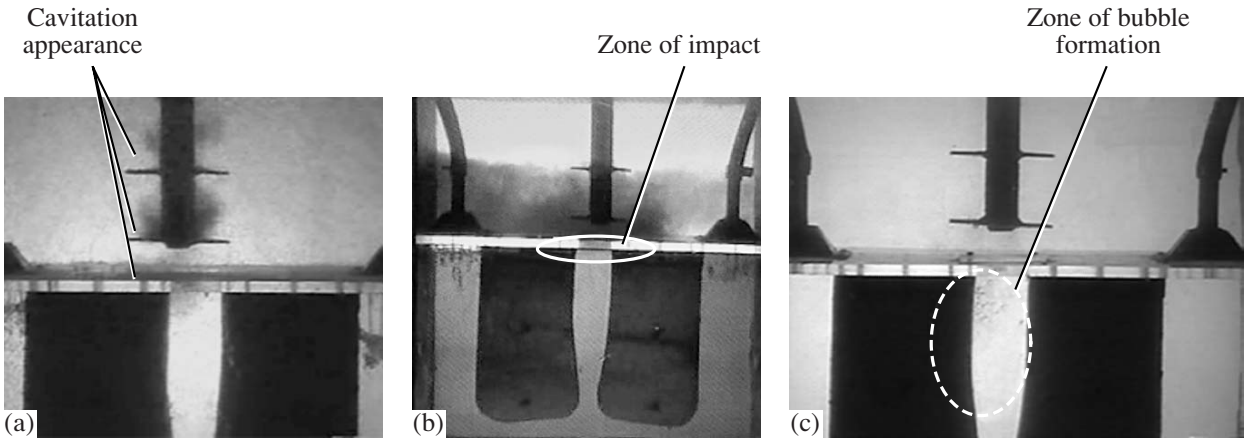

Fig. 5. Complex treatment (MHDT + EHPT) of the model liquid.

MHD-facility central channel, after each pulse, liquid vortexes appear. It is possible they are a manifestation of interaction of the hydrodynamic flows in the MHD facility with convective flows caused by the pulse action of EHPT. As the time of the circulation increases from 0.068 to 0.21 l/s, the bubbles are removed from the MHD-facility central channel more rapidly, liquid vortexes appear irrespective of the values of G, and the cavitation bubble zone volume somewhat decreases (Fig. 6a).

As the frequency f increases from 1.5 to 8 Hz, the bubble sizes decrease; however, the cavitation bubble zone volume does not depend on f (Fig. 6b).

As the pulse energy W_0 increases, the volume of the cavitation bubble appearance zone increases in proportion ($\sqrt{W_0}$) (Fig. 6c). Coloring of the liquid has shown that, when the front of the colored liquid approaches the waveguide face–end, a dark zone appears under it (Fig. 5b). It is possible that it is due to the coloring matter concentration increasing or due to the presence of an optical effect (vortex, high pressure zone). In the course of time, the liquid color in the chamber levels; in the zone under the waveguide face–end, after each pulse, the water darkens for a short time only. The stirring time for the water at EHPT in the model MHD facility was 7 s. Taking into account the similarity scales, one can calculate that the aluminum melt of the same amount shifts for 17 s and the iron–carbon melt, for 49 s.

At treatment according to scheme B (MHD absorption + EHPT), after each pulse, there take place intense gas evolution and formation of a considerable quantity of bubbles, including those of great diameter (up to 5 mm). The basic quantity of bubbles is in the central channel of the MHD facility (Fig. 5c). However, their upfloat is not observed, because, for this, the gas bubble must move against the hydrodynamic flow. Thus, the conditions of gas removal from the treated liquid are not established. As the frequency increases, the hydrodynamic picture varies only slightly in the qualitative aspect, but a pronounced vibration of the central channel occurs.

At treatment according to scheme C (MHD stirring + EHPT), after each feed pulse, there appears a

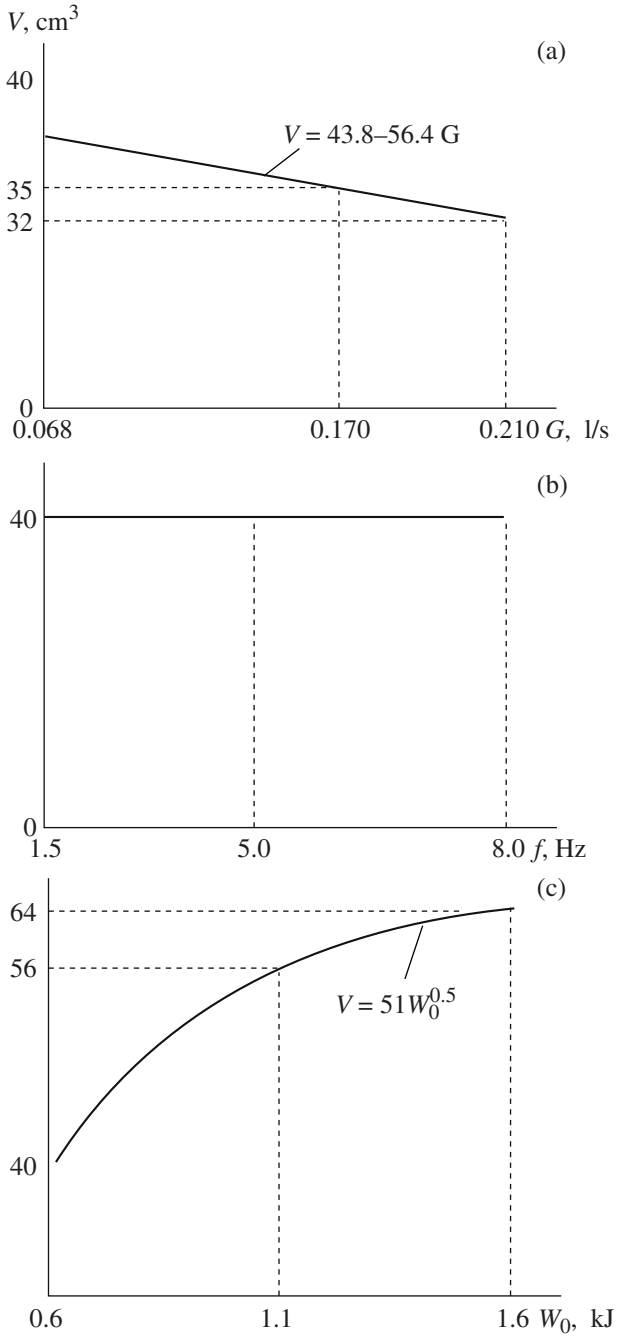

Fig. 6. Dependence of the cavitation zone volume: (a) on the circulation rate; (b) on the frequency of the pulse repetition; (c) on the stored energy of a single pulse (scheme A).

cloud of cavitation bubbles below and above the waveguide attachments; the greatest cloud is formed under the waveguide face–end. A part of the formed bubbles gets into the central channel or appears in it, but immediately floats up and is removed by the flow in the liquid circulation direction. Each pulse causes vortexes in the water under the waveguide face–end and in the central channel. When the frequency is increased from 1.5 to 8 Hz, the picture does not qualitatively change, only the intensity of the formation of the cavitation bubbles increases.

Thus, a comparison of the results for schemes A, B, and C shows that the circulation direction significantly influences the processes, thus leading to changes of the structure and the properties of the liquid. Treatment according to scheme A results in formation of smaller bubbles compared with schemes B and C. The probability of collapse for small bubbles is much higher than for large ones. Therefore, during treatment according to this scheme, it is possible to realize an intense process of bubble collapse with generation in the nearest melt of a high-pressure microzone. As is mentioned in [4], this favors local overcooling of the melt; additional nucleation at crystallization; and, finally, to the cast structure reduction. Treatment according to schemes B and C allows bubble "inflating" with gas up to greater sizes. Hence, here, the gas removal effect is more probable, as well as the obtaining of cast products of higher density. Results of the metal science studies confirm this [3, 7]. In order to allow gas bubbles to float up to the melt surface at treatment according to scheme B, the mode of periodic switching on of the MHD facility may be additionally applied.

CONCLUSIONS

It is impossible to obtain complete similarity of the processes up to their identity at simulation of the complex EHP + MHD treatment of metal melts using water or another model medium due to the variety of the latter and their different nature.

At the same time, it is possible to provide partial satisfaction of the set of basic similarity criteria; this allows describing scenarios of proceeding of the processes in nature according to the data of model studies with accuracy up to their analogy.

One can qualitatively estimate the processes talking place at EHPT: formation of a cavitation cloud, its shift from the waveguide face–end to the reservoir bottom with a rate of about 0.25 m/s, and the appearance of nonstationary hydrodynamic flows (the rate is about 0.05 m/s) in the treated volume.

The optimum ratio of the diameters of the attachment and the waveguide is determined to be ~2.5.

The efficiency of the waveguide immersion at a depth of 1/3 the height of the liquid column at EHPT is confirmed.

There are determined dependences of the volume of the cavitation zones appearing at complex MHD and EHP treatment on the technological parameters of the treatment: the liquid circulation rate, stored energy, and frequency of the pulse repetition at EHPT.

The most effective schemes of the complex EHP + MHD treatment (the schemes "MHD charging + EHPT" and "MHD stirring + EHPT") providing the maximum degree of gas removal from the model liquid are determined; this, together with the metal-science

results obtained earlier, gives the possibility to recommend these schemes for further practical application.

REFERENCES

1. Naidek, V.L., Processes of Out–Of–Aggregate Treatment of Metal Melts of Mass Consumption, in *Suchasne materialoznavstvo XXI storichchya*: Sb. Nauch. Tr., Kiev, 1998, pp. 133–135.
2. Dubodelov, V.I., Seredenko, V.A., Fikssen, V.N., Slazhnev, N.A., Tsurkin, V.N., Grabovyi, V.M., and Kreptyuk, Ya.V., Estimation of Technological Efficiency of Modes of Complex Magnetodynamic and Electrohydropulse Treatment of Aluminum Alloys, *Protsessy Lit'ya*, 2006, no. 3, pp. 81–86.
3. Dubodelov, V.I., Tsurkin, V.N., Grabovyi, V.M., Seredenko, V.A., Fikssen, V.N., Gumenenko, N.K., Slazhnev, N.A., and Kreptyuk, Ya.V., Multifunctional Technological Module as a Tool for Increasing Quality of Cast Products, *Liteinoe Proizvod*., 2006, no. 6, pp. 33–36.
4. Tsurkin, V.N., Grabovyi, V.M., and Sinchuk, A.V., Functional Capabilities of Electrohydropulse Treatment of Melt in a Ladle, *Elektron. Obrab. Mater.*, 2006, no. 5, pp. 55–61.
5. Tsurkin, V.N., Sinchuk, A.V., Kreptyuk, Ya.V., and Degtev, Yu.N., Study of Cavitational Perturbations in Liquid Metal Subjected to Electrohydropulse Treatment, *Protsessy Lit'ya*, 2007, no. 4, pp. 9–15.
6. Tsurkin, V.N., Volkov, G.V., and Sinchuk, A.V., Vpliv elektrogidroimpul'snoi obrobki rozplavu na elementy riznykh strukturnykh rivniv v metali, *Metaloznavstvo ta Obrobka Metaliv*, 2004, no. 4, pp. 37–43.
7. Dubodelov, V.I., Grabovyi, V.M., Seredenko, V.A., Fikssen, V.N., Tsurkin, V.N., and Volkov, G.V., Technological Capabilities of Out–Of–Furnace Complex Magnetohydrodynamic and Electrohydropulse Treatment of Melt, *Protsessy Lit'ya*, 2005, no. 3, pp. 10–16.
8. Voitkunskii, Ya.I., Fadeev, Yu.I., and Fedyaevskii, K.K., *Gidromekhanika*. Uchebnik (Hydromechanics. Handbook), Leningrad, 1982.
9. Dubodelov, V.I., Grabovyi, V.M., Gumenenko, N.K., Seredenko, V.A., Fikssen, V.N., Tsurkin, V.N., Kreptyuk, Ya.V., and Slazhnev, N.A., Ukraine Patent 20685, MPK B22D 27/08, Byull., 2007, no. 2.
10. Landau, L.D. and Lifshits, E.M., *Teoreticheskaya fizika. Uchebnoe posobie v 10 tomakh* (Theoretical Physics. Handbook in Ten Volumes), vol. 6: *Gidrodinamika* (Hydrodynamics), third edition, revised, Moscow, 1986.
11. *Tablitsy fizicheskikh velichin. Spravochnik* (Tables of Physical Quantities. Handbook), Kikoin, I.K., Ed., Moscow: Atomizdat, 1976.
12. *Fizicheskaya entsiklopediya* (Physical Encyclopaedia), Moscow, 1988, vol. 1.
13. *Fizicheskii entsiklopedicheskii slovar*' (Physical Encyclopaedic Dictionary), Moscow, 1960, vols. 1, 3.
14. Ul'trazvuk. *Malen'kaya entsiklopediya* (Ultrasound. Small Encyclopaedia), Moscow, 1979.

ISSN 1068-3755, Surface Engineering and Applied Electrochemistry, 2008, Vol. 44, No. 2, pp. 123–126. © Allerton Press, Inc., 2008.
Original Russian Text © F.P. Grossu, P.N. Pasha, M.K. Bologa, 2008, published in Elektronnaya Obrabotka Materialov, 2008, No. 2, pp. 55–59.

ELECTRICAL PROCESSES IN ENGINEERING AND CHEMISTRY

Hydroelectromagnetic Phenomenain Solutions

F. P. Grossu[a], P. N. Pasha[a], and M. K. Bologa[b]

[a]*State Agrarian University of Moldova, ul. Mirchesht' 44, Chisinau, MD-2049 Moldova*

[b]*Institute of Applied Physics, Academy of Sciences of Moldova, ul. Akademiei 5, Chisinau, MD-2028 Moldova*

E-mail: mbologa@phys.asm.md

Received November 5, 2007

Abstract—Macroscopic motion of weakly conducting liquids under the joint influence of hydrodynamic, electric, and magnetic fields is considered. Physical peculiarities and mechanisms of the occurring of hydroelectromagnetic convection, as well as its applications, are discussed.

DOI: 10.3103/S1068375508020087

INTRODUCTION

The scientific interest in the problem of the electric and magnetic field energies direct application in various branches of industry and science has significantly increased over the past few years. Magnetic and electric impacts on homo- and heterogeneous media have been successfully used for the purposes of energy transformation [1,2], as well as for biological and physiological [3] process control in a number of electric technologies [4]. In order to attain a more efficient utilization of electromagnetic fields, it appears essential to thoroughly and profoundly study the processes of their interaction with substances. In this respect, significant progress has been achieved both in the physics of solid state and magnetic hydrodynamics (MHD), which study the interaction between exterior magnetic fields and conducting liquid media (liquid metals, plasma). Another progressing direction is electric hydrodynamics (EHD), the subject matter of which is the processes involving an electric field impact on the hydromechanic state of liquids and gases. The most advanced progress has been reached in the field of liquid dielectrics [2, 4–8].

An inherent part of magneto- and, particularly, electrohydrodynamics is the subregion of convectional phenomena, whose essential physical characteristic is the spontaneous motion of liquid media caused by the impact of the fields being considered. Magnetic convection can be observed in the so-called ferromagnetic liquids [9] artificially obtained in laboratory conditions and in suspensions of ferromagnetic powders produced on the basis of liquid dielectric carriers (kerosene, transformer oil, etc).

The current urgency of ferrohydrodynamics [9] is justified by such variants of its possible utilization as magnetic suspenders, modulators of various types, gyroscopes, automatic electrical switches, medical diagnostics, heat and mass transfer augmentation, energy transformation, etc. [10].

Electroconvection phenomena (electric convection) are of no less interest. Particularly, the possibilities of their application in performing mechanical [2] and heat energy transformation [11] into the electric one are regarded. There have been created the theoretical and experimental bases for using electric fields in the process of augmentation of heat mass exchange in liquids and gases [5].

The investigations of an electric field influence upon liquid media are undoubtedly considered to be of great importance from the educational viewpoint, especially for revealing physical and chemical properties of liquids [12] with regard to the hydrological phenomena [13].

At the same time, the indicated regions (MHD and EHD) should be viewed just as separate limiting cases of electromagnetic hydrodynamics (EMHD). The wide region which still remains in the shadow is the field of "intermediate" (with respect to their electrophysical parameters) semiconductor media. The matter concerns water solutions of salts and electrolyte solutions, suspensions obtained on the basis of conductive or semiconductive solid particles [14], etc.

The joint influence of electric and magnetic fields on the mechanical properties of liquids has been examined insufficiently. Here, new perspectives are to be revealed in the field of utilization of hydroelectromagnetic (HEM) phenomena occurring under the above influence.

The purpose of the present paper is to briefly present certain issues concerning the joint impact produced by crossed electric and magnetic fields upon the hydromechanics of weakly conducting liquids (solutions) with regard to utilization of the electromagnetic convection and revelation of its physical mechanism.

1. On the prospects of application of crossed electric and magnetic fields in hydromechanics and on certain aspects of hydroelectromagnetic phenomena. Some impacts of crossed electric and magnetic fields on hydrodynamics of solutions as applied to convection heat exchange have been studied by the authors of [14]. Paper [15] presents the methods of application of crossed fields for disengagement of charge carriers in plasma and obtaining electric energy. Attempts have been made to use similar methods for water desalination [16]. Studies of crossed electric and magnetic fields' interaction with plasma have been taken into consideration, particularly, concerning the problems of solar-terrestrial physics [17].

In spite of the comparatively great number of papers devoted to the impact of crossed magnetic and electric fields upon various processes, many aspects of the given problem either are not studied at all or insufficiently represented in the literature. First of all, this concerns the alternating in time fields, as well as the fields of different configuration. The physical mechanism of convection phenomena caused by crossed external fields is not yet entirely comprehended. Actually, the problems of equilibrium stability and the peculiarities of convection in liquids at the presence of such fields are not studied. Moreover, as one can see, the study of the electric and magnetic field influence, including crossed fields influence, on the processes of crystallization has been presented. However, there has not been raised a question yet about the role of some hydroelectromagnetic phenomena occurring in these processes. The same can be said of the impact of the above fields on biological objects, since the tissues of living organisms comprise liquid, which is a solution of various substances (from the viewpoint of our interest, it is worth noting that this liquid can come into hydrodynamic interaction with external fields). Taking into account certain general structural properties of plasma and strong solutions, we should also mention that the study of the electromagnetic field influence on solutions may be of significance for some plasma aspects in physics as well.

All these and the above-mentioned problem of water desalination, which still remains to be solved, along with scale formation control and phase disengagement processes (and the opposite processes of mixing the latter), require a more profound scientific approach. In these directions, the application of crossed electric and magnetic fields seems to be the most promising. In addition, once again, there arises the issue of the hydroelecromagnetic phenomenon impact upon the above processes. In order to study this phenomenon, it is necessary to create a classification of the reasons for its occurrence. The construction of such a classification requires further examination and revelation of a certain physical mechanism, the basis of which is provided by the driving forces of hydroelectromagnetic convection.

2. Electromagnetic forces affecting liquid (nonmetallic) mediums. The issue of forces, called ponderomotive, is considered to be major in the hydromechanics of liquids in external electromagnetic fields (EMF). When determining their value, it is possible, in principle, to be based on the forces which affect separate particles of a substance, summarizing them in a proper way. The event of a separate particle's motion in electromagnetic fields is rather complicated in itself and lacks a solution for a random case. Thereupon, a thermodynamic approach appears to be by far more effective for the forces evaluation. In the case of not too high-speed alternating EMF ($\nu < 10^8$ Hz), the general force affecting a volume unit of a liquid medium comprises two components (SI) [18] :

the magnetic

$$\vec{f}_{\mathrm{m}} = \vec{j} \times \vec{B} - \frac{1}{2}H^2\nabla\mu + \frac{1}{2}\nabla\left[H^2\gamma\left(\frac{\partial\mu}{\partial\gamma}\right)_T\right] + (\varepsilon_r\mu_r - 1)\frac{\partial}{\partial t}\left[\frac{\vec{E}\times\vec{B}}{c^2}\right] \quad (1)$$

and the electric

$$\vec{f}_c = \rho\vec{E} - \frac{1}{2}E^2\nabla\varepsilon + \frac{1}{2}\nabla\left[E^2\gamma\left(\frac{\partial\varepsilon}{\partial\gamma}\right)_\tau\right], \quad (2)$$

where ε, μ, ε_r, μ_r is the absolute and relative dielectric and the magnetic permeabilities, correspondingly; γ – the medium density; and the rest of the symbols are common. The resulting force is determined by the sum of (1) and (2): $\vec{f} = \vec{f}_m + \vec{f}_e$. At the same time, one should distinguish between both intergenerated electromagnetic fields and independent electric and magnetic ones created by the independent external sources.

The latter implies EMF.

The first summands in (1) and (2) represent the forces affecting a volume unit with $\vec{j}$ current density and ρ charge density by the magnetic and electric fields, respectively. The second ones are forces specified by the media heterogeneity on μ and ε (forces that influence the "bound," "magnetic," and electric charges). The third group of terms are magneto- and electrostrictive forces, which fail to participate directly in convection phenomena of closed regions due to their potentiality [5]. The final term in (1) is connected with the fact that, in the process of the thermodynamic derivation of the first three, the impulse of the field itself should be considered. In order to determine the force that solely affects the substance, it is necessary to subtract the force connected with impulse current of the field itself (Abrahaams's force). Whence the given summand, generally called Abrahaams's force, occurs. This force is small as a rule and is generally neglected. However, we shall keep it at the start for the estimation purposes. Henceforth, in (1) and (2), one can neglect

the second and the third summands on the right, since we are to regard, firstly, the nonmagnetic liquids ($\mu = \mu_0 = \text{const}$) and, secondly, the isothermal conditions when there is no reason to expect a gradient of the dielectric permeability. Thus, we are to estimate the function of separate components for the force in the following expression:

$$\vec{f} = \vec{j} \times \vec{B} + \rho\vec{E} + (\varepsilon_r\mu_r - 1)\frac{\partial}{\partial t}\left(\frac{\vec{E} \times \vec{H}}{c^2}\right). \qquad (3)$$

The estimates show that consideration of Abrahaams's force is necessary at frequencies of 10^5 Hz of the external field and intensities of the external electric and magnetic fields ~1 kV/cm and H-10^2 E, correspondingly. In this respect, it is necessary to note that the effects generated by Abrahaams's force present physical interest and are worth investigating. It would seem that the Coulomb force ρE does not have any significant meaning for solutions due to the limitation of the possible intensity magnitudes of the electric field in solutions with a comparatively high specific conductivity (as compared to liquid dielectrics). However, one should bear in mind that the densities of the volume charges ρ may turn out to be high due to the electric concentrational effects [19]. However, in general, the $\rho\vec{E}$ force can be indirectly estimated with respect to the density of the conduction current $\vec{j}_n = \sigma E$ and the mobility of the k ions giving rise to this current according to formula

$$\rho\vec{E} \sim \vec{j}/k = (\sigma/k)\vec{E}. \qquad (4)$$

The numerical estimates show that this force can play a significant part in hydroelectromagnetic phenomena as well.

Let us now discuss the first term of formula (3), where $\vec{j}$ is the total current density, which, in the general case, can be determined by expression [20]:

$$\vec{j} = \sigma\vec{E} + \rho\vec{V} + \frac{\partial(\varepsilon\vec{E})}{\partial t} + D^-\nabla\rho^- - D^+\nabla\rho^+ + \nabla \times (\vec{P} \times \vec{V}), \qquad (5)$$

where $D^{\pm}$ are diffusion coefficients of charge carriers with densities $\rho^{\pm}$, $\vec{V}$ is the hydrodynamic velocity, and $\vec{P}$ is the medium polarization vector. The first summand in (5) is a usual ohmic current; the second, a convection current; the third, a bias current; and the following two terms are diffusion currents of negative and positive ions. The final summand is a bias vortical convection current [20].

It is obvious that the current density in (5), in the general case, can give rise to six additional "lorentz" forces, the estimation of which is connected first of all with the estimation of separate summands in (5) and is a subject for further investigations; here, each term of expression (5) may turn out to be of importance, but, in the first place, it is certainly a through conductivity current, since, on the threshold of the convection phenomenon occurrence, the contribution of other currents (convection ones, in particular) is negligibly small. When considering the presence of alternating currents in further investigations, due attention should be devoted to bias currents as well, the relation of which to the convection currents is as follows:

$$j_b/j_{con} \sim \tau/t_0 = \tau\nu, \qquad (6)$$

where $\nu = 1/t_0$ is the frequency of the applied voltage, and $\tau = \varepsilon/\sigma$ is the time of the electric relaxation. At frequencies of $\geq 10^5$ Hz, the bias currents can essentially correct the total current.

The authors aimed to present general characteristics of the forces that can cause hydroelectromagnetic phenomena. However, this subject is actually infinite in its physical essence. In alternating electric and magnetic fields, there arise certain factors that can have a significant (if not crucial) meaning in convection. They include, firstly, the change of the dielectric permeability with the frequency and, secondly, structural changes of the kind of "the ionic fur coat shaking up" and the resonance phenomena correlated with it.

Thus, from the theoretical point of view, we shall have to solve a whole complex of intricate and fascinating physical problems, the solution of which will promote successful application of hydroelectromagnetic phenomena.

3. Some preliminary experimental data on convection caused by crossed electric and magnetic fields. It is generally known that, at current power on the order of dozens of miliamperes per square centimeter and a magnetic field intensity on the order of hundreds of oersted, there can hardly be observed any convection phenomena. Indeed, as tests prove, no hydrodynamic effects were observed after the electric and magnetic fields of the given parameters and constant in time had been applied. Alternating fields gave no rise to any formidable effect.

Later on, a more thorough series of experiments were carried out with the physical characteristics range of the fields being expanded. The experimental device was a kind of a cell ($80 \times 50 \times 10$ mm) filled with a table salt solution containing additives to ensure the liquid motion visualization. An alternating magnetic field was used (at first, using the mains frequency) obtained in the gap of an 800 Hz laboratory transformer. The direction of the constant electric field (of current) was perpendicular relative to the magnetic one. It was determined that the peak values of the currents (up to electrolysis) and of the voltages generated no well-ordered motions in the liquid.

Certain physical speculations on the charged particle motion in alternating electrical and magnetic fields supported by theoretical calculations brought the idea of the fields synchronizing, i.e., phase coincidence. For this purpose, a matching electric circuit was constructed and experimentally selected. As a result, there were registered well-ordered and rather intensive stream flows of a cellular structure. Two characteristics of the given motion should be noted: (1) the stability of the motions at arbitrarily large (up to extreme) values of the field voltage and (2) the abrupt change of the liquid motion direction at the current reversal. These phenomena have not yet found their quantitative explanation. We failed to reveal a description of similar effects in the existing publications as well.

At the same time, effect (2) indicates that the motion the force of the electromagnetic convection is represented by the first summand (1): $\vec{j} \times \vec{B} = \sigma \vec{E} \times \vec{B}$. Effect number one displays strong stability of the given flow, which resembles, in this sense, the Couette rotation of liquid between two coaxial cylinders rotating in the same direction at a greater angle velocity of the exterior cylinder as compared to the interior one [21].

From the practical point of view, it is worthwhile to note the significance of construction of one-dimensional flows (pumps) and the study of the motion affect upon heat mass transfer. It is not improbable that the liquid becomes non-Newtonian and the fields "wash away" the boundary layers, which may result in considerable intensification of transference processes. The knowledge of the volume concentration distribution of salts is also important for revealing the role of hydroelectromagnetic phenomena in phase disengagement.

CONCLUSION

1. A brief review of scientific data on the interaction processes of electromagnetic fields and liquids is presented.

2. Physical aspects of hydroelectromagnetic phenomena and their driving forces are discussed.

3. Preliminary experimental data revealing physical peculiarities of hydroelectromagnetic phenomena and their various applications are discussed.

REFERENCES

1. *Magnito-Hydrodynamic Energy Transformation. Open cycle.* / Edited by Shumyatskii, B. Ya. and Petrik, M., Moscow: Nauka, 1979.
2. Rubashov, I.B. and Bortnikov, Yu.S., *Elektrogazdinamika* (Electrogasdynamics), Moscow, 1971.
3. Chugaevskii, Yu.V. and Fedorenko, N.E., *Stress i impul'snaya radiatsiya // Stress i adaptatsiya* (Stress and Pulse Radiation) (Stress and Adaptation), Chisinau: Shtiintsa, 1978.
4. Tenesesku, F., Bologa, M., and Kramaryuk, R., *Electrotehnologii*. (Electrotechnologies), Editura Academiei Romane, Bucuresti, 1999.
5. Bologa, M.K., Grosu. F.P., and Kozhukhar', I.A. *Elektrokonvektsiya i teploobmen* (Electroconvection and Heat Exchange), Chisinau, 1977.
6. Ostroumov, G.A., *Vzaimodeistvie elektricheskikh i gidrodenamicheskikh polei* (Interaction of Electric and Hydrodynamic Fields), Moscow: Nauka, 1979.
7. Stishkov, Yu. K. and Ostapenko, A. A., *Elektrogidrodinamicheskie techeniya v zhidkikh dielektrikakh* (Electric Hydrodynamic Flows in Liquid Dielectrics). Leningrad: LGU, 1989.
8. Zhakin, A.L., *Electrohydrodynamics*, Kursk: University Press, 1996.
9. Fertman, V. E., *Magnitnye zhydkosti - estestvennaya konvektsiya i teploobmen* (Magnetic Liquids as Natural Convection and Heat Exchange), Minsk: Nauka i Tekhnika, 1978.
10. Materialy 8-go rizhskogo soveshchaniya po magnitnoi gidrodinamike (Proc. 8th Riga Conf. on Magnetic Hydrodynamics), vol. 1-3, Riga, 1975.
11. Grossu, F.P. and Bologa, M. K., Odnomernye termoelektrodinamicheskie techeniya. *Magnitnaya gidrodinamika*. (One-Dimensional Thermoelectrodynamic Flows. Magnetic Hydrodynamics.), 1974, no. 1.
12. Shul'man, Z.P. et al., Elektroreologicheskii effect (Electroreological Effect), Minsk: Nauka i Tekhnika, 1972.
13. Bondarenko, N.F. and Gak, E.Z., *Elektromagnitnaya gidrofizika i prirodnye yavleniya* (Electromagnetic Hydrophysics and Natural Phenomena), vol. 1, 2, 1994, 1995.
14. Bulum, E.Ya. et al., *Teplo- i massoobmen v elektromagnitnom pole* (Heat- Mass Exchange in the Electromagnetic Field), Riga, 1967.
15. Zisman, A.B., USSR, Inventor's Certificate CO2 v L/00, B03 C1/08, no. 36, 1981.
16. Slesarenko, V.N., *Sovremennye metody opresneniya morskikh i solenykh vod* (Modern Methods of Sea and Salt Water Desalination), Moscow: Energiya, 1973.
17. Akasofu, S.M. and Chepmen, S., *Solnechno-zemnaya fizika* (Solar- Terrestrial Physics), vol. 2, 1975.
18. Landau, M.D. and Lifshits, E.M., *Elektrodinamika sploshnykh sred* (Electrodynamics of Continuums), Moscow: Nauka, 1957.
19. Ostroumov, G. A., *Elektrokhimiya* , vol. 2, no. 3, 1968.
20. Panovskii, V. and Filips, M., *Klassicheskaya elektrodinamika* (Classic Electridynamics), Moscow: Fizmatgiz, 1963.
21. Landau, M.D. and Lifshits, E.M., *Gidrodinamika* (Hydrodynamics), Moscow: Nauka, 1986.

ISSN 1068-3755, Surface Engineering and Applied Electrochemistry, 2008, Vol. 44, No. 2, pp. 127–132. © Allerton Press, Inc., 2008.
Original Russian Text © E.V. Kuvaldina, 2008, published in Elektronnaya Obrabotka Materialov, 2008, No. 2, pp. 60–66.

ELECTRICAL PROCESSES IN ENGINEERING AND CHEMISTRY

Loading Effect at Air Plasma Etching of Fabric of Polyethylene Terephthalate Fibers

E. V. Kuvaldina

Ivanovo State Chemicotechnological University, pr. Engel'sa 7, Ivanovo, 153000 Russia
E-mail: evk@isuct.ru

Received November 27, 2007

Abstract—The results of studying the loading effect at low temperature air plasma action on the surface of fabric of polyethylene terephthalate filament yarns are presented. Gravimetric and mass-spectrum techniques were used in this work. Gas evolution changes plasma properties and, as a consequence, the target process kinetics. Due to the mutual influence of heterogeneous and volumetric processes not only flows of active oxygen particles on the material surface reduce but also the correlations of these flows change. The NO molecule concentration is closely connected with the atom oxygen balance. Even when the fraction of the reactor surface occupied by the fabric is relatively low, the NO molecules' concentration drops appreciably. For a wide interval of discharge parameters, the specific rates of etching, the oxygen absorption from the gas phase, the gaseous product formation, and the NO molecule concentration decrease extensively when the reactor load ratio is increased from 6% to 50%. The interconnected influence of the parameters and the loading is shown in the behavior of the reaction product formation. In the case of the load ratio rising, the correlation of the degradation channels changes to a channel with a yield of CO and H_2 stronger at higher initial gas pressure.

DOI: 10.3103/S1068375508020099

INTRODUCTION

The loading effect at plasmochemical etching is shown in decreasing of the material etching rate with increasing of its amount, starting with a boundary value. The loading effect appearance was initially attributed to decreasing of the number of chemically active particles (CAP) per unit area of the treated surface [1, 2]. It was considered that the CAP formation rate does not vary. Later, the conclusion was made that the loading effect is related to the appearance of gaseous products of heterogeneous reactions and to a change of properties of the plasma bounding surface (boundary conditions for active particles) [3, 4]. As a result, the physical parameters of the plasma, the rates of the active particle generation, and the rate of the target process change. This effect may play the key role at modification of polymer films and fabrics in industrial reactors where plasma is completely bounded by chemically reacting surfaces. The loading effect is poorly known today. The majority of works in this field are concerned with investigation of material etching rates for obtaining of optimum values [5–7]. Data on the change in the rates of formation of gaseous products and their ratios related to the difference in the treated surface area are available only for polyimide film on exposure to oxygen plasma [8].

The aim of the present work is to study the loading effect influence on the kinetics of the stationary process of etching and formation of gaseous products at the air plasma action on the surface of fabric of polyethylene terephthalate (PETP).

EXPERIMENTAL

The experiments were carried out by virtue of the installation whose scheme is shown in work [9]. Plasma was formed by ignition of a direct current discharge in a cylindrical reactor of C-49 glass. The pressure of the plasma-forming gas in the reactor varied from 50 to 200 Pa, and the current intensity varied from 20 to 110 mA. The constant parameters were the following: the linear rate of the gas flow in terms of the standard conditions was 30 cm/s, the sample temperature was 357 K, and the treatment time was 10 min. The subject of the studies was a home lavsan fabric of filament yarns characterized by a mean thickness of 124 μm (specification 81476). The fabric parameters determined by virtue of a scanning electron microscope (Tesla BS-300) were the following: the yarn diameter was 220 μm, the space between the yarns was 20 μm, the mean diameter of the monofilament in the yarn was 18.5 μm, and the specific density was 7.2 mg/cm^2. The fabric samples in the form of a cylinder were placed on the thermostatically controlled reactor wall in the posi-

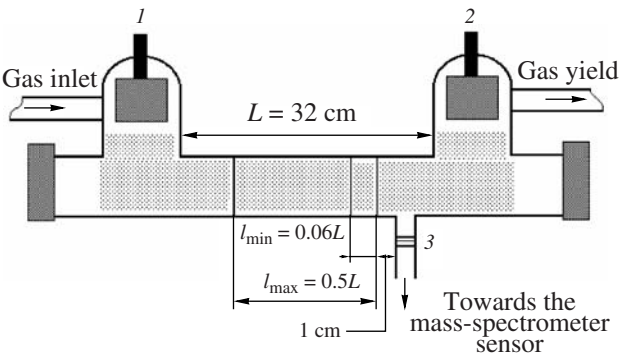

Fig. 1. Fragment of the experimental installation diagram: *1* is the cathode; *2* is the anode; *3* is the diaphragm; and l_{min} and l_{max} are the minimum and maximum dimensions of the sample element, respectively.

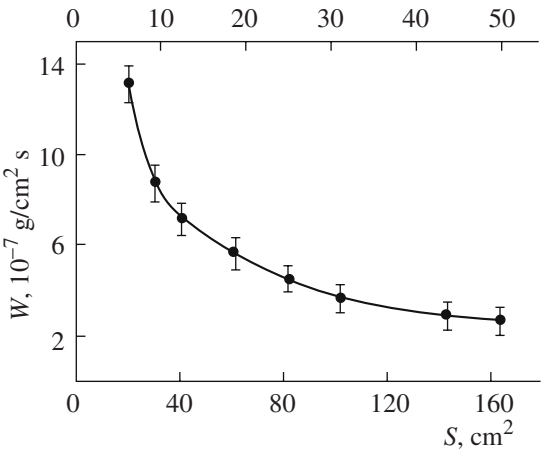

Fig. 2. Rate of loss in weight of the PETP fabric versus the reactor load ratio (%).

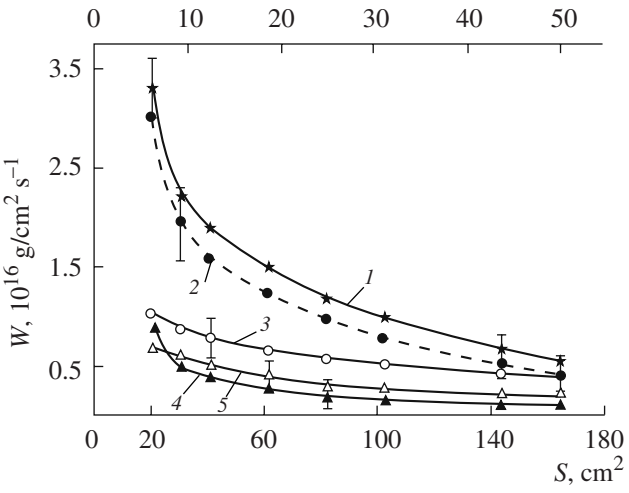

Fig. 3. Rate of consumption of O_2 (*1*) and formation of CO_2 (*2*), CO (*3*), H_2O (*4*), and H_2 (*5*) versus the reactor load ratio (%).

tive column space. The length of the fabric cylinder element was varied within the range of 2–16 cm. The position of one of the sample edges remained invariant, the treated material surface increased from 20.5 to 164 cm^2, and the part of the reactor surface covered with the fabric increased from 6 to 50% (Fig. 1).

The loss in weight of the samples was determined by periodic weighing on analytical scales (WA-34 brand). The weighing accuracy was 1×10^{-4} g. The composition of the gaseous products of the etching, the rate of their formation, and the consumption of the reagents were analyzed by virtue of a mass spectrometer ([Russian] IPDO–2A with a PMO-4C sensor).

RESULTS AND DISCUSSION

According to the results of the mass spectrometric measurements, under all the mentioned conditions, oxygen is consumed; the destruction products are molecules of CO_2, CO, H_2O, and H_2. Nitrogen-containing products of the etching and nitrogen consumption are not noted in the air; the NO molecules are stable products of the discharge burning.

Figure 2 shows, for a pressure of 100 Pa and a discharge current of 80 mA, the mean rates of loss in weight W found as the ratio of the losses in weight of the whole sample to its area, and Fig. 3 shows, under the same conditions, rates of O_2 consumption and formation of gaseous products W_i. Within the reproducibility of the results, the evolution of the products with due account for the oxygen consumed for the material oxidation completely determines the experimentally measured rates of the loss in weight. As the load ratio increases by a factor of 8, the total mole fraction of the products in the gaseous phase increases from 0.21 to 0.31. The specific rates of all the processes decrease (for a loss in weight by approximately a factor of 5) asymptotically approaching their constant values. If the mechanisms of the proceeding processes remain invariant, then the yields of gaseous products per one reacting oxygen molecule must be preserved.

Studies [10–14] have shown that, according to the dependences of the yields of the polymer material etching products on the plasma parameters (the plasma-forming gas: oxygen, air), all of them may be divided into two groups. The first group may include molecules of CO_2 and H_2O, their yields being either constant or linearly increasing. The second group includes molecules of CO and H_2. Their yields do not depend on the discharge current, they linearly decrease as the pressure increases; besides, at the transition into the zone of the afterglow, the yield of H_2 molecules sharply decreases and shows another dependence on the pressure. The channel contribution leading to formation of CO and H_2 increases at the transition from O_2 plasma to air plasma. For the rates of formation of molecules of CO_2; H_2O; and, partially, H_2, a relatively simple linear connection with the rate of formation of O atoms in the plasma

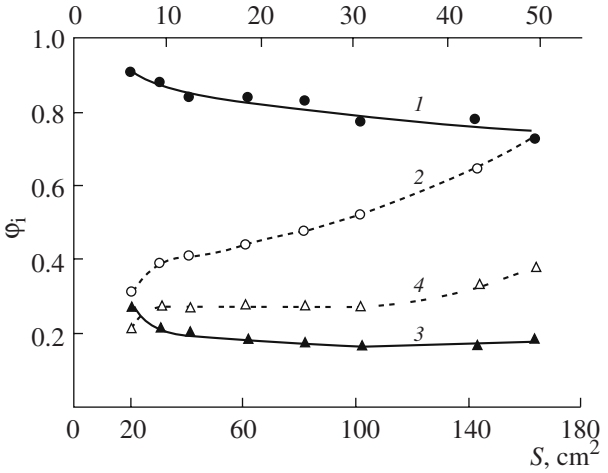

Fig. 4. Yields of CO_2 (*1*), CO (*2*), H_2O (*3*), and H_2 (*4*) per one reacting molecule of oxidant versus the reactor load ratio (%).

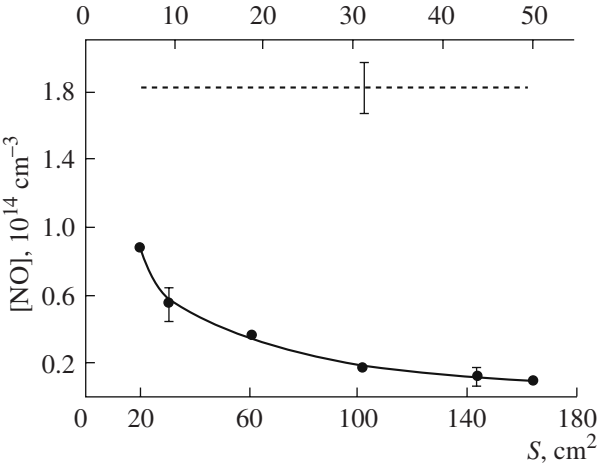

Fig. 5. Concentration of NO molecules in the discharge in the sample absence (*1*) versus the reactor load ratio (*2*) (%).

exists. For CO molecules, no correlation with the rates of formation of the active plasma agents (O atoms, O_2 metastable molecules, ions, and quanta of VUV radiation) has been found. Therefore, a conclusion was made that the observed relationships are connected with peculiarities of the reaction mechanisms in the solid phase. However, the rates of formation and yields of CO and H_2 are inversely and strongly nonlinearly connected with the pressure (the flow on the surface of oxygen molecules in the ground state).

We have calculated yields of gaseous products per one reacting molecule of O_2 ($\varphi_i = W_i/W_{O2}$) and have presented them in Fig. 4. As the treated surface area increases, symbate changes of the product yields take place; the ratio of the material destruction channels varies in favor of the channel with formation of CO and H_2. Besides, the yields of CO and H_2 increase much faster than the yields of CO_2 and H_2O decrease. It is obvious that this redistribution of the channels is a result of a compositional change of the plasma-forming gas. In fact, oxygen is consumed for the reactions and its partial pressure decreases to a considerable extent; at the same time, the initial gas at the material etching is doped with destruction products. According to the results of measurements in the space behind the sample, as the loading increases from 6 to 50%, the ratio of the total partial pressure of the etching products to the partial pressure of the O_2 molecules increases from 3 to 14. Thus, even when the reactor surface part covered with the fabric is relatively small, the PETP fabric etching occurs in a complex multicomponent system. According to the data of calculations carried out for O_2 plasma [15], the appearance of etching products of CO_2, CO, and H_2 in the gaseous phase leads to a decrease of fast electrons in the EEDF and, as a consequence, to a decrease of the constants of the rates of the gaseous threshold processes. The higher the threshold process energy, the greater the decrease degree. In the case of air, the product influence on the discharge properties must be more pronounced. This is confirmed by the results of work [11]. The increase of the rate of loss in weight of the fabric of PETP fibers in air plasma, even at a relatively low load ratio of the reactor (less than 10%), was accompanied by a decrease of the atomic oxygen concentration at the sample temperature increase. In oxygen plasma, under the same conditions, no dependence of the atom concentration, the electric field intensity, and the gas temperature on the material etching rate was observed.

It is possible that there is an additional cause leading to variation in the ratios of the rates of the gaseous product formation. This is dissociation of the reaction products by electron impact, which may be shown at great distances from the sample to the place of sampling. We have checked on this hypothesis by realizing measurements at motions of the sample with a 2-cm element along the positive column. The results have shown that dissociation of the reaction products under these conditions may be neglected.

In the sample presence, the concentration of nitrogen oxide molecules in the discharge decreases greater at a higher load ratio of the reactor (see Fig. 5). When the reactor surface part covered with the fabric is 6%, the concentration of NO molecules decreases by a factor of 2 in comparison with the initial value (in the sample absence) and by a factor of 17 at 50%. Atoms of $O(^3P)$ and vibrationally excited molecules (VEM) of nitrogen play the principal role in the formation of NO molecules [16]. This explains the strong dependence of the nitrogen oxide concentration on the ratio of the reactor loading with the polymer.

The next stage of the work is connected with the study of the loading effect in a wide range of the discharge parameters (pressures and currents). Plasma action was exerted on samples with a width of 2.7 and 16 cm, and the reactor load ratio was 8.5 and 50%,

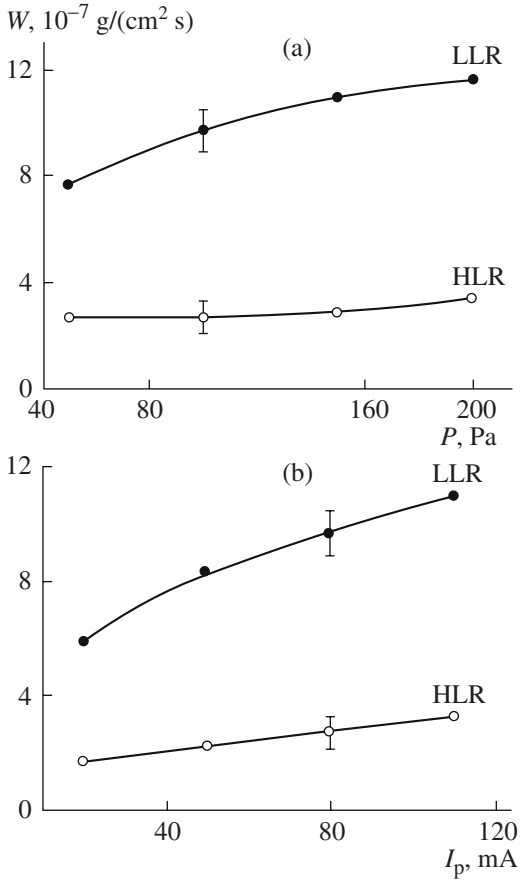

Fig. 6. Rate of loss in weight of the PETP fabric samples versus the pressure of the plasma-forming gas at I_p = 80 mA (a) and versus the discharge current at P = 100 Pa (b).

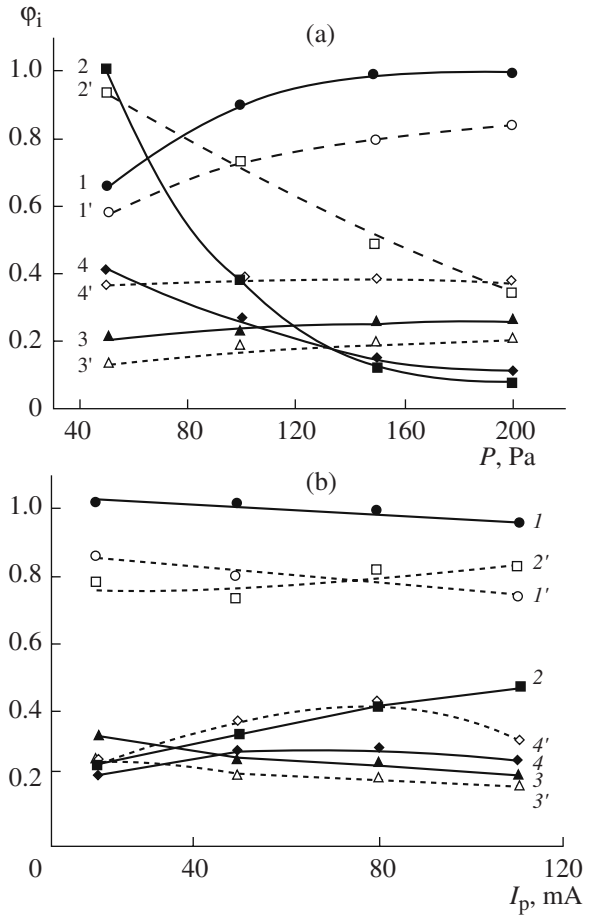

Fig. 7. (a) Yields of CO_2 (*1*, *1*'), CO (*2*, *2*'), H_2O (*3*, *3*'), and H_2 (*4*, *4*') per one reacting molecule of oxidant versus the pressure of the plasma-forming gas at I_p = 80 mA; (*1–4*)—LLR; (*1'–4'*)—HLR. (b) Yields of CO_2 (*1*, *1*'), CO (*2*, *2*'), H_2O (*3*, *3*'), and H_2 (*4*, *4*') per one reacting molecule of oxidant versus the discharge current at P = 100 Pa; (*1–4*)–LLR; (*1'–4'*)–HLR.

respectively. Let us denote them as the low load ratio (LLR) and high load ratio (HLR). The experiment data at all the studied parameters have shown retention of the common effect; that is, as the amount of the treated material increases, the specific rates of the loss in weight, oxygen consumption, and evolution of the gaseous etching products decrease as well as the NO molecule concentration in the discharge.

Figure 6 shows the specific rates of the loss in weight of fabric samples (at LLR and HLR) versus the air pressure at a discharge current of 80 mA and versus the discharge current at a pressure of 100 Pa. Under the same conditions, Figs. 7a and 7b present yields of gaseous reaction products and Fig. 8 shows the NO molecule concentration in the discharge.

The difference in the weight rates due to the loading weakly depends on the discharge parameters. The difference in the concentrations of NO molecules is preserved approximately constant too. Interdependent influence of the parameters and the loading is shown mainly in the behavior of the evolution of the reaction products. We have calculated ratios of the yields of each product at HLR and LLR ($\varphi_i^{HLR}/\varphi_i^{LLR}$).

Oxidation of the polymer surface is obtained at joint action of $O(^3P)$ atoms, $O_2(a^1\Delta_g)$ metastable molecules, and oxygen molecules in the ground state. The presence of oxygen atoms is a necessary condition of plasma etching of materials, i.e., destruction of oxygen-containing groups, leading to formation of gaseous products [17]. If with increasing loading, due to the mutual influence of the heterogeneous and volume processes, both the total flow of oxygen particles and the relative content of atoms in it decrease, then the yields of the destruction gaseous products must decrease. This is what takes place at all the discharge parameters in the case of the channel of destruction with formation of CO_2 and H_2O and at low pressure in the case of the channel of destruction with formation of CO and H_2. As has been mentioned above, the connections between the rates of formation of O atoms and CO_2 and H_2O molecules are linear. Irrespective of the parameters, the ratio of the yields of these products for HLR and LLR holds approximately true (see table).

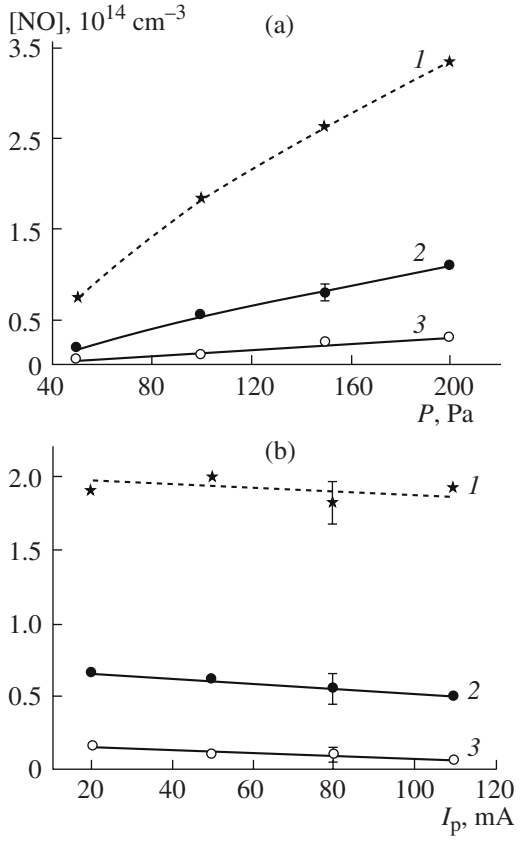

Fig. 8. Concentration of NO molecules in the discharge in the sample absence (*1*), in the fabric sample presence at LLR (*2*), and HLR (*3*) versus the initial gas pressure at $I_p = 80$ mA (a) and versus the discharge current at $P = 100$ Pa (b).

The situation for the channel with yield of CO and H_2 is more complex. As was mentioned above, the mechanism of the reactions of the formation of CO and H_2 is not thoroughly understood. The total of the linear and nonlinear effects resulting from the increase of the content of the reaction products in the gaseous phase, the decrease of the flows of the molecular and activated oxygen to the surface, and the variation in their ratios leads to the fact that the difference in the yields of CO and H_2 connected with the loading increases almost proportionally with the plasma-forming gas pressure. The contribution of this channel inversely and nonlinearly depends on the oxidant pressure. As the load ratio increases for all the conditions, the partial pressure of O_2 molecules in the composition of the plasma-forming gas decreases; this must be accompanied by a nonlinear increase of the yields of CO and H_2. Earlier, we faced the fact that, at a low content of O_2 in the N_2 and O_2 mixture, an additional reagent is water vapor and the main products of the polymer etching are molecules of CO and H_2 [18].

CONCLUSIONS

At plasmochemical etching in air of a fabric of PETP filament yarns, the loading effect is shown in a wide range of the discharge parameters. Gas evolution changes the plasma properties and, as a consequence, the kinetics of the target process. As the loading increases, due to the mutual influence of heterogeneous and volume processes, the flows of oxygen particles to the material surface decrease; besides, their ratio varies. In particular, the relative content of the $O(^3P)$ atoms decreases. The atomic oxygen balance is connected with the concentration of NO molecules in the discharge. Even with a relatively small part of the reactor surface covered with the fabric (6%), the total partial pressure of the reaction products exceeds the partial pressure of O_2 molecules; the concentration of NO molecules in the discharge appreciably decreases; that is, the loading effect takes place. As the treated material

Ratios of the yields of gaseous products at HLR and LLR of the reactor

$I_p = 80$ mA				
P, Pa	$\varphi_{CO_2}^{HLR}/\varphi_{CO_2}^{LLR}$	$\varphi_{CO}^{HLR}/\varphi_{CO}^{LLR}$	$\varphi_{H_2O}^{HLR}/\varphi_{H_2O}^{LLR}$	$\varphi_{H_2}^{HLR}/\varphi_{H_2}^{LLR}$
50	0.87	0.93	0.65	0.90
100	0.82	1.92	0.82	1.46
150	0.81	4.08	0.73	2.75
200	0.84	4.86	0.77	3.36
$P = 100$ Pa				
I_p, mA	$\varphi_{CO_2}^{HLR}/\varphi_{CO_2}^{LLR}$	$\varphi_{CO}^{HLR}/\varphi_{CO}^{LLR}$	$\varphi_{H_2O}^{HLR}/\varphi_{H_2O}^{LLR}$	$\varphi_{H_2}^{HLR}/\varphi_{H_2}^{LLR}$
20	0.84	3.18	0.80	1.16
50	0.79	2.18	0.83	1.27
80	0.82	1.92	0.82	1.46
110	0.78	1.88	0.84	1.22

amount increases, the specific rates of etching, the consumption of oxygen from the gaseous phase, and the formation of gaseous products of the material destruction considerably decrease as well as the concentration of NO molecules in the discharge. The interdependent influence of the parameters and the loading is shown in the behavior of the evolution of the reaction products. As the load ratio increases, the destruction channel ratio varies in favor of the channel with the yield of CO and H_2 being stronger at higher pressure of the initial gas.

REFERENCES

1. Danilin, B.S. and Kireev, V.N., *Primenenie nizkotemperaturnoi plazmy dlya travleniya materialov* (Low Temperature Plasma Application for Etching of Materials), Moscow: Energoatomizdat, 1987.
2. Ivanovskii, G.F. and Petrov, V.I., *Ionno–plazmennaya obrabotka materialov* (Ion–Plasma Treatment of Materials), Moscow: Radio i Svyaz', 1986.
3. Maksimov, A.I., Gorberg, B.L., and Titov, VA., Possibilities and Problems of Plasma Treatment of Fabrics and Polymer Materials, *Tekstil'naya Khim*., 1992, no. 1, pp. 101–117.
4. Maximov, A.I., Rybkin, V.V., Kuvaldina, E.V., and Titov, V.A., Loading Effect as a Result of Feedback in Chemically Reacting Plasma, Proc. 14th Int. Symposium on Plasma Chemistry, Prague, Czech Republic, 1999, vol. II, pp. 753–757.
5. Lamontegne, B., Wrobel, A.M., Jelbert, G., and Wertheimer, M.P., Large–Area Microwave Plasma Etching of Polyimide, J. *Phys. D: Appl. Phys.*, 1987, vol. 20, no. 7, pp. 844–850.
6. Economau, D., Audit, E.S., and Barno, G., In Situ Monitoring of Etching Uniformity in Plasma Reactors, *Solid State Technol*., 1991, vol. 34, no. 4, pp. 107–111.
7. Lerner, N.R. and Wydeven, T., Polymer Etching in the Oxygen Afterglow Increased Etch Rate with Increased Reactor Loading, *J. Electrochem. Soc*., 1989, vol. 136, no. 5, pp. 1426–1430.
8. Maksimov, A.I., Rybkin, V.V., and Kuvaldina, E.V., Influence of Chemically Reacting Boundary Surfaces on Oxidation Destruction of Polyimide in Nonequilibrium Plasma, *Khim. Vys. Energ*., 1995, vol. 29, no. 1, pp. 60–62.
9. Kuvaldina, E.V., Lyubimov, V.K., Maksimov, A.I., and Rybkin, V.V., Investigation of Temperature Dependences of Rates of Polyimide Film Etching in Oxygen Plasma, *Khim. Vys. Energ*., 1990, vol. 24, no. 5, pp. 471–474.
10. Rybkin, V.V., Kuvaldina, E.V., and Titov, V.A., Kinetic Behavior of Etching of Polyethylene Terephthalate and Polyimide in Oxygen Plasma, *Khim. Vys. Energ*., 1998, vol. 32, no. 6, pp. 465–469.
11. Rybkin, V.V., Titov, V.A., Kuvaldina, E.V., and Smirnov, S.A., Comparative Analysis of Etching of Fabric of Polyethylene Terephthalate Fibers in Oxygen and Air Plasma, *Khim. Vys. Energ*., 1997, vol. 31, no. 6, pp. 449–452.
12. Rybkin, V.V., Kuvaldina, E.V., Serova, N.Yu, Smirnov, S.A., and Titov, V.A., Etching of Polyethylene Terephthalate Fabric in Air Plasma Afterglow, *Khim. Vys. Energ*., 1996, vol. 30, no. 3, pp. 219–223.
13. Titov, V.A., Shikova, T.G., Kuvaldina, E.V., and Rybkin, V.V., Kinetic Behavior of Formation of Gaseous Products under Oxygen Plasma Action on Surface of Films of PE, PP, PETP, and PI, *Khim. Vys. Energ*., 2002, vol. 36, no. 5, pp. 391–394.
14. Kuvaldina, E.V., Shutov, D.A., Rybkin, V.V., and Smirnov, S.A., Kinetics of Formation of Gaseous Products under Action of Plasma of Nitrogen–Oxygen Mixtures on Polypropylene Surface, *Khim. Vys. Energ*., 2004, vol. 38, no. 3, pp. 231–233.
15. Bulan'kov, N.I, Kuvaldina, E.V., Lyubimov, V.K., and Rybkin, V.V., Analysis of Applicability of the Method of Small Argon Additives for Optic Diagnostics of Oxygen Plasma Containing Impurities of CO_2, CO, and H_2, Zh. *Prikl. Spektrosk*., 1991, vol. 54, no. 3, pp. 851–854.
16. Rybkin, V.V., Smirnov, S.A., Kuvaldina, E.V., and Titov, V.A., Kinetic Analysis of the Processes of Formation and Destruction of Neutral Particles of Air Plasma, Abstracts of Papers *IX Vserossiiskaya konferentsiya po fizike gazovogo razryada* (IX All–Russia Conf. on Gas Discharge), Ryazan, RGRTA, 1998, part I, pp. 20–21.
17. Shikova, T.G., Rybkin, V.V., Titov, V.A., and Choi, Kh.S., Reactions of Active Particles of Oxygen Plasma with Polyethylene, *Khim. Vys. Energ*., 2006, vol 40, no. 5, pp. 396–400.
18. Kuvaldina, E.V., Shutov, D.A., and Rybkin, V.V., Kinetics of Formation of Gaseous Products under Action of Plasma of Nitrogen–Oxygen Mixtures on Polypropylene Surface, *Khim. Vys. Energ*., 2004, vol. 38, no. 3, pp. 231–233.

ISSN 1068-3755, Surface Engineering and Applied Electrochemistry, 2008, Vol. 44, No. 2, pp. 133–137. © Allerton Press, Inc., 2008.
Original Russian Text © B.B. Kolupaev, 2008, published in Elektronnaya Obrabotka Materialov, 2008, No. 2, pp. 67–72.

ELECTRICAL PROCESSES IN ENGINEERING AND CHEMISTRY

Influence of Surface Layers on the Formation of the Electrophysical Properties of Heterogeneous Polymer Systems

B. B. Kolupaev

Rovno State Humanitarian University, ul. Ostafova 31, Rovno, 33000 Ukraine
E-mail: Boris_Kolupaev@ukr.net

Received October 22, 2007

Abstract—There is investigated the role of polymer layers on the metal surface of a fine filler in the formation of a PVC system with electrophysical properties. It is shown that a physicochemical polymer modification takes place under the surface active center influence. Thus, the surface layer properties (density and geometrical characteristics) differ from the PVC ones. The correlation between the electrophysical properties of the PVC composite and the surface layer in the range of the fine copper fraction of 0–11.3 vol % at $E \le 10^6$ V m^{-1} and a frequency response of 20–2 $\times 10^5$ Hz is determined. An explanation of the investigated relation is presented.

DOI: 10.3103/S1068375508020105

INTRODUCTION

In the case of heterogeneous polymer systems (HPS), it is found [1] that the adsorption interaction with the filler particle surface results in restriction of the possible conformations of the macromolecules providing a change of the relaxation properties of the composite. In the adsorption layer, separate segments of the macromolecules directly interact with the surface, thus forming adsorption sequences [2]. It also contains segment formations in the form of loops and tails that belong to the given molecule but are not adsorption connected to the surface, as well as segments of an adsorbed macromolecular coil that does not directly interact with the surface. Therefore, the adsorption interaction of the polymer molecules with the solid surface of the filler may be considered a process leading to redistribution of intermolecular forces in the surface layer and formation of additional points of the physical structural network due to contacts of the chain segments with the surface. It is characteristic that changes of molecular mobility affect not only the adsorption layers but also the surface ones, since the surface effect is shown clearly far away from the surface [3]. The properties of the polymer layers (PL) formed at the interface with solids are of great practical interest, especially in the case of polymer systems with fine fillers [1]. One can apply to transition layers the notions of effective thickness Δl, density ρ_1, and other properties they are estimated by [3]. However, the issue concerning not only the conditions of PL formation and estimation of their characteristics and structure but also the influence on the complex of HPS properties remains open. Therefore, the aim of the studies is to determine the effective characteristics of PL and their role in the formation of the electrophysical properties of metal-filled flexible-chain polymers. It should be noted that, in amorphous flexible-chain polymers, only fluctuation (not excepting the discreteness of their form) structure elements with finite lifetimes may exist [4]. After the manner of [1], let us call them microblocks (or supernetworks); the lifetime of separate relaxation oscillators is described by the Boltzmann relation [5].

MODEL

Let us suppose, after [3], that HPS is an assembly of particles of fine filler, PL, and polymer with invariable properties. This model approximation of HPS is correct provided that the filler content φ is less than the critical one φ_{cr}, that is, when the whole polymer binder transits into the PL state [4]. After introduction of a certain quantity of filler into the HPS, the density fluctuations in the form of PL appear. All the active centers of the filler surface act as potential field sources, being to some extent equivalent to the external pressure, since interaction at the polymer–filler interphase is realized [4]. Let us suppose that potential forces of interaction of the kinetic elements of the polymer matrix structure and active centers act radially to the filler surface. Then, taking into account the statistical character of the bond distribution, following [5], we write

$$\rho_1 = \rho_0 \exp\left(-\frac{W(l)}{kT}\right), \quad (1)$$

where ρ_0 is the mean value of the polymer matrix density, and $W(l)$ is the value of the work necessary for bringing the polymer structure subsystem to the filler surface active center at the distance l (at $l = \infty$, $W = 0$ and $\rho_1 = \rho_0$). Taking into account that

$$W(l) = W_1(l) - W_2 + W_3(\Delta l), \tag{2}$$

where $W_1(l)$ is the value of the work necessary for the formation of the place of the structure subsystem in the PL, the value of this work at $l = \infty$ corresponds to W_2, and $W_3(\Delta l)$ is the work of the potential forces at the structure subsystem transition from $l = \infty$ to the certain point 0 of the PL. Taking into account the Boltzmann law [5], we obtain

$$\frac{1 - P_1(l)}{1 - P_2(l)} = \exp\left\{-\frac{[W_1(l) - W_2]}{kT}\right\}, \tag{3}$$

where $P_i(l)$ ($i = 1, 2$) is the probability that the center of one of the $(N - 2)$ structure subsystems of the polymer matrix (except for the considered two) lies at the point 0. Using relations (1) and (2), we obtain

$$\rho_1 = \rho_0 \frac{1 - P_1(l)}{1 - P_2(l)} = \exp\left[-\frac{W_3(\Delta l)}{kT}\right], \tag{4}$$

where $P(l)$ is the P value at $l = \infty$.

Proceeding from the fact that the source of the HPS density variation is, in addition to φ, the PL connected to it, without loss of generality, it follows that $P_i \sim \varphi$. In fact, the higher the volume content of fine filler in the polymer system, the higher the probability of the kinetic structure element being at the point 0 of the polymer surface layer. In a first approximation, we consider that $W_2(\infty) = 0$, that is, $P_2(l) = 0$; then,

$$\rho_1 = \rho_0(1 - \varphi)\exp\left[-\frac{W_3(\Delta l)}{kT}\right], \tag{5}$$

where $0 < \varphi \le \varphi_0$, and φ_0 is the limiting volume content of the disperse phase in the HPS (0.74 at regular packing of equidimensional spheres of the disperse filler, 0.63 at the statistical one, and 0.80 in the case of a binary mixture of spheres differing in their dimensions by approximately an order) [3].

If we suppose that, on the filler particle of radius R, a PL appears in the form of a globular layer of the effective thickness Δl and then (at $0 < \varphi \le \varphi_{cr}$) there is a polymer in bulk, then

$$M_s = M_p + N_i \int_R^{R+\Delta l} \rho_0(1 - \varphi) e^{-W_3(\Delta l)/kT} 4\pi R^2 dR + M_f, \tag{6}$$

where M_s, M_p, M_f is the mass of the HPS, of the polymer in bulk, and of the filler, respectively, and N_i is the quantity of the filler particles.

In the range $0 < \varphi \le \varphi_{cr}$, as the filler content in the HPS increases, the value M_p decreases. Let us represent the given dependence in the form of the Langmuir equation [2]

$$dm = \alpha m dn, \tag{7}$$

where α is the coefficient characterizing the filler activity [4]. Taking into account that, at introduction of the filler particles N, the polymer binder mass varies from M_p to the value M_{pl} (M_{pl} is the PL mass), after integration of relation (7), we obtain

$$M_{pl} = M_p[1 - \exp(-\alpha N_i)]. \tag{8}$$

If we suppose that macromolecules in the PL do not participate in the molecular motion process, then their rate v is [3]

$$v = 1 - \frac{\Delta C_1}{\Delta C_2}, \tag{9}$$

where ΔC_1 and ΔC_2 are the values of the heat capacity increment for the polymer being in the PL state and in the HPS bulk at $0 < \varphi \le \varphi_{cr}$. Then, from relations (8) and (9), it follows that

$$1 - \exp(-\alpha N_i) = \frac{\rho_1}{\rho_0}\left(1 - \frac{\Delta C_1}{\Delta C_2}\right), \tag{10}$$

Therefore, the coefficient α shows at what rate the polymer from the bulk has transited into the PL at variation of the number N_i of the fine filler particles per unit.

Using relations (6), (8), and (10), let us determine Δl of the PL in the range $0 < \varphi \le \varphi_0$ from the condition

$$R^3 \rho_f \left(\frac{\rho_s}{\rho_f}\frac{V_s}{V_f} - 1\right) = \rho_1 V_{pl} \frac{2 - \exp(-\alpha N_i)}{1 - \exp(-\alpha N_i)}, \tag{11}$$

where V_{pl} is the effective volume of the PL; ρf is the filler material density; and V_s and V_f are the volume of the HPS and the filler, respectively. Let us estimate the effective density ρ1 of the PL taking into account relation (5) on the assumption that the value $W_3(\Delta l)$, according to (2) and (9), as well as the statistical distribution of the surface active centers and their interaction with the polymer

$$W_3(\Delta l) = W_0 \beta v, \tag{12}$$

where W_0 characterizes the energy of the polymer–filler interaction resulting from intermolecular and interatomic interactions of various nature [6], β depends on the number of active centers of the filler surface [1], and v is determined by the value of the polymer chain flexibility [3].

On the basis of (5) and (12), respectively, we find

$$\rho_1 = \rho_0(1 - \varphi)\exp\left[-\frac{W_0\beta}{kT}\left(1 - \frac{\Delta C_1}{\Delta C_2}\right)\right]. \tag{13}$$

For determination of the value Δl of the PL, it is necessary to solve equation (6) with respect to Δl taking into account relations (11) and (13). As calculations show, the value Δll should be written as follows:

$$\Delta l = R\left\{\left[1 + \frac{(\rho_s - \rho_f\varphi)\left(1 - \frac{\Delta C_f}{\Delta C_p}\right)}{\rho_0\varphi\left[1 + (1-\varphi)\left(1 - \frac{\Delta C_f}{\Delta C_p}\right)\exp(-W_3/kT)\right]}\right]^{1/3} - 1\right\}, \quad (14)$$

Thus, on the basis of equation (14), the PL effective thickness in the absence of coagulation structures of the filler particles depends on their dispersion, the physicochemical characteristics and concentrations of ingredients, and the conditions of formation and operation of the composite.

RESULTS AND DISCUSSION

In terms of the considered calculations of ρ_1 (13) and Δl (14), as well as the heat capacity increment ΔC_i ($i = 1, 2$), let us estimate the effective density and thickness of the PL of a representative of amorphous flexible-chain polymers—PVC (polyvinyl chloride)—containing fine metallic filler. In the studies, we used suspended PVC of the C–6359–M grade filled with fine Cu powder. The filler CCl_4 was deprived of fat, then it was boiled in methyl alcohol and dried in vacuum at $T = 393$ K up to constant weight. The predominant size of the Cu particles with the form coefficient ≈1 is equal to 12×10^{-6} m. The samples were pressed in the T–p mode at $T = 403$ K and $p = 10.0$ MPa. A number of the samples were subject to isothermal annealing at $T = T_g$ (T_g is the glass–transition temperature of the HPS) during 1 hour. The density of the composites was determined by the method of hydrostatic weighing with an accuracy of 0.03% [4]. Molecular relaxation of the PVC systems was studied by the dielectric method by virtue of the unbalanced bridge of Schering and Lynch [4] in the range of temperature $293 \le T \le 403$ K and of frequencies 20–2×10^5 Hz. As it follows from the results obtained according to relation (13) and shown in Fig. 1, for the PVC systems at $T = 300$ K, there is observed nonmonotonic variation of the value ρ1 depending on the content of fine Cu. It is taken into account that, for powderlike metals, the kinetic equation of oxidation has the form [1]

$$\beta = \frac{m_t}{m_0} = 1 - \exp(-kt^n), \quad (15)$$

where $n \le 2$; m_t and m_0 are the mass of the oxidized and initial metal, respectively; t is the time; and k is constant. At $t \le 1$ hour and $T = 403$ K, the oxide film thickness is about 15.0×10^{-10} m and the oxidation proceeds according to the scheme $Cu \longrightarrow Cu_2O$. It is considered that, on the surface of such a filler, there exist 1–2% coordinatively unsaturated atoms of metal that interact with the PVC atoms. The value $\beta = 2\%$ is selected in the calculations taking into account that the PVC is characterized by dipole–dipole, induction, and disperse interactions [6]. The intermolecular interaction is about 4×10^{-20} J [1]. It is characteristic that, in the studied range of the filler content, the PL decondensation in comparison with the initial PVC is observed. In the range $0 < \varphi \le 1.13$ vol %, the gradient of the PL density variation is about 3.2%, and, as φ increases up to 11.3 vol %, it decreases to 1.1%. Figure 1 shows the results of the Δl value variations determined according to relation (14) depending on the content of the disperse phase. The PL effective thickness appeared to decrease linearly in the whole range of PVC filling.

Studying the charge transport in PVC systems, it is supposed [4] that the volume resistivity ρV of the composites rapidly decreases at $\varphi \ge 10.0$ vol % Cu. Therefore, at $\varphi \le 10.0$ vol % fine metal, HPS are not considered as a rule. At the same time, investigation of the dependence $\log\rho_V = f(\varphi)$ has shown (Fig. 1) that variation of the $\log\rho_V$ value takes place already at introduction of first rates of the electroconducting filler. It is characteristic that, in the case of composites that were not subjected to preliminary thermal treatment (Fig. 1), introduction of ingredients in the range $0 < \varphi \le 11.3$ vol % makes a less significant contribution to the value ρV. The correlation between $\log\rho_V$ and ρ_1 ($0.67 \le \varphi \le 11.3$) vol % at I = const is observed in the form

$$\log\rho_V = A + B\rho_1, \quad (16)$$

where A and B are the parameters of linear regression calculated by Fisher's ratio test [5], being equal to 4.18 and 9.15, respectively (the confidence interval of the correlation coefficients is $0.70 < |r| < 0.91$). The dependence of the conductivity of these systems on the PL state is also shown by the relation between the current density j and Δl (Fig. 2). The reciprocal proportion between them is a direct demonstration of the fact that current carriers appear in the HPS bulk instead of being injected from contacts and/or particles of the filler (at $E \le 5 \times 10^4$ V m^{-1}).

It is found that, at constant voltage, at the PL effective thickness decrease by a factor of 10, instead of the expected increase (by the same factor), its density varies by a factor of only 1.3. It should be noted that, at long-term effect of the electric field, the current in the studied systems at U = const decreases in time rapidly

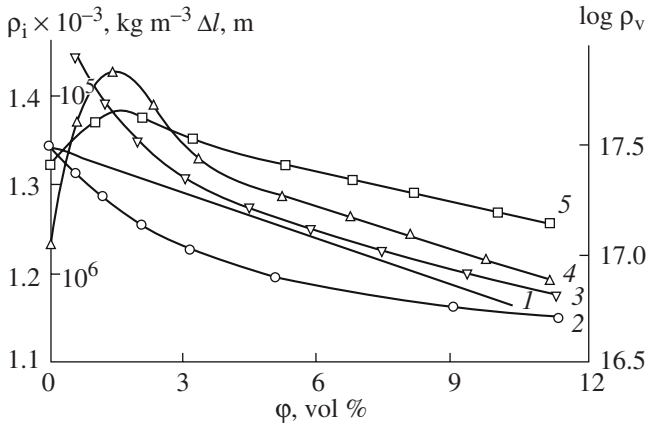

Fig. 1. Dependence of the values of ρ_i (*1* and *2*), Δl (*3*), and $\lg \rho_V$ (*4* and *5*) on the filler content on the basis of the additivity (*1*); relations (13) and (14), respectively (*2* and *3*); annealed samples (*4*); and unannealed samples (*5*) (explanations are in the text).

at first, then more slowly, achieving a stationary value (Fig. 2). For the initial period of time (up to a minute), the ampere–time characteristic is satisfactorily approximated by an exponent. After the studied sample is abridged for $t > 3$ min, the ampere–time ratio is reproduced. The dependence of the residual current value on Δl of the PL at U = const is also shown in Fig. 2. The samples were kept in the electric field for one hour. It is revealed that, at U = 150 V and at the PL thickness decrease by a factor of 10, the residual current value increases by a factor of only 1.1. Taking into account the significant inertia in the stationary current setting, its ampere–time dependence at various thicknesses of the PL for the specified mean field intensity was studied. The experiment results are shown in Fig 2; it follows from them that, as Δl increases within the studied range, the current relaxation time increases from 2 to 16 min.

Figure 2 also shows the dependence of the dielectric permeability ε of the systems PVC + Cu on the value Δl of the PL at T and f = const. One can see that an increase of the Δl value results in a decrease of ε. At higher frequency f, these variations are less. Taking into account that ε is the value directly proportional to the number of particles taking part in the polarization, the carried out calculations [3] show the increase of their number by 19% in the case of annealed PVC. However, the number of particles taking part in high-frequency dielectric losses of the annealed PVC appears to decrease by 10%. This allows stating [4] that contributions to their mean value $\bar{\varepsilon}$ are additive. Since $\varepsilon_{Cu} \longrightarrow \infty$, the formulae of Wagner [3] and Bruggeman [4] may be reduced to the form

$$\bar{\varepsilon} = \varepsilon_0 + 3\varphi\varepsilon_0, \tag{17}$$

$$\bar{\varepsilon} = \frac{\varepsilon_0}{(1-\varphi)^3}, \tag{18}$$

where ε_0 is the mean dielectric permeability of the medium surrounding the fine metal particle. Therefore, here the PL influence on the composite dielectric properties is taken into account, though implicitly. The obtained dependences (curve *5*, Fig. 2) show that, at $2.0 \times 10^{-6} < \Delta l < 4.0 \times 10^{-5}$ m, the most intense variation of the $\bar{\varepsilon}$ value is observed. It will not be suggested that, in the given range of ingredients, aggregation of Cu particles is possible. Therefore, the intense variation of $\bar{\varepsilon}$ in the specified range Δl is due to structural variations taking place in the PL. It appears that, as the Cu content increases, there is shown the existence of two competitive factors: a decrease of ρ_1 of the PL and an increase of $\bar{\varepsilon}$ due to the filler contribution to the composite dielectric properties.

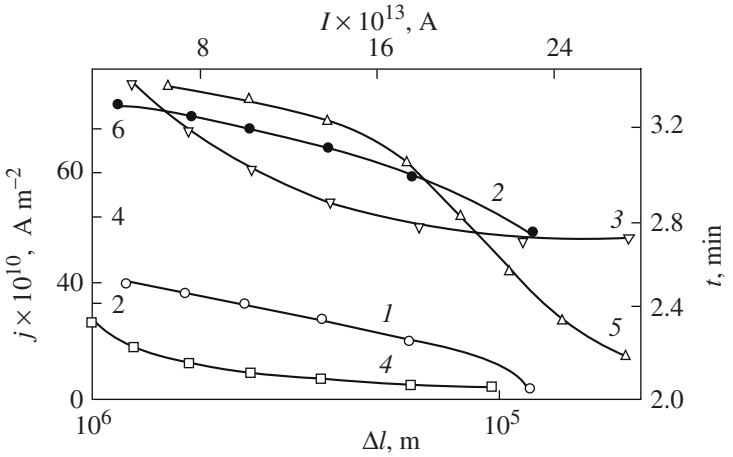

Fig. 2. Dependence of the value j (*1* and *2*) on Δl at U_1 = 70 V, U_2 = 150 V. The ampere–time dependence at $E = 10^5$ V m^{-1} and Δl: 10^{-5} m (*3*); 2×10^{-6} m (*4*); $\varepsilon = f(\Delta l)$ (*5*) at T = 310 K and f = 60 Hz.

CONCLUSIONS

It is found that surface layers act as an additional polymer modifier in the formation of the electrophysical properties of heterogeneous systems.

REFERENCES

1. Berlin, A.A. and Basin, V.E., *Osnovy adgezii polimerov* (Fundamentals of Adhesion of Polymers), Moscow: Khimiya, 1969.
2. Kuleznev, V.N., *Smesi polimerov* (Mixtures of Polymers), Moscow: Khimiya, 1980.
3. Lipatov, Yu.S., *Kolloidnaya khimiya polimerov* (Colloid Chemistry of Polymers), Kiev: Naukova Dumka, 1984.
4. Kolupaev, B.S., *Relaksatsionnye i termicheskie svoistva napolnennykh polimernykh sistem* (Relaxation and Thermal Properties of Filled Polymer Systems), Frenkel', S.Ya., Ed., Leningrad: Vysshaya Shkola, 1980.
5. Boltzmann, L., *Izbrannye trudy* (Selectas), Moscow: Nauka, 1984.
6. Kolupaev, B.B., Investigation of Viscoelastic Properties of Metal–Filled PVC on the Basis of Potential of Inter– and Intramolecular Interaction, *Inz.-Fiz. Zh.*, 2007, vol. 80, no. 1, pp. 178–186.

ISSN 1068-3755, Surface Engineering and Applied Electrochemistry, 2008, Vol. 44, No. 2, pp. 138–145. © Allerton Press, Inc., 2008.
Original Russian Text © E.I. Yantovski, 2008, published in Elektronnaya Obrabotka Materialov, 2008, No. 2, pp. 73–82.

ELECTRICAL PROCESSES IN ENGINEERING AND CHEMISTRY

Solar Energy Conversion Through Seaweed Photosynthesis and Zero Emissions Power Generation

E. I. Yantovski

Independent Researcher, Elsass str. 58, D-52068 Aachen, Germany

E-mail: iksvotnay@aol.com

Received September 20, 2007

Abstract—The present paper is aimed at describing a "closed cycle" power plant scheme (Solar Oxygen Fuel Turbine (SOFT)) with macroalgae (seaweed) cultivation in a pond, combustion of its organic matter in a fluidized bed boiler using the Rankine cycle, and return of the combustion products to the pond to feed the algae. The oxygen used for combustion is released to the atmosphere during photosynthesis. It is further elaborated in a paper presented at ECOS2005 in Trondheim. As a renewable fuel, the seaweed Ulva lactuca is selected. Its growth rate in many experiments (in the literature) is 0.1–0.2 per day, the heating value of its dry weight is 19 MJ/kg, and its optimal concentration in salt water is 1 : 1000. The energy efficiency is less than in photovoltaics, but the energy expenditures to construct the pond as a solar energy receiver are much less, so it gives some economic benefits. For a power unit of 100 kW, the pond surface is about 4 hectare. The cultivation of seaweed in sea-water ponds is well developed in Italy and Israel for water cleaning and chemical production. Construction in the future of a SOFT system near the Dead Sea in the Israeli desert would provide the country with needed power, chemicals, and fresh water using solar energy. The system is protected by United States Patten no. 6 477 841 B1 dated 12.11.2002 with priority in Israel dated 22.03.1999. Many more benefits to the customer than are in the patent text are highlighted in the paper, including fresh water by desalination. In view of the active work in Italy on water cleaning using Ulva and contaminants in the water as nutrients for an increase of the biomass productivity, an additional target of the SOFT cycle might be incineration. Some suppositions of the use of a desert surface for massive scale use of ponds are given.

DOI: 10.3103/S1068375508020117

INTRODUCTION

Seaweed is not a new thing in world industry, although it is still limited to use mostly in food and pharmaceuticals. Let us look at the report of the Irish Galway Institute quoting some specific difficulties:

These difficulties and the size of the Irish industry should be considered in relation to the international seaweed industry. About 7 million t of seaweed (wet weight) were produced world wide in 1993, of which, some 65% was food grade (Anon. 1997). Brown algae accounted for 4.9 million t, of which, Chinese production alone of the food kelp Laminaria japonica was 4 million t. Japan produced an additional 300000 t of this kelp making a total in 1995 of about 4.3 million t, which probably makes Laminaria japonica the largest single-species crop produced by aquaculture in the world. Some 250–300000 t of this material is used in China to make about 7000 t of alginates—viscous polysaccharides used in a wide variety of industrial applications, particularly in the food industry. In addition, Japan and Korea in 1993–1994 produced about 21000 million sheets of nori (about 550000 wet t). Nori is a red alga (mainly Porphyra yezoensis), and this crop is worth about US $1.5 billion; it is the most valuable single-species crop produced by aquaculture in the world. The third most valuable food species is wakame (Undaria pinnatifida), of which 750000 t were produced in Japan, Korea, and China in 1995. In 1995, in contrast, the only European production of seaweed by aquaculture was 8 wet t of wakame in Brittany, and even this small amount was more than adequate to satisfy the demand.

Most of the remaining seaweed harvesting and aquaculture goes to fuel the production of the three families of seaweed polysaccharides known as seaweed sums: alginates from brown algae and carra-geenans and agars from red algae. The wholesale value of these gums is about US $560 million. The total worth of the international seaweed business exceeds US $4.5 billion, of which Ireland has only a very small percentage.

Algae cultivation for electricity generation has been discussed in some recent decades. All algae have been divided into microalgae (with a size of some microns) and macroalgae or seaweed, which are much greater. The photosynthesis is similar in both kinds, and we will start the early history with microalgae. However, the technical problems of cultivation and combustion are different, that is why we will focus on macroalgae only.

The first published results of the use of open ponds with microalgae to convert carbon dioxide from power plants into methane fuel belong to Golueke and Oswald (cited in [1]). They demonstrated a small system involving microalgae growth, digestion to methane, and recycling of nutrients. They tried to catch the CO_2 and inject the flue gases into the pond regardless of the fact that there was a very small fraction of CO_2 in the flue gases (about 10%). Then, especially active was the Solar Energy Research Institute (SERI, now NERL) in their "Aquatic Species Program." After the testing of three outdoor algae facilities in California, Hawaii, and New Mexico, it was concluded that it is possible to produce microalgae in a large-scale pond with high productivity and relatively low cost.

Similar results published by Alexejev et al.[2] from Moscow University demonstrated a small microalgae system called "Biosolar" with production of 40 g/m^2 dry biomass in a day. The mineralized elements from the tank of the produced methane are reused by the algae. CO_2 is restored after burning. They stated "1 mtce of methane might be produced from a surface of 70 m^2 annually."

The chemistry of an algae pond was described by L. Brown [3, 4], along with the outlook for a raceway-type pond and a paddle wheel to move the water. The overall reaction for photosynthesis by cianobacteria and micro-and macroalgae is as follows:

$$CO_2 + H_2O + \text{light} \Rightarrow CH_2O + O_2. \quad (1)$$

He also stated: "We estimate that microalgal biomass production can increase the productivity of desert land by 160-fold (6 times that of a tropical rainforest). Microalgae require only 140–200 lb of water per pound of carbon fixed even in open ponds, and this water can be low-quality, highly saline water."

If the pond water is rich with nutrients as waste municipal water or released from an animal farm, very high figures of the dry biomass production have been published: 120 g/m^2 in a day [5] or 175 g/m^2 per day by Pulz (cited in [6]). These figures translate into 40–50 kg/m^2 annually.

In parallel with the ponds, some schemes of relevant power plants to use the produced biomass as a fuel have been proposed. A patent by Yamada [7] contains the use of dry algae as an addition to the regular fuel. A fraction of the flue gases is released to the atmosphere by a smoke stack, while the rest is directed to an absorption tower to be washed by water, which dissolves the CO_2 from the flue gases and returns it to the pond. The negative point of this scheme is the rather small fraction of CO_2 in the flue gases, where the dominant gas is inert nitrogen. The separation of the CO_2 from the nitrogen turned out to be an insurmountable problem.

A radical solution—the separation of nitrogen not after but before combustion—has been described by Yantovski [8] as the cycle entitled SOFT (Solar Oxygen Fuel Turbine). For further development of the SOFT cycle, see below.

Combustion of the biomass in "artificial air,"—a mixture of oxygen and steam or carbon dioxide—gives flue gases without nitrogen. The CO_2 then might be returned to the pond to feed the algae.

DATA ON ULVA GROWTH

Crucial data for the SOFT project are the productivity of Ulva under natural insolation and with an ordinary sea water temperature and chemical composition. There exists an experience of Ulva harvesting on an Irish island [20] where it is quite abundant. Besides Ulva, there exist a number of similar highly productive seaweeds.

Let us try to evaluate the possible growth rate of macroalgae with the dimensions of a branch from one to ten millimeters. For simplicity, assume the form of the organic matter particle to be a sphere.

Its volume is $V = 4/3\pi r^3$ and its cross section surface is $A = \pi r^2$. The solar energy flow density (insolation) is $\delta = 220$ W/m^2. The low heating value of the produced organic matter is $H = 19000$ J/g, the biomass density is $\rho = 800$ kg/m^3, and the efficiency of the photosynthesis is $\eta = 0.1$.

AS A RESULT OF PHOTOSYNTHESIS, THE SPHERE RADIUS IS INCREASED

According to the standard definition of the relative growth rate RGR = M'/M, where M' = the rate of the mass increase in a second or in a day and M = the mass of the organic particle, we have

$$M'/M = RGR = (3/4)\delta\eta/H\rho r,$$
$$\text{In time increase } M(t) = M_0\exp(t \cdot RGR) \quad (2)$$

The actual problem is the change of RGR in time, when (2) is invalid.

In this formula, the least known are the two following quantities: the efficiency of the photosynthesis (assume it to be 0.1) and the size of the considered particle (assume $r = 1$ mm). With these rather preliminary assumptions we, have M/M = RGR = (3/4) 220 × 0.1/(19000 × 800000 × 0.001 = 0.108 × 10^{-5} 1/s = 0.09378 ~ 0.1 1/day.

The result is in agreement with the observed data. It is evident that the more r is the less RGR is. In some research, the decline of RGR is indicated after a certain size of the particles is achieved.

The direct measurement of Ulva lactuca growth according to different insolation in shallow water (40 to 70 cm) in the Roskilde Fjord in Denmark was performed by O. Geertz-Hansen and K. Sand-Jensen in 1992 [22]. They measured the surface area A of 17 mm diameter Ulva disks. The growth rates denoted were calculated as RGR = $\mu o = \ln(A/Ao)/t$, where t = the days of incubation.

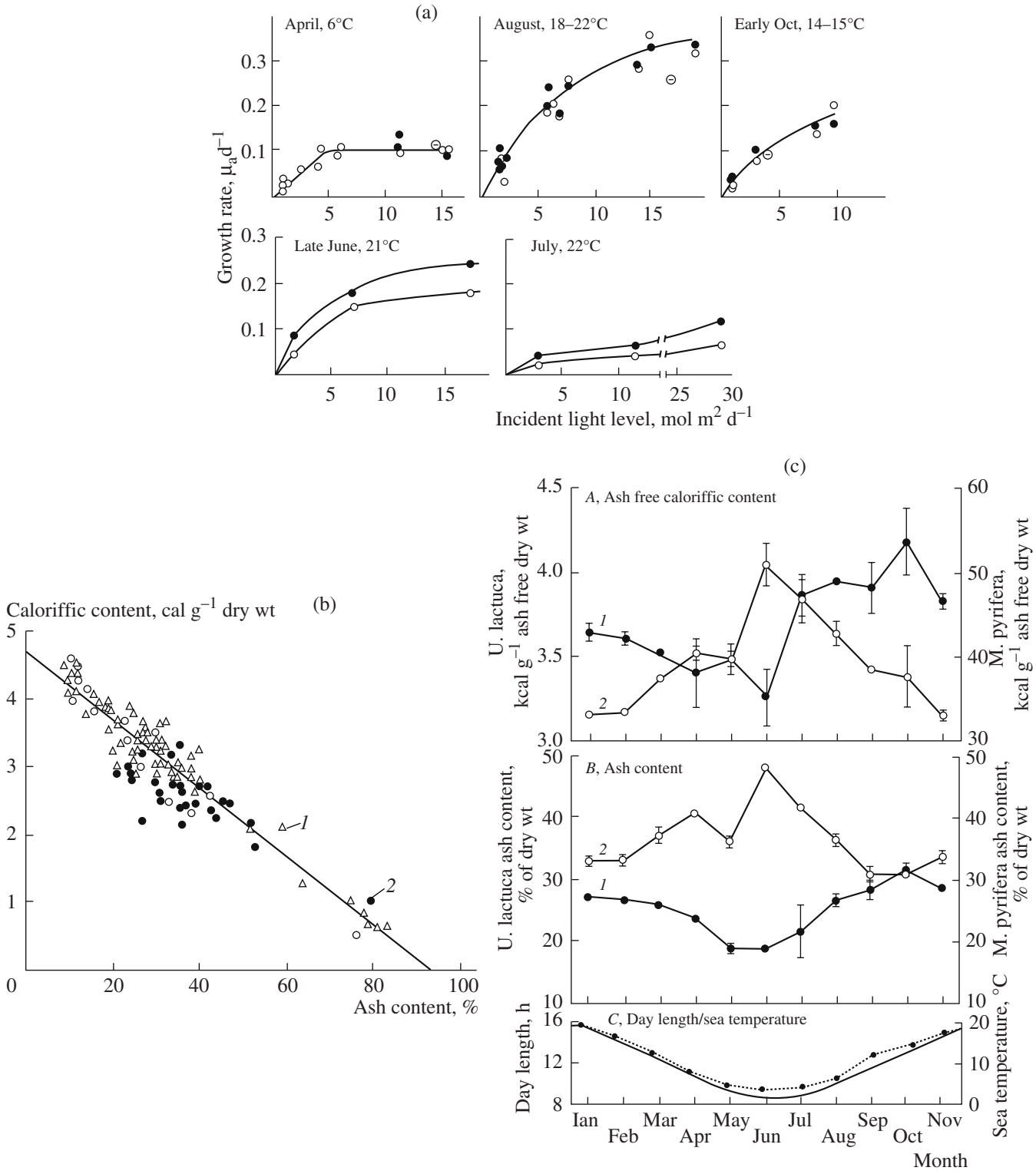

Fig. 1. (a) Growth of Ulva lactuca versus insolation. Black dots—with addition of inorganic nitrogen; open dots—without [22]. (b) Correlation line for many algae: heating value versus ash content [21]. (c) Heating value variation in a year. In New Zealand, winter is in May–Aug.

Experiments vividly show the conversion of solar energy into chemical energy in the Ulva biomass at the rather high latitude of Denmark (see Fig. 1a.) All 5 graphs are presented in RGR in units per day versus the local insolation in mol/sq.m/day. The last unit should be converted for our convenience to W/sq.m. Here, mol = mols of photons = 1 Einstein = 210 kJ, and one day = 86 400 s; hence, 10 mol/m^2 day = 24.3 W/m^2. The most important data are the rather high growth rate (up to 0.3/day) in the natural conditions of 55° latitude with modest insolation and real temperatures. In Israel, it might be much higher due to the warm winter.

The most productive seaweed Ulva is already used for water cleaning (denitrification). The experience provides a value for the SOFT cycle.

As the depth of the ponds here is 1 m, the dry weight of the Ulva biomass is 1.5 kg per m^3 of water and the growth rate is 0.1/day. The daily produced biomass is 1200 kg (case B) = 13.8 g/s. If we assume that the LHV of the biomass = 19000 J/g, the energy flow in the biomass as a fuel is 262.2 kW. Assuming a realistic efficiency of the fuel into power conversion of 25% (even in small units as in microturbines or piston engines of ZEMPES), the produced power from such pond with a 0.8 ha surface is 65.5 kW, or 100 kW from 1.22 ha. In the subsequent calculations, the same power requires 4 ha due to the lower assumed biomass productivity. It is possible since the photosynthesis during denitrification is more productive than in sea water without nitrides.

The role of nitrides is mentioned in an earlier work.

We recorded specific growth rates (NGR) ranging from 0.025 to 0.081 d^{-1} for a period up to two months in repeated short-term experiments performed at relatively low initial algal densities (300–500 g AFDW per m^{-3}). These NGR are significantly related to dissolved inorganic nitrogen (DIN) in the water column. The tissue concentrations of total nitrogen (TN) were almost constant, while the extractable nitrate decreased in a similar manner to the DIN in the water column. The total phosphorus showed considerable variation, which was probably linked to pulsed freshwater inflow.

In the long-term incubation experiment, the NGR of Ulva was inversely related to the density. The internal concentrations of both total P and TN reached maximum values after one month; thereafter, the P concentration remained almost constant, while the TN decreased below 2% w/w (by dry weight). The TN decrease was also accompanied by an abrupt decrease in the nitrate tissue concentration. The biomass incubated over a two-month period suffered a progressive N limitation as shown by the decreasing NY ratio (49.4 to 14.6). The reciprocal control of Ulva against the biogeochemical environment and vice versa is a key factor in explaining both the resource competition and the successional stages in primary producer communities dominated by Ulva. However, when the biomass exceeds a critical threshold level (approximately 1 kg of AFDW per m^{-3}), the macroalgal community switches from active production to rapid decomposition, probably, as a result of self shading, the biomass density, and development of anaerobic conditions within the macroalgal beds.

Systematic measurements of Ulva growth under the natural conditions of a coastal lagoon (Sacca di Goro in the Adriatic Sea in Italy) were made by Viaroli et al. [23]. In a 26 km^2 area with an average depth of about 1.5 m, they observed different chemical contents of the water and they recorded an RGR of Ulva of about 0.05–0.15 per day. This is a renewable source of fuel for the SOFT cycle in the gigawatt range.

MACROALGAE AS A RENEWABLE FUEL

Having looked at a growth rate of about RGR = 0.08 – 0.23 in the literature and a fantastic "calibration value" of RGR = 0.4509, we need to learn the main property of any fuel—the heating value. Sometimes, it is called the calorific value when measured in calories. In the literature, one may see rather different values from 10 to 19 MJ/kg. The question is what is meant by kg, dry or wet, and with ash or without. The most comprehensive seems to be the work by M.D. Lamare and S.R. King [21]. Here, dry algae samples are disintegrated and combusted in a bomb.

Extrapolating to 0 ash we see that 4.7 kcal/g of dry wt = 19.64 kJ/g, which might be accepted for all organic matter of different algae. For 10% ash, it is about 19 kJ/g, which is selected for the forthcoming energy conversion calculations. As an inorganic substance is absorbed from water solutions without photosynthesis, it seems to be out of the energy balance.

The heating value of algae depends on the season of growth (see Fig. 1b).

Considering this, the heating value of Ulva seems to be a little less than 19 MJ/kg. However, we will use just this figure as it is more statistically proven.

MACROALGAE CULTIVATION IN ISRAEL AND ITALY

The crucial data for this paper are based on Israeli experience [9]. There were in 1998 three raceway-type ponds, each with a surface of 1500 m^2 with paddlewheel sea water circulation. CO_2 is supplied by a tank on a truck and injected into the water by perforated tubes. The depth of the water is 0.4 m, and the hydrogen factor is pH = 7. Firm figures were obtained for the seaweed Gracilaria only. The stable productivity of dry mass from the ponds was 12 t/year, or 8 kg/sq m year. By the use of the seaweed Ulva, the expected productivity is doubled. These ponds are located in Northern Israel near to the shore of the sea, from where the sea water is pumped into the ponds. Still, the produced biomass is used as raw material for chemicals and pharmaceutics. Recently, some headway in seaweed culti-

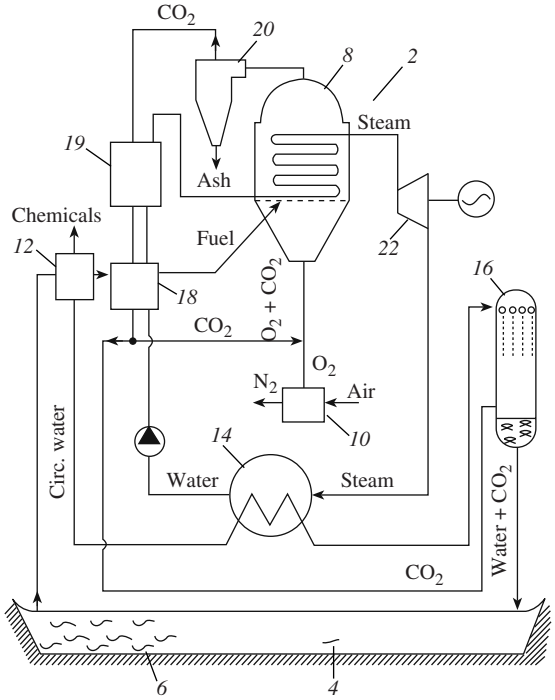

Fig. 2. Schematics of the SOFT cycle [15].

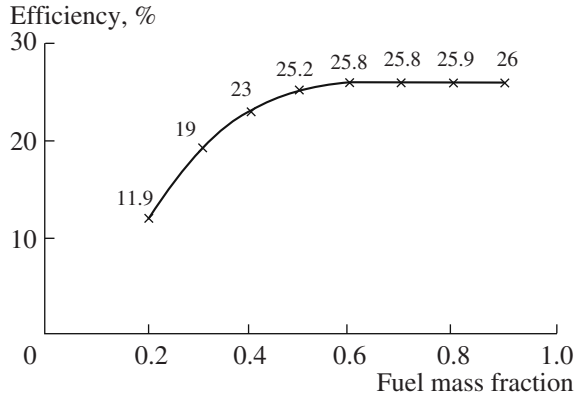

Figs. 3 and 4 from the patent description. The efficiency versus fuel wetness and a version of the SOFT cycle with fuel gasification.

vation was made by Noritech Seaweed Biotechnologies Ltd.

In Italy, the main practical interest in Ulva seems to be concentrated in water cleaning and denitrification [16–19], where much research has been done in Genova, Venice, and Parma Universities. Their active work gives an opportunity to use the SOFT cycle also as an incinerator with deflecting extra nitrides, heavy metals, and other contaminants using a fuel separation device to dispose of them perhaps underground at some depth.

ENERGY FLOW CONCENTRATION

The main obstacle of solar energy capture is its very low current density, especially when annually averaged. In Israel, it is about 220 W/m^2, only 16% of the solar constant 1368 W/m^2. In Central Europe, it is half. Thus, the energy expenditure and the cost of the incidental energy absorber is of primary importance. In the case of photovoltaics with rather high efficiency (in a laboratory, about 30%; in practice, half that), the required pure silicon absorber requires for its manufacturing lots of energy and money. That is why solar cells are up to now rather expensive. As will be shown later, the efficiency of solar energy conversion into electricity using an algae pond is much less (about 3–5%). However, the energy expenditure for the absorber–pond is a hundred times less than that for silicon.

Having been absorbed by algae, the solar energy in chemical form is concentrated by a water flow much better than by an optical concentrator. The concentration factor of a paraboloid concave mirror is about 500; this means the averaged focal spot energy current density is about $500 \times 220 = 110$ kW/sq m.

The energy flow in the pipe from an algae pond to the processing is about

$$\alpha \times \rho \times V \times H = 0.001 \times 1000 \times 1 \times 19 \cdot 10^6 = 19000 \text{ kW/m}^2 \quad (3)$$

Here, $\alpha = 0.001$ = the mass fraction of biomass in the water, $\rho = 1000$ kg/m^3 = the water density, $V = 1$ m/s = the water velocity, and $H = 19$ MJ/kg = the dry biomass heating value.

It is evident that the energy current density in the pipe is a hundred times more than that at the focal point of an optical concentrator (hydrodynamic concentration). This means the equipment size for the subsequent energy conversion processes should be rather small. It is more important than the large size of a solar energy absorber.

POWER UNIT OUTLOOK

A schematic is presented in Fig. 2. Water with algae 6 from pond 4 is going to water separation unit 12, from where the pure water without algae is used as circulating water to cool condenser 14 and absorb CO_2 in 16. Wet organic matter is dried in 18 by the heat of flue gases. Relatively dry fuel is directed to the fluidized bed combustor 8. After combustion in the artificial air (a mixture of oxygen and carbon dioxide), the flue gases go into cyclon separator 20, and then the deflected ash is returned into the pond. CO_2 with some steam goes through heat exchanger 19 and fuel drier 18 to a separation point, from where a major part is mixed with oxygen, forming artificial air for the fluidizer, and a minor part is directed to absorber 16 to be dissolved in the circulation water and returned to the pond. This minor fraction of the CO_2 flow is exactly equal to the CO_2 that appeared during the combustion. Oxygen is

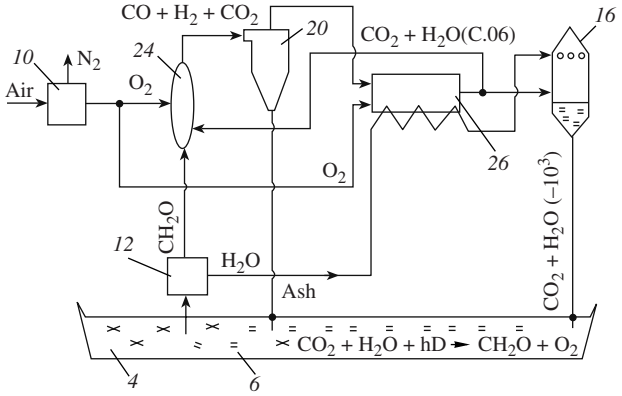

Fig. 4.

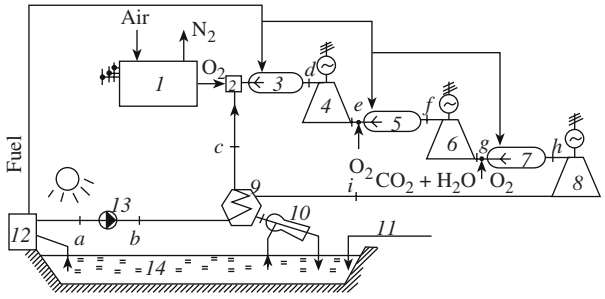

Fig. 5. First version of the SOFT cycle (1991). *1*—Oxygen plant; *2*—Steam-oxygen mixer; *3*—First combustion chamber; *4*—HP turbine; *5*—Second combustion chamber; *6*–MP turbine; *7*—Third combustion chamber; *8*—LP turbine; *9*—Recuperate; *10*—Jet condenser; *11*—Make-up water; *12*—Fuel and water plant; *13*—Feed water pump; *14*—Photosynthesis solar pond.

produced from air at the cryogenic or ion transport membrane (unit 10). Water from condenser 14 goes by a feed water pump through heat exchangers 18 and 19 into tubes of fluidized bed combustor 8 (boiler). The produced steam expands in turbine 22 driving a generator. Low pressure steam is condensed in 14. Actually, it is the ordinary Rankine cycle.

Some words on the chemical production follow. It is unwise to combust crude seaweed at a power plant in the same sense that it is unwise for crude oil. A small mass fraction of seaweed contains very useful organic chemicals, which should be deflected along with the water separation before the fuel combustion. There exist lots of methods of high organics separation, which is far from the scope of the present paper. In any case, the chemicals production could improve the economics of the SOFT cycle.

Let us take for a numerical example the decentralized power supply of a small power plant of 100 kW [10]. In order to get reliable figures, we make rather modest assumptions:

—the fuel is wet (50% water content);

—the ASU power consumption with 98% oxygen purity is 0.22 kWh/kgO_2;

—the superheated steam before the turbine is at 130 bar and 540°C;

—the isentropic coefficient of the turbine is 0.80 and that of the feed pump is 0.75;

—the seaweed productivity is 16 kg/m^2 per year, or 10 W(th)/m^2; and

—the photosynthesis efficiency is 4.6%.

The calculated results are as follows:

—the heat input is 425.5 kW(th),

—the net output is 107.3 kW (el),

—the cycle efficiency is 25.2%, and

—the pond surface is 4 ha.

A graph of the efficiency versus the fuel moisture can be seen in Fig. 3. For quite possible figures of the Rankine cycle with reheating and efficiency of 35% the needed surface of the pond is 3 ha. For an Israeli kibbutz of some hundred people, only 4–5 such units and a pond of 15–20 ha are required. For a local power plant of 10 MW with a cycle efficiency of 40% and photosynthesis efficiency of 6%, the specific power per square meter is about 5 W ($220 \times 0.4 \times 0.06 = 5.28$) and the pond size is about 2 km^2. By order of magnitude, it is comparable with the Yatir reservoir in the Negev desert near to Beer Sheva. The Keren Kayemeth Lelsrael [11] is planning to build 100 water reservoirs in the next five years. One of these might be used for a SOFT demonstration.

Fig. 6. Location of the tentative Life Sea in the Negev desert in the middle of the channel of the Red Sea–Dead Sea.

Finally, for the national power demand of 10 GW (about 2 kW per capita) in Israel, a reasonable extrapolation is possible: an expectation of specific power of 10 W/m^2 due to increasing the cycle efficiency and the photosynthesis. This means the needed pond surface is about 1000 km^2. The surface of the Dead Sea is just the same (exactly 980 km^2). If in the future a Life Sea (with a normal, not deadly salt concentration for seaweed) appears in the desert not too far from the Dead Sea (see Fig. 6), it could give the country full electrical power along with lots of fresh water and organic chemicals. There would be no emission of combustion flue gases and no net consumption of oxygen, which is consumed in combustion but released in photosynthesis. The only requirement is solar energy and a piece of desert. Also, a terror attack could not cause any serious damage.

An Israeli group represented at the Johannesburg Summit by Mr. Jacob Keidar announced the Israeli–Jordanian project of a 300 km long pipeline just from the Red to the Dead Sea. The Life Sea might be a useful consumer of the transferred water at the middle of the pipeline (see Fig. 6).

GASIFICATION

In a proper energy mix, not only electricity but also gaseous or liquid fuel is needed. In the SOFT cycle, it is attainable by a small modification (Fig. 3). The difference is the incomplete combustion (gasification) in the fluidized bed reactor (now it is gasifier 24). Biomass gasification is well documented [12]. Fluidized bed gasification experiments with the sugarcane bagassa are described by Gomez [13]. The produced gaseous fuel mixture consists of carbon monoxide, hydrogen, and carbon dioxide. After cleaning in 20, it is used in piston engine or turbine 26, thus producing mechanical power. The same fuel–gas mixture might be converted into liquid fuel such as methanol or even gasoline. After combustion in 26, the flue gases are absorbed by circulated water and returned to pond 4 to feed seaweed 6.

The figures in brackets (0.06 and 10^3) reflect the mass ratio of water/CO_2.

WATER DESALINATION

For the state of Israel, the problem of fresh water is not less severe than of electrical power supply. The annual demand is about 1.4 km^3 of fresh water. It rains only 50 days in a year, and 60% of the land is desert.

Let us consider what the SOFT cycle might do for water desalination: is it possible to use the low-grade heat after the turbine expansion to evaporate of a fraction of the circulating salty water (sea water) with the subsequent condensation of vapor for fresh water production (desalination).

Assume an evaporator of a minor fraction of the circulating water after the turbine. Cooling and condensing this vapor by the major part of the circulating water gives fresh water as a condensate.

How large is its flow rate? Assume the turbine to be of a back-pressure type with an exiting steam pressure of 1.2 bar. If, in a modern high-temperature steam turbine, the inlet is characterized by 1000 K and 200 bar, the enthalpy is 3874 kJ/kg. After the expansion, the steam is at 450 K and 2830 kJ/kg. For water evaporation at 1 bar, an enthalpy drop of 2500 kJ/kg is enough.

In a small power unit of 100 kW, the mass flow rate of the cycle water of the Rankine cycle is 100/0.25.1044 = 0.4 kg/s. The mass flow rate of desalinated water is the same: 0.4 kg/s.

For a small demonstration plant, the figures are as follows:

—Pond surface 4 ha (40000 m^2),

—Power 100 kW,

—Dry fuel flow 0.021 kg/s,

—Chemicals (4%) 1 g/s,

—Fresh water 0.4 kg/s.

The specific dry fuel consumption is 756 g/kWh. It is about twice the standard fuel consumption in microturbine power units due to the lower heating value and low efficiency.

In a 1 GW power plant with cycle efficiency of 40% and a pond surface of 10 × 20 km, the flow rate of the produced fresh water is 4 t/s, or 14 400 t/h. Assuming 7000 h/year of operation, the yield of water annually is about 0.1 km^3. It is evident that, if the SOFT cycle with water desalination is used at full scale, it might meet all the water demands. The contemporary practice of the use of 18 power generating and desalinating plants at the West Bank of the Arabian Gulf [14] giving 15 GW of power and 1.9 km^3 of desalinated water annually confirms the above guesses. In the case of the applicability of the experimental results of Italian researchers [16–18] with higher growth of Ulva, the size of the mentioned ponds might be much reduced.

COMPARISON WITH THE FIRST SOFT VERSION OF 1991

The closed cycle power plant concept based on algae photosynthesis in a pond, combustion of organic matter of dried algae in a zero-emission power plant, and CO_2 capture to return it to the pond for feeding the algae was published in 1991 [8] (see Fig. 5). There was used air separation and expansion in a steam turbine. The difference was that an inert gas replaced nitrogen in the combustor. It was not carbon dioxide but steam. Also, the algae was different: not macro but micro, that is why not a fluidized bed combustor but a gas-turbine one as for clean fuel was assumed. After the triple expansion in the turbines together with steam, the carbon dioxide was returned to the pond. Now, this version is actively being used by Clean Energy Systems (CES), which is creating a demonstration plant of 5 MW in

California not for algae but for ordinary gas fuel. It might be the first zero emission power plant. If it is successful, an algae fuel system for a SOFT cycle demonstration might be added.

CONCLUSIONS

The seaweed Ulva, which was selected as a renewable fuel for the SOFT cycle, is well documented. Its main properties are the following: a relative growth rate of RGR = 0.1–0.2 per day (or 10–20 times in a month with averaged insolation) and a heating value of 15–19 MJ/kg of ash-free dry weight. The optimal concentration of organic matter in the water is about 1 : 1000 by mass.

The SOFT power cycle, which is protected by a United States patent [15], is of practical interest for countries with sufficient solar radiation. The concept is ready for engineering, economic calculations, and demonstration. It is a nonfossil fuel, nonnuclear, nonpolluting, and nonoxygen consuming power cycle with the least expensive receiver of solar radiation and effective hydrodynamic concentration of the energy flow. Its additional service to the human environment might be incineration by combusting Ulva with nitrides and other contaminants from added brackish water.

REFERENCES

1. Benemann, J., Utilization of Carbon Dioxide from Fossil Fuel Burning Power Plants with Biological Systems, *Energy Convers. Mgmt*., 1993, vol. 34 nos. 9–10, pp. 999–1009.
2. Alexejev, V.V. et al., Biomass of Microalgae Use for Solar Energy Conversion, Techno-Economic and Ecology Aspects of Ocean Energy Use, TOI Vladivostok, 1985, pp. 53–58 (in Russian).
3. Brown, L. and Zeiler, K., Aquatic Biomass and Carbon Dioxide Trapping, *Energy Convers. Mgmt*., 1993, vol. 34, nos. 9–10, pp. 1005–1013.
4. Brown, L., Uptake of Carbon Dioxide from Flue Gas by Microalgae, *Energy Convers. Mgmt*., 1996, vol. 37, nos. 6–8, pp. 1363–1367.
5. Bull, L.E., Monaco: De l'Institute Oceanografique, 12/1993.
6. Kurano, N. et al., Carbon Dioxide and Microalgae, vol. 114 of Advances in Chemical Conversions, Inui, T., et al., Eds., Elsevier: Studies in Surface Sci. and Catalysis, 1998.
7. Yamada, M., Recovery and Fixation of Carbon Dioxide, Patent of Japan 03154616, applied 10.11.1989, publ. 02.07.1991.
8. Yantovski, E., The Thermodynamics of Fuel-Fired Power Plants Without Exhaust Gases, World Clean Energy Conference CMDC (Geneva, 1991), 4–7 Nov., pp. 571–595.
9. Uri, O., Seaweed Cultivation Project in Israel, Rosh Hanicra, 1998 (private communication).
10. Iantovski, E., Mathieu, Ph., and Nihart, R., Biomass Fuelled CO_2 Cycle with Zero Emission, Proc. Powergen Europe. (Madrid, 1997).
11. LeIsrael, K.K., Wasser fur Israel, Judisher Nationalfonds e.V. 2003.
12. Olsson, et al., Cogeneration Based on Gasified Biomass, Proc. ECOS'2000 (Nederlands), vol. 4, pp. 1945–1957.
13. Gomez, E., Preliminary Tests with a Sugarcan Bagasse Fuelled Fluidised Bed Air Gasifier, *Energy Conv. Mgmt*., 2001, vol. 40, pp. 205–214.
14. Azoury, P.H., Power and Desalination in the Arabian Gulf Region, *Proc. Instn. Mech. Engrs*., 2001, vol. 215, part A, Imech E.
15. Yantovski, E., Closed Cycle Power Plant, US Patent 6477841 B1, Nov. 12, 2002.
16. de Casablanca, M.-L. et al., Growth Rate of Ulva Rigida in Different Mediterranean, *Bioresource Technol*., March 2002, vol. 82, pp. 27–31.
17. Bartoli, M. et al., Dissolved Oxygen and Nutrient Budgets in a Phytotreatment, *Hydrobiologia*, Nov. 2005, vol. 550, no. 1.
18. Vezzulli, L. et al., A Simple Tool to Help Decision Making, *Water SA*, Oct. 2006, vol. 32 no. 4.
19. Giusti, E. and Marsili-Libelli, S., Modelling the Interaction Between Nutrients and the Submersed Vegetation in the Orbetello Lagoon, *Ecological Modelling*, 2005, vol. 184, pp. 141–161.
20. Yantovski, E. and McGovern, J., Solar Energy Conversion through Seaweed Photosynthesis with Combustion, Zero Emission Power Plant, Proc. Conf. Renewable Energy in Maritime Island Climates (26–28 Apr. 2006, Dublin, Ireland), pp. 23-27.
21. Lamare, M.D. and Wing, S.R., Calorific Content of New Zealand Marine Macrophytes, New Zealand *J. Marine Freshwater Res*., 2001, vol. 35, pp. 335–341.
22. Greertz-Hansen, O. and Sand-Jensen, K., Growth Rate and Photon Yield of Growth in Natural Populations of a Marine Macroalga Ulva Lactuca, *Mar. Ecol. Progr. Ser*., 1992, vol. 81, pp. 179–183.
23. Viaroli, P. et al., Nutrient and Iron Limitation to Ulva Blooms in a Eutrophic Coastal Lagoon, *Hydrobiologia*, 2005, vol. 550, pp. 57–71.

ISSN 1068-3755, Surface Engineering and Applied Electrochemistry, 2008, Vol. 44, No. 2, pp. 146–153. © Allerton Press, Inc., 2008.
Original Russian Text © N. Hamdi, E. Srasra, 2008, published in Elektronnaya Obrabotka Materialov, 2008, No. 2, pp. 83–90.

ELECTRICAL PROCESSES IN ENGINEERING AND CHEMISTRY

Interaction Between Clay Soils and Acidic Wastewater: Textural and Structural Evolution

N. Hamdi and E. Srasra

Technopole Borj Cedria, Unité des materiaux, Tunis, BP 95-2050 Hammam Lif, Tunisia

E-mail: hamdinoureddine@yahoo.fr

Received November 1, 2007

Abstract—This paper reports the interaction between clay and acidic wastewater (pH = 2.7 and rich in F^-, PO_4^{3-}, Cl^-, etc.). However, this work investigates the structural and textural evolution after the leachate permeability test of clay soils from three potentials sites for acid effluents storage in the south of Tunisia (soil 1, soil 2, and soil 3). We can notice that the coefficient of permeability decreases according to the time in the case of soil 1 and soil 2 and increase from 6.8×10^{-10} to 1.1×10^{-8} m/s for soil 3. The textural changes for the three varieties of clay soils obtained after the leachate permeability test were studied through nitrogen gas adsorption at liquid nitrogen temperature; we determined the specific surface areas (SBET) and total pore and micropore volume. The textural study data have indicated that soil 1 had the lowest textural properties with a pore volume in the 0.06–0.09 $cm^3\ g^{-1}$ ranges and with a surface area (SBET) varying between 35.4 and 47.4 $m^2\ g^{-1}$. A detailed structural and morphologic modification were undertaken by scanning electron microscopy (SEM) equipped with energy-dispersive spectroscopy (EDS); their results show that soil 1 and soil 2 are able to uptake the noxious elements. By comparison, the selectivity of the elimination of these elements is in the order F > P > S for soil 1. The quantitative analysis of anions shows that the sorption capacity of fluoride for soil 1 is about 60 mg/g and is much higher compared to others anions.

DOI: 10.3103/S1068375508020129

1. INTRODUCTION

Scientific endorsements concerning barrier performances of mineral liners are indispensable for obtaining disposal site reliability, and examinations addressing the individual quality of natural clay soils are necessary. The use of argillaceous sites for industrial waste storage is due primarily to their very lowest permeability (hydraulic permeability lower than 10^{-9} m/s) [1, 2]. However, it is necessary to choose the most suitable type of clay that resists better against the waste aggressiveness (acidic, basic, radioactive wastes, etc.) and has a low porosity and high sorption capacity.

Various investigations have been carried out on clay–pollutant systems [3, 4]. Several authors [5–7] reported that the contact of a chemical solution with an argillaceous barrier gives a significant modification of the textural and structural properties. Generally, the acid solutions are the most aggressive compounds, which destroy the crystalline structure of clays, especially the octahedral layer [8]. The clay soils used for the experimental work were chosen from three Tunisian sites (soil 1, soil 2, and soil 3) originating in the Gabes region. The industrial waste consisted of an enormous quantity of solid powder accompanied by a liquid solution of high acidity (the pH varies between 2 and 3); this acid solution (leachate) is very charged with noxious elements (F, Cl, S, and P). Moreover, the leachate permeability test of the three soils was studied in our laboratory using a permeameter [9].

The present study correlates the permeability variations with the textural and structural modifications of the clay soils produced by the acid attack and noxious elements sorption in clay minerals. First, we used N_2 adsorption to determine the surface area and the pore size distribution by the MP method. Second, we used scanning electron microscopy (SEM) and energy-dispersive spectroscopy (EDS) to investigate the form variation of the particles and to detect the noxious elements fixed in the clays.

2. MATERIALS AND METHODS

2.1. Soils

The samples used in this work were provided from three sites in the south of Tunisia (soil 1, soil 2, and soil 3) in the form of intact carrots packed in PVC tubes to avoid any contamination coming from the external environment. The depths of the removal are 17.60, 10.10, and 12.15 m. The permeability tests were carried

out using the samples without modification in order to maintain the originality of the materials. The mineralogical composition of these samples is summarized in Table 1. The industrial waste contains significant amounts of solids combined with a liquid solution of pH = 2.7 heavily loaded with harmful elements (Table 2).

2.2. Permeability Test

The permeability test was carried out using an odeometer (permeameter) [9]. The hydraulic conductivity k (cm/s) governed by the Darcy law was calculated by the following equation [10]:

$$k = \frac{2.3aL}{At}\log\frac{h_1}{h_2},$$

where A is the cross section of the sample, a is the cross sectional area of the presser tube of the water column, L is the thickness of the sample, t is the time interval between the readings of the levels h_1 and h_2, h_1 is the initial height of the water, and h_2 is the final height of the water at the time t.

2.3. Textural Measurements

Nitrogen sorption isotherms at liquid nitrogen temperature (77 K) were obtained with a Quanta-chrom-Autosorbl unit using a volumetric technique. Prior to the analysis, all the samples were degassed in vacuum at 160°C for 4 hours. The BET surface areas were calculated from the nitrogen adsorption isotherm at relative pressures ranging from 0.05 to 0.35. The total pore volume was derived from the amount of nitrogen adsorbed at a relative pressure close to unity (p/p_0 = 0.99) by assuming that all the accessible pores had been filled with condensed nitrogen in the normal liquid state. We proposed here a micropore analysis method called the MP method to calculate the micropore size distribution. In the MP method [11], the surface area of a group of pores with similar pore size is obtained from the difference in the slopes of the tangents drawn at two adjacent points on the t plot. In addition, the pore volume of the pores group is then calculated from the information of the surface area and pore size assuming a pore shape. For seeing the argillaceous modification texture inside the grain, we measured the total specific surface of the clays using adsorption of ethylene-glycol [12]. The interest in this protocol is that the molecular value of the obstruction of the ethylene glycol is independent of the nature of the compensation cation load; it is equal to 2.22 m^2/mg of ethylene glycol. The total surface area is given by S_T = 2.22 p, where p is the weight of the ethylene-glycol retained after the adsorption stability in mg per gram of the sample.

Table 1. Mineralogical composition of the three soils

Sample	Mineralogical composition of the clay samples, %						
	Paly	Smec	Kao	Il	Q	Ca	Do
Soil 1	35.4	1.7	14.9	–	29.1	18.9	–
Soil 2	–	56.3	6.5	–	12.5	24.7	–
Soil 3	–	–	22.9	62.7	9.7	–	4.7

Note: Paly—palygorskite, Smec—Smectite, Kao—Kaolinite, Il—Illite, Q—Quartz, Ca—Calcite, Do—Dolomite.

Table 2. The composition of the leaching solution

Ions	Initial concentration in the wastewater, mg/L
F^-	2360
Cl^-	880
PO_4^{3-}	1500
Na^+	2836
SO_4^{2-}	1563
Ca^{2+}	850

2.4. Scanning Electron Microscopy (SEM)

The morphological observation was undertaken using a PHILIPS FEI QUANTA 200 scanning electron microscope, which was employed in the conventional high-vacuum mode using gaseous secondary electron and secondary electron detectors, respectively. To investigate the compositional variation of the untreated soil after the permeability test, semiquantitative microprobe chemical analysis by energy-dispersive spectros-

Table 3. Results of permeability for the three soils obtained using an odometer

Samples	Water permeability, m/s	Permeability test using the waste solution	
		Permeability, m/s	Test duration, days
Soil 1	8.5×10^{-10}	6.2×10^{-11}	223
Soil 2	2.8×10^{-9}	1.9×10^{-10}	287
Soil 3	6.8×10^{-10}	1.1×10^{-8}	276

Table 4. Percentage of carbonate of the soils before and after the permeability test

Samples	% of carbonate
Soil 1 crude	18.9
Soil 1 after the permeability test	7.7
Soil 2 crude	24.7
Soil 2 the after permeability test	12.1
Soil 3 crude	4.7
Soil 3 after the permeability test	3.1

copy (EDS) was performed in SEM in order to characterize the new chemical elements adsorbed in the clay soils.

2.5. Instruments for F^-, PO_4^{3-}, Cl^-, and pH Measurements

The fluoride concentrations and pH were measured using a Metrohm 781 pH/Ion Meter and an HI9321 pH meter (HANNA Instruments), respectively. The phosphate concentration was measured using the standard method [13] (vanadomolybdophosphoric acid colorimetric method) using a Hach DR/4000 spectrophotometer. The chloride was analyzed using a Metrohm 716 DMS Titrino using a silver nitrate solution.

3. RESULTS AND DISCUSSION

3.1. Permeability

The permeability study is composed of two parts: first, the determination of the permeability coefficient using water and, second, the determination of the kinetic permeability using an acidic waste solution. Table 3 summarizes the permeability coefficient k (m/s), and we observed that, for soil 1 and soil 3, the permeability is $k < 10^{-9}$ m/s. However, since the waste solution that will be stored has an acidic character (pH = 2.7), it is indispensable to determine the permeability using the leachate solution as function of the time (>200 days) (Figs. 1, 2, and 3). These results show that there exists an interaction between the waste solution and the soils where the permeability decreases according to the time in the case of soils 1–2 and increases from 6.8×10^{-10} to 1.1×10^{-8} m/s for soil 3. This amelioration of permeability found in the case of soil 2 could be due to the precipitation of some compounds that blocked the water circuit in the specimen. The consequences of the carbonate fraction degradation are relatively higher in both soils (see Table 4). In contrast, in the case of soil 3, there is probably the formation of interconnected microcracks, which increase the solution flow, because this soil has a low percentage of carbonates and a low plasticity (illitic clay), which is affected by the acidic attack. After the leachate permeability test, the specimen recovered from the permeameter was prepared for the textural and structural study.

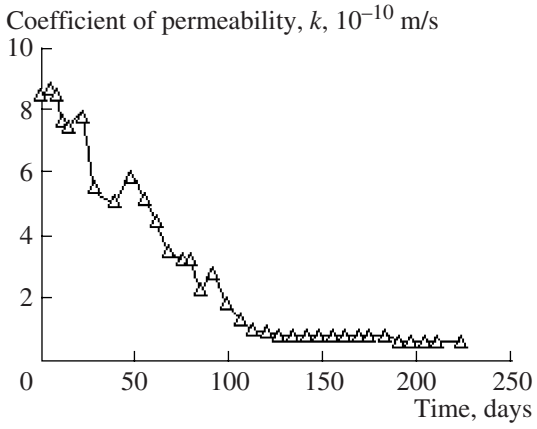

Fig. 1. Variations of the leachate permeability with time for soil 1.

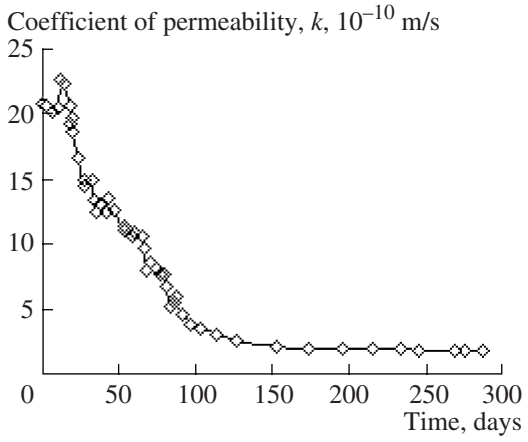

Fig. 2. Variations of the leachate permeability with time for soil 2.

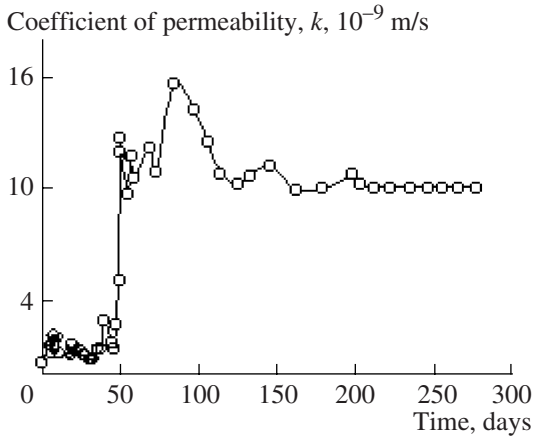

Fig. 3. Variations of the leachate permeability with time for soil 3

3.2. Textural Characterization

3.2.1. Nitrogen adsorption isotherms. Figure 4 shows the nitrogen adsorption–desorption isotherms for the three soils before and after the permeability test. The shape of the isotherms for all the samples corresponds to type II in the IUPAC classification, and, for all the isotherm curves, the hysterisis was of H_3 type characteristic of layered materials with slit-shaped pores [14]. Then, the isotherms of soil 1, soil 2, and soil 3 did not present a plateau exactly parallel to the pressure axis, which can correspond to the adsorption in some kind of mesoporosity [15].

The increase in the adsorbed volumes of the leached samples with the attack time can be explained by the increasing pore numbers in the samples of soil 1 and soil 2 [16]. The adsorption and desorption branches of the hysteresis loop of soil 3 before and after the permeability test are similar. We can notice that, in the cases of soil 1 and soil 2, the pore volume increases after the leachate permeability test; it is clear that the isotherms move upwards with the adsorbing N_2 volume.

3.2.2. Surface area, porosity and microporosity. The specific area and total pore volume of the samples before and after the permeability test as obtained from the isotherm data are collected in Table 5. In the three samples, the acid attack caused by the waste solution after the permeability test produces an increase of the specific surface S_{BET} and the micropore volume V_{mp}. A high specific surface area (S_{BET}) was obtained for soil 3 due to the important illitic fraction in this sample. Moreover, in soil 3, the textural variation (S_{BET} and V_{mp}) remains very weak. However, a higher total specific surface (S_T) was determined for soil 2 because it is constituted of smectic clay, which has a significant internal specific surface. Before and after the permeability test, the specific surface and the total pore and micropore volume of soil 1 remained the weakest.

Figure 5 shows the micropore size distributions (MPSD) of the samples calculated by the MP method. For all the samples, the height of the MPSD curve increased after the permeability test indicating an increase of the number of micropores, and the maximum of the micropore volume corresponds to the pore size (12 Å). It's due to the attack of the impurity, essentially the carbonate by the acid lixiviat. The micropore volume is highest in soil 3; also, the three curves have a Gaussian form representing a more uniform micropore size distribution in the 11–13 Å range.

3.3. Structural Characterization

The SEM/EDS analysis shown in Figs. 6, 7, and 8 exhibits the morphology and chemical composition of the three soils before and after the leachate permeability test. The composition of the untreated soil is given in Figure 6a (EDS spectra). The major elements are O, Si, and Al; the others (Mg, Fe, Na, Ca, and K) are the minor.

After the permeability test, the SEM imaging (Fig. 6b) shows that the particles' morphology

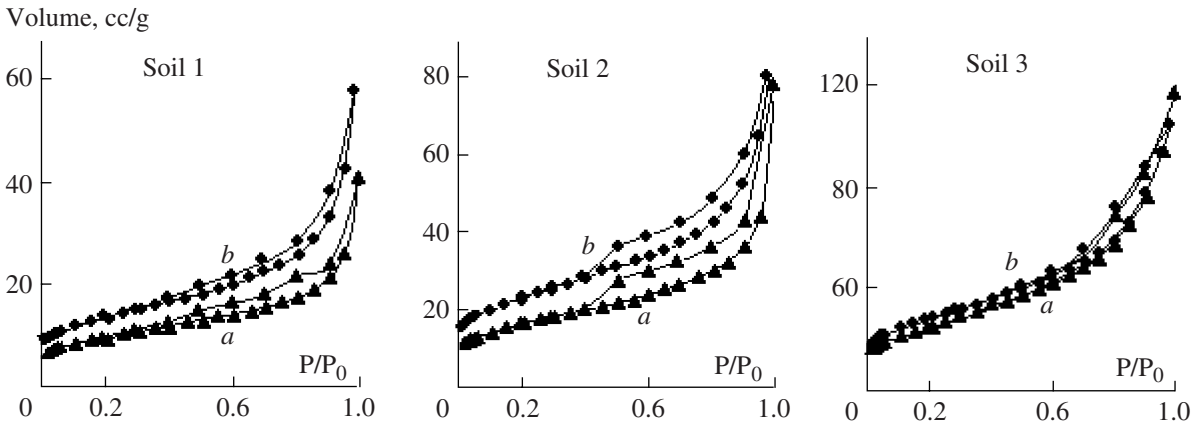

Fig. 4. Nitrogen isotherms of three soils: *a*—raw soils, *b*—samples after the leachate permeability test.

Table 5. Textural parameters of the soils before and after the permeability test

Samples	S_{BET}, m^2/g	S_T, m^2/g	V_{Tp}, cm^3/g	V_{mp}, cm^3/g
Soil 1 crude	35.4	55.7	0.064	0.013
Soil 1 after the permeability test	47.4	77.7	0.090	0.019
Soil 2 crude	57.1	209.8	0.122	0.023
Soil 2 after the permeability test	70.8	224.2	0.124	0.032
Soil 3 crude	91.5	133.4	0.216	0.035
Soil 3 after the permeability test	92.2	134.9	0.164	0.039

Note: S_{BET}—specific surface BET; S_T—total specific surface areas; V_{Tp}—total pore volume at $P/P_0 = 0.99$; V_{mp}—micropore volume.

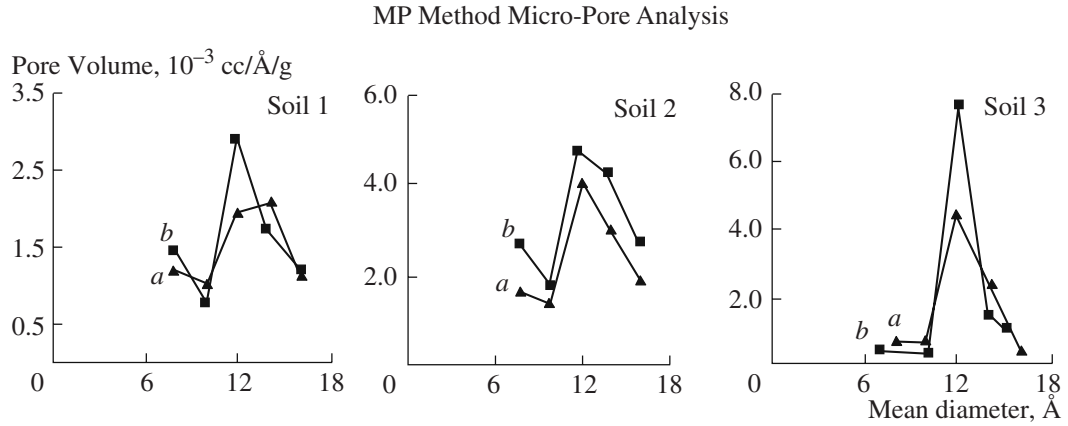

Fig. 5. Distribution of the micropore volume according to the MP method for the three soils: *a*—raw sample, *b*— sample the after permeability test.

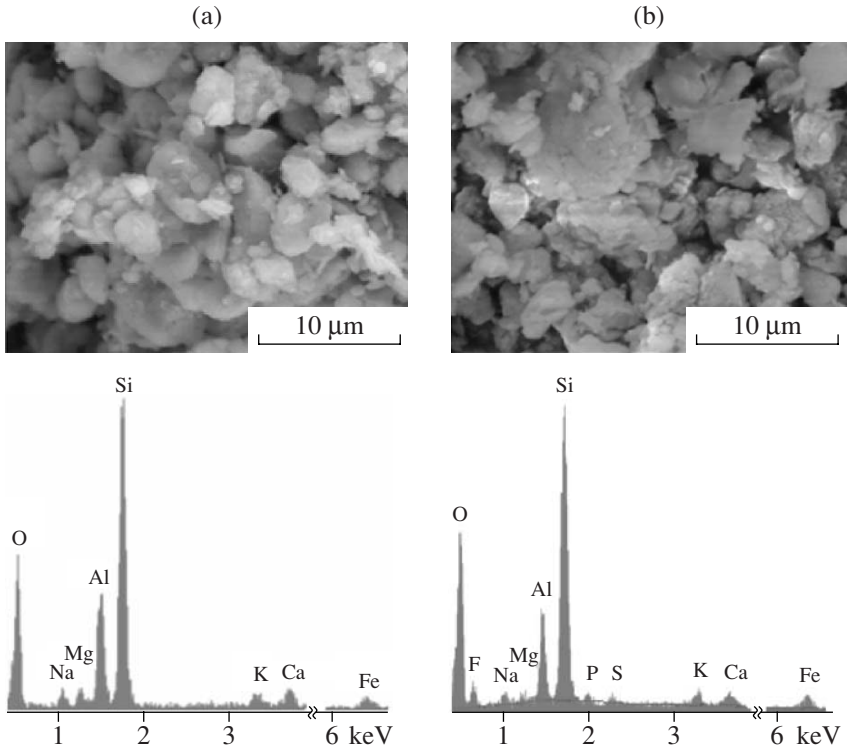

Fig. 6. SEM images and representative EDS spectra of Soil 1. (a) Raw soil; (b) soil after the permeability test.

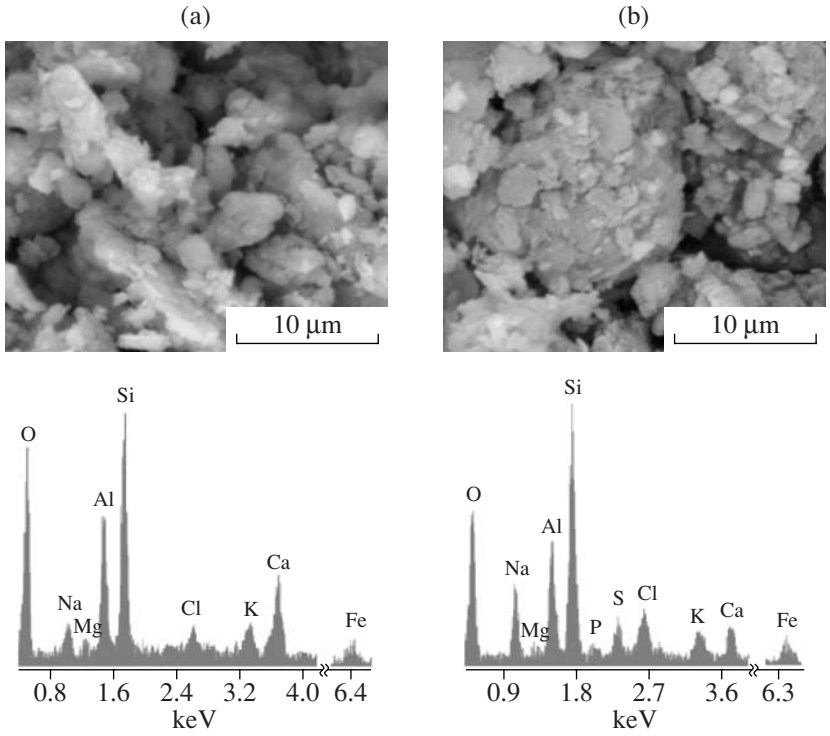

Fig. 7. SEM images and representative EDS spectra of Soil 2. (a) Raw soil; (b) soil after the permeability test.

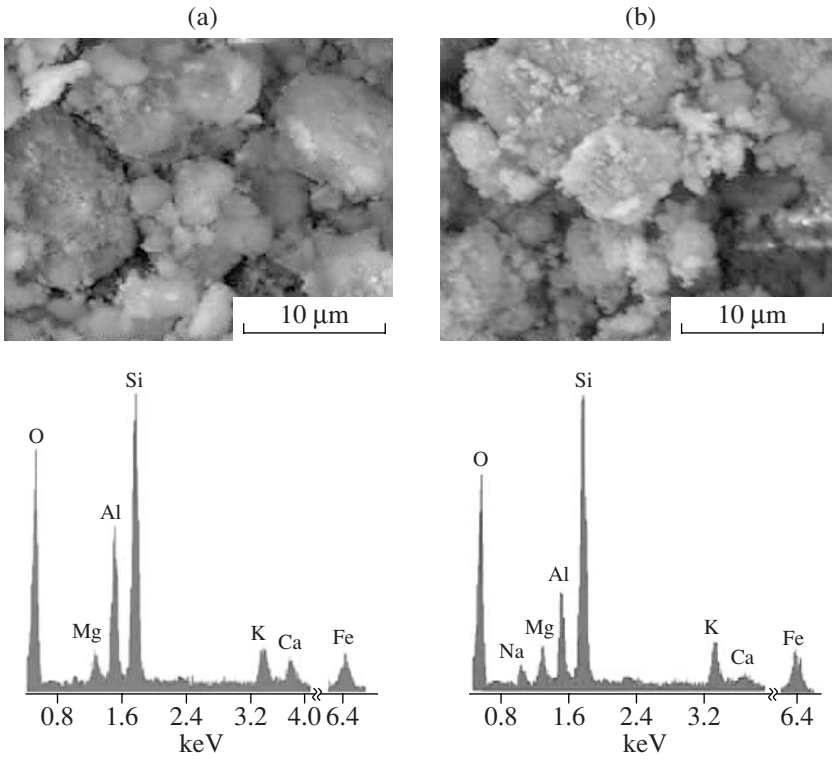

Fig. 8. SEM images and representative EDS spectra of Soil 3. (a) Raw soil; (b) soil after the permeability test.

Table 6. Sorption of anions (PO_4^{3-}, F^-, and Cl^-) from wastewater into the three soils

Anions	Removal capacity (mg/g) at pH = 2.7 and the S/L ratio = 3.33%		
	Soil 2	Soil 1	Soil 3
F^-	57.04	60.01	51.92
PO_4^{3-}	2.43	1.52	1.12
Cl^-	2.17	1.45	0.05

becomes more laminated; this is due to the attack of the impurity by the acidic waste, thus ensuring purification of the clay represented by the layers of argillaceous form. In addition, the new EDS peaks after the permeability test (Fig. 6b) are attributed to fluoride (F), sulfur (S), and phosphorus (P) and correspond to the fixation of these elements in this sample. Also, when the EDS probe was focused on a group or only one particle within the same aggregate, all showed the existence of F and S atoms. This shows the fixing uniformity of these noxious elements and reveals that this soil (palygorskitic clay) does not let pass the harmful ions to the underground water.

In the case of soil 2, Fig. 7 reveals that the morphology was modified completely and the particles becomes finer and dispersed after the acidic treatment. Therefore, the EDS analysis (Fig. 7b) shows a remarkable reduction in the Ca percentage revealing the attack of carbonates. In addition, we observe the fixation of other elements such as sulphur (S), phosphorus (P), and chlorine (Cl).

According to Fig. 8, the EDS analysis indicates that soil 3 is composed predominantly of O, Si, and Al (the Si/Al mass ratio near 2 is unity); also, greater amounts of potassium (K) are clearly observed in Fig. 7a relative to the cation and no exchangeable illite. This sample is evidently not enriched with noxious elements (Fig. 7b) after the permeability test, just a weak adsorption of sodium (Na). Moreover, we notice a reduction in the percentage of Al, thus confirming that soil 3 has been attacked by the acidic waste solution (especially, the octahedral layer).

3.4. Sorption Study of Anions into the Three Soils

The aim is to argue the results found by the EDS analysis and to quantify the removal of all the anions by these sample. A sorption study of F^-, PO_4^{3-}, and Cl^- from the waste solution was carried out using 1 g of powdered soil in 30 ml of solution; the agitation time was about 48 hours. The results for all three samples are shown in Table 6. It can be seen that the sorption capacity of anions into the three soils is in agreement with the results found by the EDS analysis in the majority of cases. Fluoride is the more selective element in soil 1, and the sorption capacity is very interesting; it is about 60 mg/g. Table 3 shows that the selectivity of the fluoride adsorption onto the three samples was 25–50 times greater than for others anions.

4. CONCLUSIONS

Based on the difference of the mineralogical composition of the three soils, soil 1 is essentially palygorskite clay mixed with kaolinite, soil 3 was illito-kaolinitic clay, and soil 2 was smectic clay associated with kaolinite and calcite. Following this study, the results of the leachate permeability show that, in the cases of soil 1 and soil 2, k decreases with the leached time. In contrast, soil 3 shows an increase of the permeability according to time. This was clearly due to the higher resistance to the acid attack and the lowest textural size of soil 1 and soil 2. Moreover, in all the samples, the specific surface area and the micropore volume increase after the permeability test was derived from an essentially carbonate attack. The EDS/SEM analysis indicates the remove of the noxious elements such as fluoride (F), sulphur (S), and phosphorus (P) by soil 1 after the permeability test and the fixation of the (Cl) in the place of (F) by soil 2. However, the sorption study of F^-, PO_4^{3-}, and Cl^- from the waste solution into the three soils shows that the fluoride is more selective for all the samples and is on the order of 60mg/g for soil 1. Based on these results, the suitable site for waste storage is soil 1 or soil 2.

REFERENCES

1. Dixon, D.A., Gray, M., and Graham, N.J., Swelling and Hydraulic Properties of Bentonites from Japan, Canada and USA, of Environmentalgeotechnics, Kamon Ed., Rotterdam, Balkema: ISBN, 1996, pp. 43–48.
2. Jozja, N., Baillif, P., Touray, J.C, Pons, C.H., Midler, F., and Burgevin, C., Impacts “multi-échelle” d’un échange (Mg, Ca)-Pb et ses consequences sur I’augmentation de la perméabilité d’une bentonite, *C. R. Geoscience*, 2003, vol. 335, pp. 729-736.
3. Lee, S.Y. and Tank, R.W., *Appl. Clay Sci*., 1985, vol. 1, pp. 145–162.
4. Roh, Y., Lee, S.R., Choi, S.K., Elless, M.P., and Lee, S.Y., *Soil Sediment Contam,* 2000, vol. 9, pp. 463–486.
5. Studds, P.G., Stewart, D.I., and Cousens, T.W., The Effect of Ion Valence on the Swelling Behavior of Sodium Montmorillonite, Engineering Techincs Press, 1996, pp. 139–142.
6. Jullien, A., Proust, Ch., Le Forestier, L., and Baillif, P., Hydro-Chemio-Mechanical Coupling Effects on Permeability and Swelling Behaviour of Ca Smectite Soaked by Cu Solutions, *Appl. Clay Sci*., 2002, vol. 21, pp. 143–153.

7. Krishna, K.M., Marion, G.R., and Scott, H.F., Formation Damage in Smectitic Sandstones by High Ionic Strength Brines, Colloids Surf., 1999, vol. 154, pp. 249–257.
8. Coméaga, L., Dispositifs d'étanchéité par géosynthétiques bentonitiques dans les centres de stockage de déchets, Thesis, France: de 1'Universite de Lyon, 1997, p. 297.
9. Hamdi, N., Della, M., and Srasra, E., Experimental Study of the Permeability of Clays from the Potential Sites for Acid Effluent Storage, *Desalination*, 2005, vol. 185, pp. 1947–1958.
10. Kalkan, E. and Akbulut, S., The Positive Effects of Silica Fume on the Permeability, Swelling Pressure and Compressive Strength of Natural Clay Liners, *Eng. Geology*, 2004, vol. 73, pp. 145–156.
11. Mikhail, R.S.H., Brunauer, S., and Bodor, E.E., Investigations of a Complete Pore Structure Analysis: I. Analysis of Micropores, *J. Colloid Interface Sci*., 1968, vol. 26, pp. 45–53.
12. Eltantawy, I.M. and Arnold, P.M., Ethyleneglycol Sorption by Monoionic Montmorillonites, *J. of Soil Sci*., 1974, vol. 25, pp. 99–110.
13. Sing, K.S.W., Everett, D.H., Haul, R.A.W., Moscou, L., Pierotti, R.A., Rouquerol, J., and Siemieniewska, T., Reporting Physisorption Data for Gas/Solid Systems with Special Reference to the Determination of Surface Area and Porosity, *Pure and Appl. Chem*., 1985, vol. 57, pp. 603–619.
14. Standard Methods for the Examination of Water and Wastewater, 1995. 19th ed., APHA, AWWA, WPCF, Washington, DC.
15. Pires, J., Araujo, A.C., Carvalho, A.P., Pinto, M.L., Gonzalez-Calbet, J.M., and Ramirez-Castellanos, J., Porous Materials from Clays by the Gallery Template Approach: Synthesis, Characterization and Adsorption Properties, Micropor. Mesopor. Mater., 2004, vol. 73, pp. 175-180.
16. Temuujin, J., Jadambaa, Ts., Burmaa, G., Erdenechimeg, Sh., Amarsanaa, J., and MacKenzie, K.J.D., Characterisation of Acid Activated Montmorillonite Clay from Tuulant, Mongolia Ceram. Int., 2004, vol. 30, pp. 251–255.

ISSN 1068-3755, Surface Engineering and Applied Electrochemistry, 2008, Vol. 44, No. 2, pp. 154–158. © Allerton Press, Inc., 2008.
Original Russian Text ©V.I. Gun'ko, L.I. Onishchenko, I.Yu. Grebennikov, A.Ya. Dmitrishin,
S.O. Toporov, E.N. Slepets, 2008, published in Elektronnaya Obrabotka Materialov, 2008, No. 2, pp. 91–97.

EQUIPMENT AND INSTALLATIONS

Study of the Compatibility of Phenyltrinitroxylenethane (Phenylxylilethane) with Structural Materials

V. I. Gun'ko, L. I. Onishchenko, I. Yu. Grebennikov, A. Ya. Dmitrishin, S. O. Toporov, and E. N. Slepets

Institute of Pulse Research and Engineering, National Academy of Sciences of Ukraine, Pr. Oktyabr'skii 43-a, Nikolaev, 54018 Ukraine

Received November 9, 2007

Abstract—The influence of structural materials on the basic electrophysical characteristics (relative permittivity, loss tangent, volume electric resistivity, and electric strength) of phenylxylilethane is considered in this paper.

DOI: 10.3103/S1068375508020130

The operation stability of high-voltage electrotechnical devices, such as high-voltage impulse capacitors, at large electric intensity in a dielectric is mainly determined by the properties of the impregnating dielectric. When selecting a liquid dielectric, one should keep in mind not only the demands for high electric strength, low dielectric loss, and resistance to the effect of partial discharges but also the requirement of the compatibility with the structural materials used. This means that the liquid shouldn't impair the physicomechanical characteristics of the structural materials used and they themselves shouldn't cause a substantial reduction of the electrophysical parameters of the liquid dielectric.

Lack of information on the compatibility of a liquid impregnating dielectric with structural materials doesn't allow predicting the safety and longevity of the electrotechnical device itself.

Phenylxylilethane, being a synthetic hydrocarbonaceous aromatic oil of the diarylalkan series possessing high resistance to gas and stability, is widely employed at present to impregnate capacitors with a dielectric on the basis of polymer films. When evaluating the influence of polymer structural materials applied in capacitor construction on the electrophysical characteristics of phenylxylilethane, there was examined the effect of the compatibility of polymer films, foil, and a metal layer [1, 2, 3], which was estimated according to the change of the loss tangent as one of the most sensitive characteristics integrally reflecting the capacitor efficiency.

In the reference literature [4, 5], information on the reciprocal influence of liquid dielectrics and structural materials is given in a general form: copper and its alloys and salts of organic acids and metals with variable valency (copper, iron, cobalt, etc.) are active catalyzers of liquid oxidation, and it is necessary to select resins individually for every fluid.

Assessment of the impact of structural materials used in capacitor construction on the electrophysical characteristics of phenylxylilethane is the aim of this paper.

The following structural materials were selected to carry out the investigation: aluminum foil A5, polyethyleneterephthalate film PET-KE, polycarbone film PK-K, polypropylene film PP-KSS, copper M1, copper tin coated with solder POS-40, brass L63, glass-epoxidephenol tubing, glass fiber laminate STEF-1, amides PA6 of type B, polypropylene interpolymer 22007-29, rubber MBS-M1, rubber 51-1434, rubber 51-1486, rubber IRP-2025, and lacquer LBS-1.

The structural material samples were placed into separate glass containers with phenylxylilethane and kept for 24 hours under the following conditions:

—residual pressure not more then 6 Pa;

—temperature (80_{-5})°C.

After exposure under the mentioned conditions, the containers with the phenylxylilethane and the structural material samples were cooled in vacuum up to the environmental temperature and were held for 48 hours.[1] The results of the measurement of the phenylxylilethane electrophysical parameters (relative permittivity ε, loss tangent $\mathrm{tg}\delta$, volume electric resistivity ρ_v, and electric strength E_{st}) after contact with structural materials are shown in the table and diagrams presented in Figs. 1–4. To make the variation of the phenylxylilethane electrophysical parameters more obvious, there are represented their values before the contact with the structural materials in the form of the base line.

The greatest reduction of the phenylxylilethane electric strength occurred after its contact with resins

[1] Gun'ko, V. I.; Onishchenko, L. I.; Grebennikov, I. Yu.; Dmitrishin, A. Ya.; Toporov, S.O.; Slepets, E. N. Elektronnaya Obrabotka Materialov, 2008, no. 2, pp. 91–97.

Compatibility testing results for phenylxylilethane with structural materials

Materials	Characteristics			
	E_{st}, kV/mm	ε	tanδ	ρ_v, Ohm/cm
Aluminum foil A5	33.12	2.523	2.811×10^{-4}	6.07×10^{12}
Polyethyleneterephthalate film PET-KE	34.08	2.512	2.806×10^{-4}	4.93×10^{12}
Polycarbone film PK-K	33.98	2.520	2.824×10^{-4}	4.78×10^{12}
Polypropylene film PP-KSS	33.76	2.522	2.810×10^{-4}	4.55×10^{12}
Steel St3	34.69	2.524	2.716×10^{-4}	4.98×10^{12}
Steel 45	34.76	2.523	2.738×10^{-4}	5.03×10^{12}
Copper M1	32.82	2.547	4.272×10^{-4}	2.43×10^{12}
Copper tin-coated with solder POS-40	34.29	2.513	3.116×10^{-4}	4.77×10^{12}
Brass L63	33.14	2.536	3.898×10^{-4}	3.73×10^{12}
Glass-epoxidephenol tube	33.88	2.534	2.344×10^{-4}	7.43×10^{12}
Glass fiber laminate STEF-1	33.60	2.541	2.819×10^{-4}	6.64×10^{12}
Amides PA6 of type “B”	33.26	2.489	3.126×10^{-4}	5.48×10^{12}
Polypropylene interpolymer 22007-29	33.51	2.521	2.916×10^{-4}	4.46×10^{12}
Rubber MBS-M1	35.43	2.547	3.017×10^{-4}	9.36×10^{12}
Rubber 51-1434	34.82	2.537	3.226×10^{-4}	6.69×10^{12}
Rubber 51-1486	33.96	2.540	3.132×10^{-4}	4.78×10^{12}
Rubber IRP-2025	32.64	2.549	4.244×10^{-4}	4.26×10^{12}
Lacquer LBS-1 deposited on cable paper K-120	34.82	2.484	3.213×10^{-4}	7.64×10^{12}

Note: Before the compatibility testing with the structural materials, the phenylxylilethane had the following characteristics: $E_{st} = 35.2$ kV/mm; $\varepsilon = 2.52$; $\tan\delta = 2.5 \times 10^{-4}$; $\rho_v = 8.37 \times 10^{12}$ Ohm/cm.

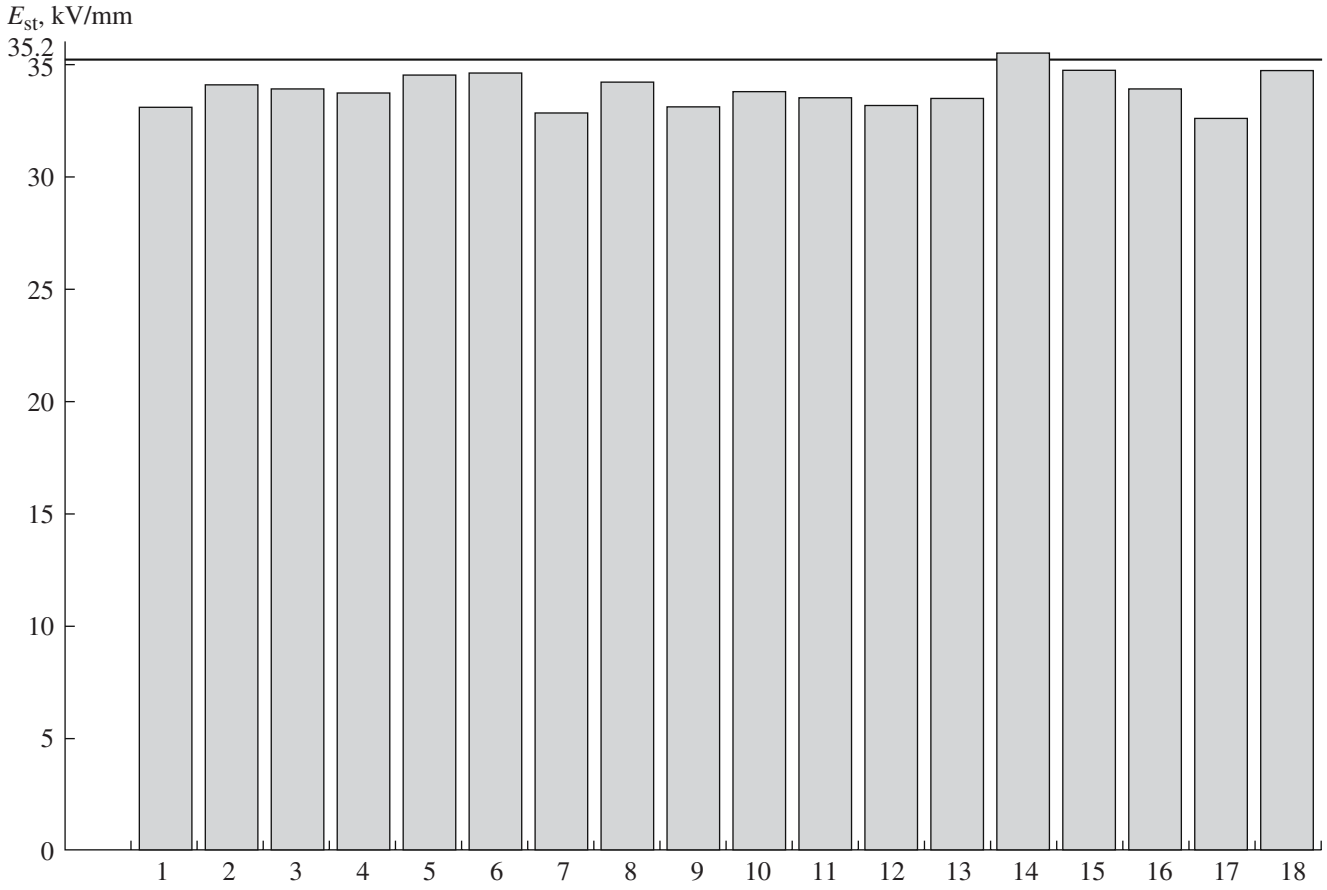

Fig. 1. Variation of the phenylxylilethane electric strength after contact with structural materials. 1 – Aluminum foil A5; 2 – polyethyleneterephthalate film PET-KE; 3 – polycarbone film PK-K; 4 – polypropylene film PP-KSS; 5 – steel St3; 6 – steel 45; 7 – copper M1; 8 – copper tin coated with solder POS-40; 9 – brass L63; 10 – glass-epoxidephenol tube; 11 – glass fiber laminate STEF-1; 12 – amides PA6 of type "B"; 13 – polypropylene interpolymer 22007-29; 14 – rubber MBS-M1; 15 – rubber 51-1434; 16 – rubber 51-1486; 17 – rubber IRP-2052; 18 – lacquer LBS-1.

51-1486 and IRP-2052 by 3.5 and 7.3%, respectively, testifying that it isn't desirable to use them in contact with phenylxylilethane. Resins MBS-M1 and 51-1434 had the lowest influence on the change of the phenylxylilethane electric strength, and they could be recommended to be utilized in constructions where phenylxylilethane is used as a liquid impregnating dielectric.

In estimating the effect of copper and its alloys (brass L63) on the electric strength value of phenylxylilethane, it can be deduced that the copper product surfaces contacting with phenylxylilethane should be tinned. Thus, after the contact with copper whose surfaces were tinned with solder POS-40, the phenylxylilethane electric strength decreased only by 2.6%, while, after the contact with copper and brass L63, the phenylxylilethane electric strength receded by 6.7 and 6.0 %, respectively.

The structural material virtually didn't affect the phenylxylilethane relative permittivity. Its largest change was observed after the contact with lacquer LBS-1 deposited on cable paper K-120 with the variation being only 1.4%.

After the contacting of phenylxylilethane with all the structural materials, the loss tangent value in some way or another arose, especially, (as was expected) after contacting with copper (by 70.8%). The greatest reduction of the phenylxylilethane volume electric resistivity occurred after the contact with copper M1 (by 70.9%) and after the contact with brass L63 (by 55.4%), while, after the contact with copper tinned with solder POS-40, the decrease was only 43%.

Generalizing the results of the conducted investigation on the assessment of the structural materials' effect on the electrophysical characteristics of phenylxylilethane, we can draw the following conclusions:

—The examined structural materials don't considerably impair the electrophysical characteristics of phenylxylilethane. As for copper and alloys based on copper, their surfaces should be tinned.

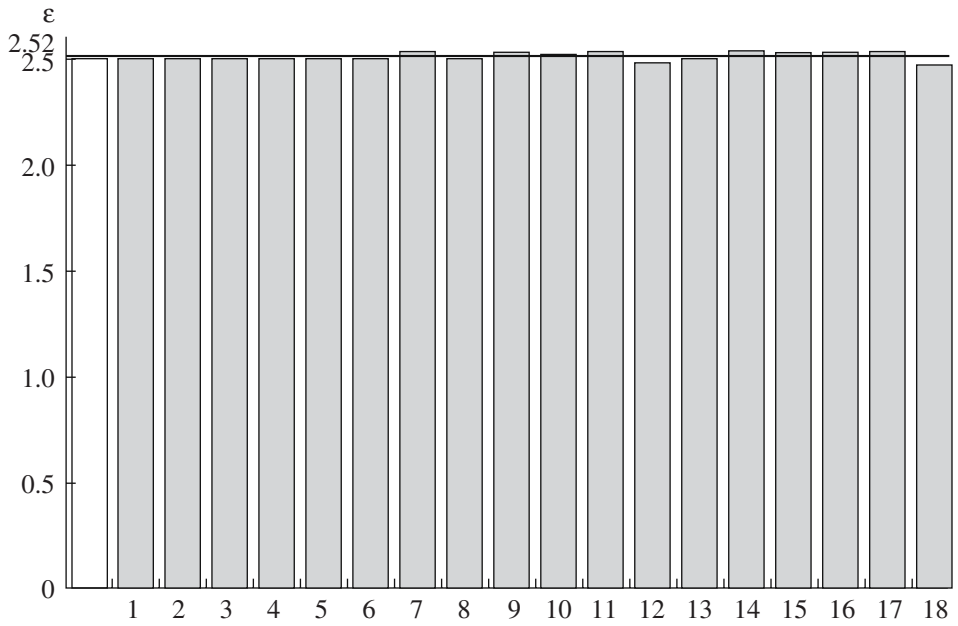

Fig. 2. Variation of the phenylxylilethane relative permittivity after contact with structural materials. 1 – Aluminum foil A5; 2 – polyethyleneterephthalate film PET-KE; 3 – polycarbone film PK-K; 4 – polypropylene film PP-KSS; 5 – steel St3; 6 – steel 45; 7 – copper M1; 8 – copper tin-coated with solder POS-40; 9 – brass L63; 10 – glass-epoxidephenol tube; 11 – glass fiber laminate STEF-1; 12 – amides PA6 of type "B"; 13 – polypropylene interpolymer 22007-29; 14 – rubber MBS-M1; 15 – rubber 51-1434; 16 – rubber 51-1486; 17 – rubber IRP-2052; 18 – lacquer LBS-1.

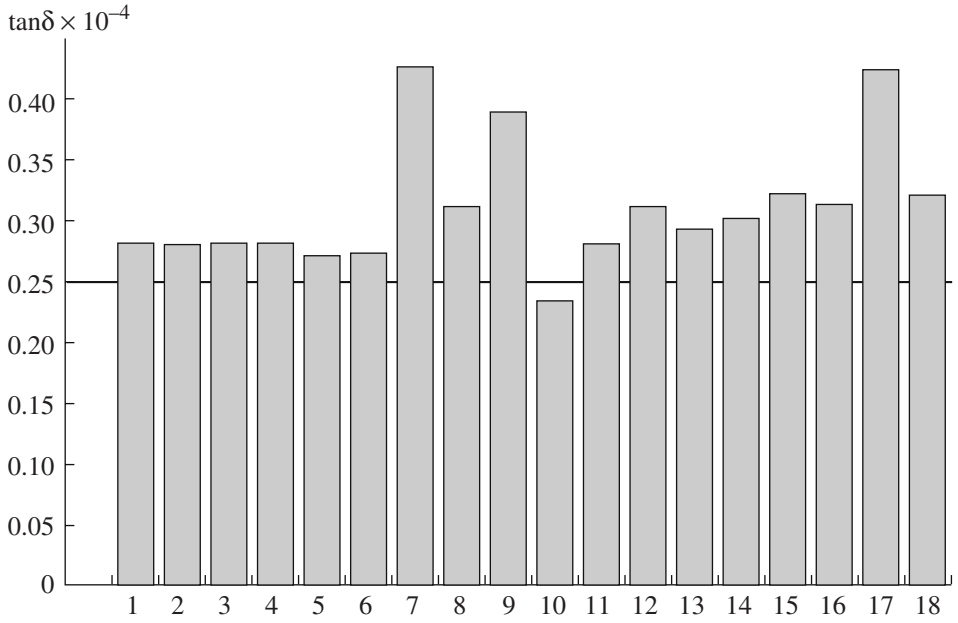

Fig. 3. Variation of the phenylxylilethane loss tangent after contact with structural materials. 1 – Aluminum foil A5; 2 – polyethyleneterephthalate film PET-KE; 3 – polycarbone film PK-K; 4 – polypropylene film PP-KSS; 5 – steel St3; 6 – steel 45; 7 – copper M1; 8 – copper tin coated with solder POS-40; 9 – brass L63; 10 – glass-epoxidephenol tube; 11 – glass fiber laminate STEF-1; 12 – amides PA6 of type "B"; 13 – polypropylene interpolymer 22007-29; 14 – rubber MBS-M1; 15 – rubber 51-1434; 16 – rubber 51-1486; 17 – rubber IRP-2052; 18—lacquer LBS-1.

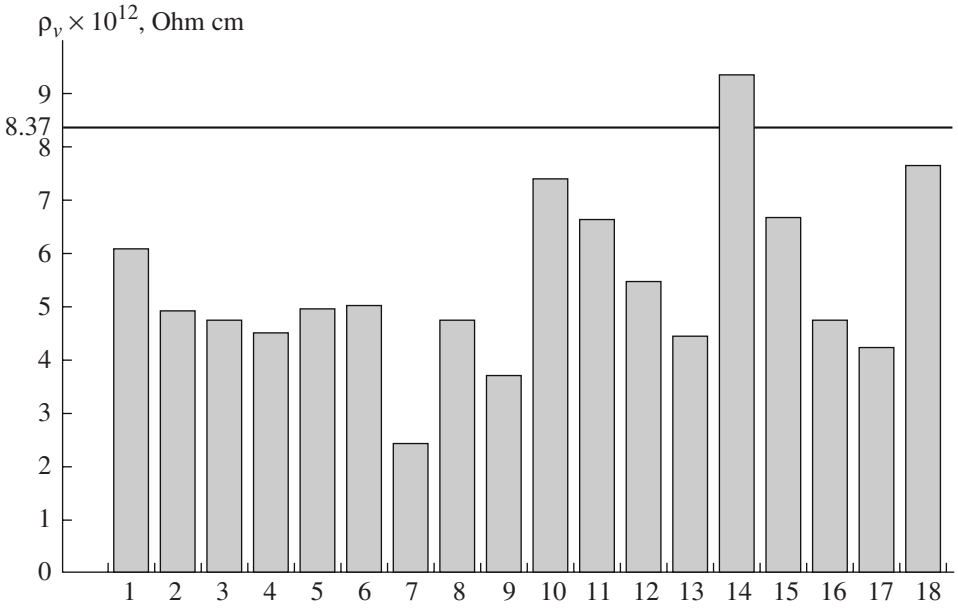

Fig. 4. Variation of the phenylxylilethane volume electric resistivity after contact with structural materials. 1 – Aluminum foil A5; 2 – polyethyleneterephthalate film PET-KE; 3 – polycarbone film PK-K; 4 – polypropylene film PP-KSS; 5 – steel St3; 6 – steel 45; 7 – copper M1; 8 – copper tin coated with solder POS-40; 9 – brass L63; 10 – glass-epoxidephenol tube; 11 – glass fiber laminate STEF-1; 12 – amides PA6 of type "B"; 13 – polypropylene interpolymer 22007-29; 14 – rubber MBS-M1; 15 – rubber 51-1434; 16 – rubber 51-1486; 17 – rubber IRP-2052; 18 – lacquer LBS-1.

—Rubbers of types MBS-M1 and 51-1434 can be recommended for use when there is possible contact with phenylxylilethane.

The obtained results can be applied for designing not only high-voltage impulse capacitors but also many other electrotechnical devices where phenylxylilethane is used.

REFERENCES

1. Zhuravleva, N.M., Andreev, A.M., Molodova, L.A. and Lutskaya, T.V., Selection of Impregnating Fluids for High-Voltage Film Capacitors, *Elektrotekhnika*, 1994, no. 4, pp. 55–58.
2. Andreev, A.M., Zhuravleva, N.M., Aleksandrova, N.P. and Galakhova, N.M., Change of Working Characteristics of the Film-Impregnated Capacitor Insulation due to the Interrelation of its Components, *Elektrotekhnika*, 1996, no. 3, pp. 69–71.
3. Pereselentsev, I.F., Ginsburg, S.L., Stupin, Yu.I., Impregnating Dielectrics for Power Capacitors, *Elektrotekhnika*, 1989, no. 3, pp. 47–51.
4. Berezin, V.B., Prohorov, N.S., Rykov, G.A., et al., *Elektrotehnicheskie materialy* (Electrotechnical Materials), (Reference-book), Moscow: Energoatomizdat, 1983.
5. Spravochnik po elektrotekhnicheskim materialam (Handbook on Electrotechnical Materials), Koritskii, Yu.V., et al., Eds., Moscow: Energoatomizdat, 1986.

ISSN 1068-3755, Surface Engineering and Applied Electrochemistry, 2008, Vol. 44, No. 2, pp. 159–164. © Allerton Press, Inc., 2008.
Original Russian Text ©A.M. Gashimov, K.Z. Nuriev, S.Manuchar, K.B. Gurbanov, Z.K. Nurubeili, 2008, published in Elektronnaya Obrabotka Materialov, 2008, No. 2, pp. 98–104.

WORK EXPERIENCE

Effective Efficiency Coefficients for Standard-Free Analysis of Solid Substances by the Method of Mass Spectrometry of Secondary Ions

A. M. Gashimov, K. Z. Nuriev, S. Manuchar, K. B. Gurbanov, and Z. K. Nurubeili

Institute of Physics, National Academy of Sciences of Azerbaijan,
pr. G. Dzhavid 33, Baku, AZ-1143 Azerbaijan
E-mail: arif@physics.ab.az

Received October 18, 2007

Abstract—Mass-spectrometry research of secondary ion emission (MSSI) products is a direct method of analysis of the element and isotope content of conducting and nonconducting solid substances. Similar to other methods of mass-spectrometric analysis, MSSI also has some analytical characteristics that enable one to detect a simple reaction between a concentration of the analyzed element and the registered initial signal.

DOI: 10.3103/S1068375508020142

INTRODUCTION

Mass-spectrometric investigations of the secondary ion emission products (MSSI) is a direct method of analysis of element and isotope contents of conducting and nonconducting solid substances. Similar to other methods of mass-spectrometric analysis, MSSI also has certain analytical characteristics that allow one to reveal a simple reaction between the concentration of the analyzed element and the registered initial signal.

Despite the fact that systematic investigations of secondary ion emission (SIE) was started with Beske's work [1], even at present, however, it remains to clarify one of the main moments of this method, namely, a certain inadequacy between the measured mass spectrum of the secondary ions (SI) and the chemical structure of the specimen. The reason for the disagreement is the unequal yield of ions of different elements due to the ionization peculiarities of the atoms and the mass discrimination in the separation systems and their registration. For the assessment of the above disagreement, there are generally used the coefficients of the effective efficiency (CEE) of the element being defined in relation to the internal standard [2]:

$$\frac{I_x}{I_{vn.st.}} = K^x_{vn.st.} \cdot \frac{N_x}{N_{vn.st.}}, \quad (1)$$

where I_x, $I_{vn.st.}$ are the measured analytical signals of the element being defined and the internal standard; N_x and $N_{vn.st.}$ are the concentrations of the corresponding elements; and $K^x_{vn.st.}$ is the coefficient of the effective efficiency. The magnitude $K^x_{vn.st.}$ is frequently presented as

$$K^x_{vn.st.} = X^x_{vn.st.} \cdot F_{prib},$$

where $X^x_{vn.st.}$ is the coefficient of the relative yield of secondary ions, which characterizes the atom discriminations of various elements at the ion emission, and $F_{prib.}$ is the instrument factor, which is connected with the ions separation according to their mass and their registration.

A great number of works (see, for instance, [3–5]) show that the CEE magnitude can be determined experimentally by means of introducing into the sample being analyzed an internal standard with a given concentration. This permits one to decrease the systematic error, on average, by 20%. However, the manufacturing and certification of the standard specimens with consideration for the rigid requirements for their homogeneity that the MSSI should meet are extremely difficult; therefore, CEE determination by means of theoretical, empirical, or semiempirical expressions still remains urgent. At present, a great number of empirical expressions have been suggested, each of which is based on a certain mechanism of SI formation [6–9]. In order to make use of one or another expression for the CEE calculation, it is necessary to know the physical processes that underlie the SI formation basis. Therefore, nowadays, one of the major issues of mass spectrometry of solid substances is the solution of the problem of a standard-free analysis. In this connection, preliminary knowledge of the CEE magnitudes for the elements that

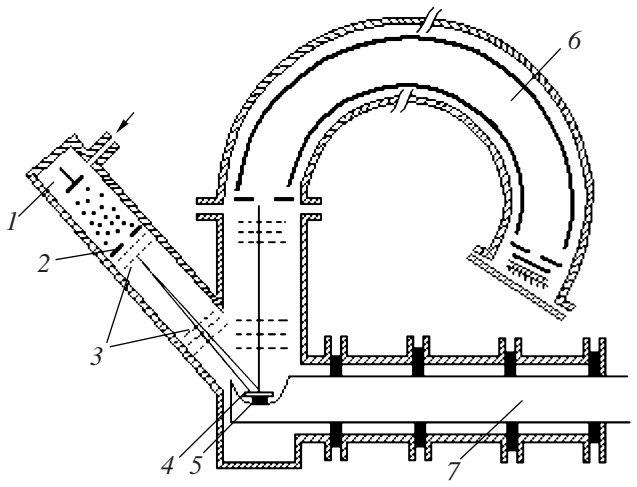

Fig. 1. Experimental device.

form the investigated sample, in our opinion, is of certain interest.

In this work, there has been made an attempt to create a CEE catalogue for a wide range of elements on the basis of experimental results. The existence of such a catalogue for some energy ranges and primary ion currents, as it seems to us, will enable reduction of the systematic error occurring in the process of the analysis of a solid substance using the MSSI method.

THE EXPERIMENT CONDITIONS

The experiments were carried out on the device whose scheme is presented in Fig. 1. The primary ions with 1.5–5.5 keV of energy and with a 0.1–0.5 mA/cm^2 ion flow density were extracted from of the plasma (1) of a glow discharge in argon (oxygen, xenon) through the aperture in the cathode (2), accelerated, focused by means of the ion-optical system (3) located behind the cathode, and directed onto the sample (4) at an angle of 45° with respect to the perpendicular of the sample surface. The secondary ions were gathered by an extracting grid (5), which was supplied by the pulse voltage in accordance with the target with a duration of 10^{-7} s. Such a regime of the experimental device operation permitted us to obtain at the source outlet a cluster of primary ions with divergence of 1–2°. As an ion analyzer, there was used a time-of-flight mass spectrometer with an axially-symmetric electric field (6), which allowed us to focus the ions according to the energy and angle of divergence. The necessity of making use of the above analyzer is accounted for by the fact that the secondary ions emitted from the sample surface have a comparatively greater (over 5%) divergence of the initial energies.

One should note that, actually, any kind of ion sources can be used as an ion gun. A major requirement that an ion gun should meet is a great magnitude of the ion current, and, since the secondary-emissive mass spectra little depend on the divergence of the bombarding ions, their divergence within a range of 10–20% is quite allowable.

For rapid installation or replacement of the specimens, there has been used a high-vacuum fast-operation lock (7) [10], permitting one to mount or shift the specimens without upsetting the high vacuum (10^{-4} Pa) at the ion source. Due to the experimental device, there has been performed heating of the samples up to 500–600°C in order to purify them of absorbed gases.

The analyzed specimen was mounted on a metal substrate (8) that was introduced through the vacuum lock into the ionization area. The target was heated by means of an electric heater.

In the preparation of the targets, their purity was the main concern. This is stipulated by the fact that the particles with energy of several kilo-electro-volts at colliding with the solid substance utterly lose their energy over a path length of several nanometers. It is the depth where the secondary ion formation occurs, and the presence of alien molecules on the surface may considerably distort the mass spectrum of the analyzed substance. The contamination of the target can happen in the mass spectrometer itself, as well as due to an insufficiently high vacuum (10^{-2} to 10^{-3} Pa) in the ionization area. The experiments showed that heating up the target to 500–600°C for 1–2 hours entirely purifies it from the absorbed molecules.

THE RESULTS OF THE EXPERIMENT

Fig. 2 presents typical mass-spectra oscillograms of certain metals. The insufficient reproducibility (up to 30%) of the results stipulated repeated bombardments. In Table 1, you can see the CEE calculated on the basis of the mass spectra of the most commonly used isotopes of 27 pure metals. The elements in the Table are arranged in the order of the CEE reduction. $^{56}Fe^+$ was selected as the external standard. Ar^+, O^+, and Xe^+ served as the bombarding ions.

The Table also presents the potentials of the first and second ionization of the elements being analyzed. The metals' CEEs presented in the Table allow one to reach a number of conclusions that are of interest from the practical point of view and are of great importance for the comprehension of certain peculiarities of the SI mechanism formation on the metal surface. Above all, it should be noted that the emission of the secondary ions is a structural-susceptibility phenomenon, since it depends on the structure and properties of the target material. This implies that, with regard to the nature of the target, the intensity of the ion emission (CEE) for various metals may differ by more than two orders.

As is seen from Table 1, the difference between the CRS magnitudes for various metals amounts to more than two orders at Ar^+ ion bombarding and to about three orders for O^+. This, indeed, is the cause of the range of efficiency of the analysis ($5 \cdot 10^{-6}$ to $5 \cdot 10^{-5}$%).

On the basis of the experimental data, there were built the CEE MSSI curves of the dependences on the atomization energy and ionization potential of the elements (Fig. 3). As one can see from the Figure, the dependence of the relative yield of ions X^+_{Fe} from the first ionization potential has a quadric character. The dependence of X^+_{Fe} upon the atomization energy (4) reflects the atomization processes (the rate and atomization energy) effect upon the SI relative yield. The greatest X^+_i is observed for the elements with the least ionization potential but with the greatest atomization energy.

It is of interest to compare the data of Table 1 with respect to the CEE change according to the arrangement of the elements in the periodic system. The investigations showed precise correlation for the elements located in one row. For the majority of metals (Mg, Zn, Al, Cd, Ti, Sn, and Pb) of one row, the CEE magnitude linearly reduces with the Z serial number increase. Moreover, the straight lines K^+_i (Z) for different groups are parallel.

Since the elements of one group of the periodic system are isoelectronic, i.e., they have an equal number of external electrons, the significant decrease of the SI relative yield with the Z increase should be explained by the influence of the internal shell structure on the emission process, and the distinctions observed for one period are obviously stipulated by the change of the electronic structure of the valent electrons.

The influence of the physicochemical primary ion properties on the coefficient of the secondary ionic emission is of positive interest for both theoretical and practical application. Owing to the importance of the problem, the dependence of the relative yield of ions of certain metals upon the nature of the bombarding ions was studied in the present work. In Table 2, one can see the CEE magnitudes calculated on the basis of the mass spectra of 27 metals obtained by MSSI at various energies of the primary ions (Ar^+, O^+, and Xe^+).

As is obvious from the Table, the SI yield of certain metals depends not only on the energy of the bombarding ions but also on their chemical properties. Thus, for instance, while the CEEs for Bi, Pt, Ag, and Au do not differ by an order of magnitude at Ar^+ or O^+ bombarding, for Al, V, and Ti, they differ by two orders.

Thus, the analysis of multiple investigation results indicates the presence of a large data discrepancy in the way of the coefficients of the secondary ion emission for similar elements at a range of energy of the bombarding ions. Since the direct comparison of the data is difficult, in this case, the only way to estimate the CEE of various elements is to compare them with similar characteristics of a commonly used isotope of one of the metals. The Table comprises ion relative intensities of various elements with respect to $^{56}Fe^+$ ion intensities. It is obvious that the difference of the relative yields of

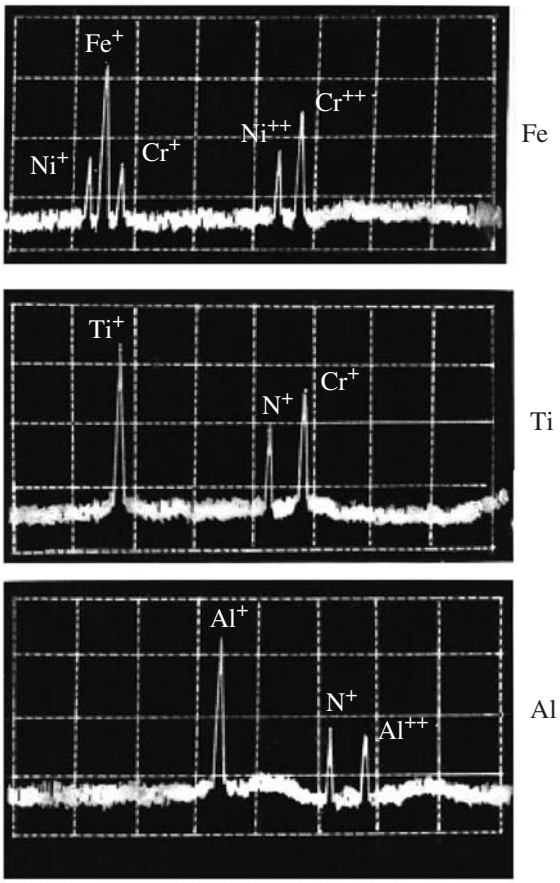

Fig. 2. Mass-spectra oscilograms of Fe, Ti, and Al.

one and the same metal amounts to more than one order (e.g., for Al^+, Mg^+, and V^+) considering the bombarding ions structure and to several times at the change of the bombarding ions energy.

It should be noted that the acquisition of reproducible results in the process of secondary ion investigations is not a trivial task. There was observed an influence of surface-active elements having a maximal affinity with oxygen and therefore displaying a pronounced tendency for the SIE changes with the change of the residual gas composition, i.e., the oxygen partial pressure. However, despite the data divergence, it is possible to reach a preliminary conclusion about the significant CEE change from element to element, which can amount to three orders in some cases. That is why, in order to attain proper results while making use of the proposed catalogue of elements for carrying out systematic investigations, it is necessary to maintain the constancy of the experimental conditions.

CONCLUSION

In conclusion, it is worth noting that the experimental CEE determination is a complicated task. Therefore, any available information on certain elements' discrim-

Table 1. Experimental magnitudes of the effective efficiency coefficient

Element	EEC			Potential ionization, eV	Atomization energy, eV
	Ar^+	O^+	Xe	φ_I	φ_a
Mg	11.4	86	131	7.644	1.15
Al	9.6	447	129	5.89	7.81
Nd	4.13	1.11	83	6.32	9.37
Y	2.87	5.12	72	6.58	4.43
V	2.75	200	122	6.74	3.36
Ga	2.28	13.2	83	6.00	2.08
Be	2.19	15.5	72	9.32	–
Mn	2.15	13.5	69	7.34	3.12
Ti	1.56	127	67	6.83	3.73
Co	1.22	5.97	48	7.86	4.62
Nb	1.16	35.6	41	6.77	3.53
Cr	1.01	41.6	34	5.76	–
Fe	1.00	15.8	25	7.88	6.35
Ni	0.98	1.42	20.3	7.63	5.23
Mo	0.39	25.2	14.1	7.18	7.28
Bi	0.36	0.46	2.5	8.32	–
Zr	0.29	27.2	7.2	6.93	–
Cu	0.26	1.26	3.1	7.72	7.94
W	0.187	5.83	3.0	7.98	7.91
Ta	0.186	5.43	5.03	6.0	6.73
Pt	0.11	0.125	2.3	8.96	6.83
Ag	0.108	0.135	1.71	7.84	4.32
Sn	0.94	0.558	1.02	7.35	2.63
Pb	0.86	1.22	0.95	7.85	2.83
Zn	0.44	0.908	0.63	9.42	1.32
Cd	0.291	0.108	0.55	9.93	2.33
Au	0.123	0.051	0.72	9.20	2.0

ination in the secondary emission, in our opinion, will be profitable for interpretation of solid substance mass spectra. The problem is that the CEE (regardless of the solid substance atom ionization method) is subjected to the influence of all the stages of the solid substance mass-spectrometric analysis. First of all is the physics

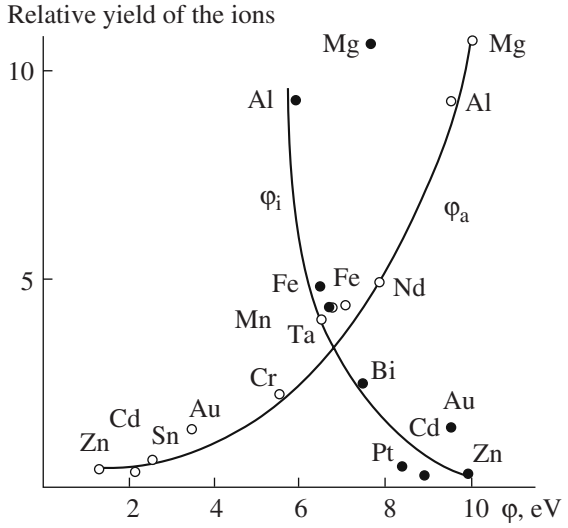

Fig. 3. Dependence of the ion relative yield on the potential of the first ionization [φ_I] and the atomization energy [φ_a].

Table 2

The bombarding ion energy $W = 2.0$ keV

Element	EEC			Element	EEC			Element	EEC		
	Ar^+	O^+	Xe		Ar^+	O^+	Xe		Ar^+	O^+	Xe
Mg	6.91	60.4	92.0	Co	0.77	3.92	19.2	W	0.121	3.71	1.91
Al	5.82	342	80.5	Nb	0.71	25.43	16..3	Ta	0.09	3.53	3.12
Nd	2.31	0.51	46.2	Cr	0.53	26.32	13.2	Pt	0.08	0.07	1.71
Y	1.92	29.8	15.6	Fe	0.41	8.12	11.0	Ag	0.071	0.08	0.92
V	1.70	148	60.2	Ni	0.18	2.93	10.3	Sn	0.060	–	0.73
Ga	1.23	7.03	56.5	Mo	0.17	16.8	8.7	Pb	0.03	–	0.69
Be	1.11	7.82	40.9	Bi	0.15	0.42	9.2	Zn	0.02	–	0.51
Mn	1.42	6.71	23.2	Zr	0.14	15.2	5.3	Cd	–	–	0.41
Ti	0.93	6.12	21.0	Cu	0.15	0.63	6.1	Au	–	–	0.21

$W = 3.0$ keV

Element	EEC			Element	EEC			Element	EEC		
	Ar^+	O^+	Xe		Ar^+	O^+	Xe		Ar^+	O^+	Xe
Mg	7.92	67.1	917	Co	0.81	4.83	45.5	W	0.132	4.02	4.3
Al	6.13	350	216	Nb	0.81	27.2	39.2	Ta	0.120	3.92	7.2
Nd	2.95	0.61	62.3	Cr	0.61	28.6	34.4	Pt	0.088	0.085	3.22
Y	2.02	39.2	27.3	Fe	0.52	9.18	23.7	Ag	0.16	0.102	2.4
V	2.21	152	26.7	Ni	0.48	3.62	21.6	Sn	0.61	0.357	1.3
Ga	1.83	8.75	66.5	Mo	0.27	18.7	19.7	Pb	0.052	0.94	1.1
Be	1.60	9.01	60.9	Bi	0.25	0.53	22.4	Zn	0.02	0.68	1.0
Mn	1.61	7.71	58.8	Zr	0.21	18.74	11.4	Cd	0.01	0.82	1.3
Ti	1.01	8.62	52.4	Cu	0.15	0.81	13.7	Au	0.01	0.03	1.1

$W = 4.5$ keV

Element	EEC			Element	EEC			Element	EEC		
	Ar^+	O^+	Xe		Ar^+	O^+	Xe		Ar^+	O^+	Xe
Mg	11.4	86.1	131	Co	1.22	5.97	48	W	0.187	5.83	3.0
Al	9.62	447.2	129	Nb	1.16	35.6	41	Ta	0.186	5.43	5.3
Nd	4.13	1.11	83	Cr	1.01	41.6	34	Pt	0.112	0.108	2.3
Y	2.87	5.12	72	Fe	1.00	15.8	25	Ag	0.108	0.135	1.71
V	2.75	200	122	Ni	0.98	4.42	20.3	Sn	0.094	0.558	1.02
Ga	2.28	13.2	83	Mo	0.39	25.2	14.1	Pb	0.086	1.22	0.15
Be	2.19	15.5	72	Bi	0.36	0.46	2.5	Zn	0.034	0.918	0.63
Mn	2.15	13.5	69	Zr	0.29	27.2	7.2	Cd	0.019	0.108	0.55
Ti	1.56	127	67	Cu	0.262	1.26	3.1	Au	0.012	0.051	0.72

$W = 5.5$ keV

Element	EEC			Element	EEC			Element	EEC		
	Ar^+	O^+	Xe		Ar^+	O^+	Xe		Ar^+	O^+	Xe
Mg	8.41	74.1	172	Co	1.01	5.73	65	W	0.179	4.91	6.0
Al	6.62	374	150	Nb	0.93	32.1	56	Ta	0.171	4.81	10.1
Nd	3.11	0.8	89	Cr	0.88	35.7	50	Pt	0.101	0.107	4.6
Y	2.21	47.1	81	Fe	0.81	12.1	41	Ag	0.93	0.121	3.41
V	2.23	170	160	Ni	0.78	4.07	35	Sn	0.87	0.441	2.04
Ga	1.91	11.2	95	Mo	0.35	21.7	31	Pb	0.81	1.02	1.9
Be	1.82	12.3	87	Bi	0.31	0.37	42	Zn	0.029	0.87	1.26
Mn	1.89	10.2	84	Zr	0.25	24.1	14	Cd	0.016	0.94	1.21
Ti	1.31	115	81	Cu	0.21	0.98	18	Au	0.040	0.03	1.44

of the processes, including the stages of atomization and ionization of various elements. Second is the discrimination of the ions in the analytical system and of the elements in the ion-optical system. In other words, the CEE should be considered as a result of the collective interaction of various processes. As seems to us, this will simplify the problem of theoretical and experimental CEE investigation, because, behind any type of discrimination, there is a definite physical process that submits to investigation.

REFERENCES

1. Beske, H.E. Zangew, Positive secondary Phys. 1962, vol. 14, p. 30.
2. Fainberg, V.S. and Ramendik, G.I., On Possibility of Describing the Relative Yield of Secondary Ions by Means of Quasi-Equilibrium Model in Mass Spectrometry, *Zh. Anal. Khim*., 1991, vol. 46, issue 2, pp. 241–252.
3. Newbury, D.E. and Simons, D., Secondary Emission of Molecular Ions from Light Elements Targets, SIMS - IV Proc. 4th Conf. Berlin, 1984. p. 101.
4. Ramendik, G.I., Manzon, B.M., and Tyurin, D.A., Quasi-Equilibrium Model of Ion Formation in Investigations of Spark and Laser Mass Spectrometry, *Zh. Anal. Khim*, 1989, vol. 4, pp. 996–1007.
5. Bensen, K.M., Surkin, P., Gilbers, R., and Adams, F., Secondary Ion Mass Spectromety Depth Profiling and Simultaneous Inactivation, *Spectrochim*. Acta, 1984, vol. 38, no. 5, pp. 843–861.
6. Teylor, S.E., and McLennon, S.M., Molecular Rearrangement Cluster Formation in the SIMS of Fluoride Salts, *Chem. Geol*. 1983, vol. 39, nos. 3 and 4, p. 273.
7. Ramkumar, K. L., Datta, B.P., and Kavimandan, V.D., On a Mechanism of Secondary Emission of Polyatomic Particles, *F. Z. Anal. Chem*, 1989, vol. 318, no. 1, p. 12.
8. Datta, B.P. and Yain, H.C., Focusing Errors of a Multiple-Focusing Time-of-Flight Mass Spectrometer with an Electrostatic Sector Fields, Int. *J. Mass Spectrum Ion Proc*., 1986, vol. 68, no. 3, p. 219.
9. Vos, L. and Van Cricken R., Cluster Induced Secondary Ion Emission, F. Z. *Anal. chem*., 1985, vol. 309, p. 32.
10. Sysoev, A.A. and Ivanov, V.P., High-vacuum Fast Operating Lock, *Prib. Tekh. Eksp*., 1995, vol. 55, no. 3, pp. 137–142.

ISSN 1068-3755, Surface Engineering and Applied Electrochemistry, 2008, Vol. 44, No. 2, pp. 165–168. © Allerton Press, Inc., 2008.
Original Russian Text ©B.Eshpulatov, E.U. Arzikulov, 2008, published in Elektronnaya Obrabotka Materialov, 2008, No. 2, pp. 105–109.

OPERATING EXPERIENCE

Pinning Structure of Dimensional Phonon Resonance in Quantum Wires

B. Eshpulatov[a] and E. U. Arzikulov[b]

[a] *Tashkent University of Information Technologies, Samarkand Branch, ul. Shorukh mirzo 47A, Samarkand, 140104 Republic of Uzbekistan*

E-mail: eshkuvat@samdu.uz

[b] *Navoi State University, Samarkand, Universitetskii bul'var 15, Samarkand, 140104 Republic of Uzbekistan*

Received November 21, 2007

Abstract—The dimensional phonon resonances in dimensionally-quantum semiconductor wires are considered. It is supposed that the absorption of light is caused by electron transitions between dimensionally–quantum subbands in potential wells with the participation of long-wavelength phonons. The influence of resonance electron–phonon interaction on a spectrum of one-dimensional electrons in quantum wires is investigated. It is shown that the spectrum contains two branches and also the splitting of the peak of the dimensional phonon resonance into two components; the distance between them is determined by the resonance electron–phonon interaction.

DOI: 10.3103/S1068375508020154

INTRODUCTION

Over the period of the last decades, optical methods have been widely used for investigation of the electron properties of low-dimensional systems [1–2].

Therefore, the study of the optical phonon influence on the properties of electrons in quantized semiconductor wires in the case when the electron–phonon interaction strongly alters the absorption frequency dependence appears to be relevant. One of these effects is the dimensional phonon resonance [3–4], whereby the light absorption is due to electron transitions between dimensionally quantized levels in quantized semiconductor wires with LO-phonon participation.

If the difference of the energy between the dimensionally quantized levels taking part in the optical transition is close to the energy of the optical LO-phonon, there appears a resonance coupling between the dimensionally quantized levels, which may lead to pinning effects [4].

In the present work, the theory of the form of the dimensional phonon resonance line in dimensionally quantized semiconductor wires at fulfillment of the above indicated conditions is developed.

PROBLEM FORMULATION AND BASIC RELATIONS

Below, there are considered dimensionally quantized wires with the length L and the cross sectional area $a \times d$, where a is the Y-direction width and d is the Z-direction width. The semiconductor is assumed to be of cubic syngony and the electron dispersion law to be parabolic. The temperature and the concentration of electrons are supposed to be sufficiently low so that only the lower dimensionally quantized level is occupied and the optical LO-phonons are not excited.

In the considered approximation, the wave function and the electron energy have the form

$$\Psi(x, y, z) = \left(\frac{4}{adL}\right)^{1/2} e^{ik_x x} \sin\left(\frac{\pi n}{a} y\right) \sin\left(\frac{\pi m}{d} z\right), \quad (1)$$

$$\begin{aligned} \mathrm{E}_\gamma(n, m, k_x) &= \frac{\pi^2\hbar^2}{2m^*a^2} n_\gamma^2 + \frac{\pi^2\hbar^2}{2m^*d^2} m_\gamma^2 \\ &+ \frac{\hbar^2 k_{xy}^2}{2m^*} = \hbar\omega_\gamma, \end{aligned} \quad (2)$$

where m^* is the effective mass of the electron; m and n are the whole numbers indexing the levels of the dimensional quantization in the state γ; and k_x is the continuous quantum number.

Interaction of the electron in the dimensionally quantized semiconductor film with bulk LO-phonons is described by the Hamiltonian

$$H_{\mathrm{int}} = \sum_{\alpha\alpha'\vec{q}} [C_{\vec{q}} I_{\alpha\alpha'}(\vec{q}) \cdot b_{\vec{q}} + э.с.] \cdot a_\alpha^+ a_{\alpha'}; \quad (3)$$

$$\begin{aligned} C_{\vec{q}} &= -i(\hbar\omega_0)[4\pi\alpha_0 l_0^3/V]^{1/2} (l_0 q)^{-1}, \\ l_0 &= \hbar/(2m^*\omega_0)^{1/2}; \end{aligned} \quad (4)$$

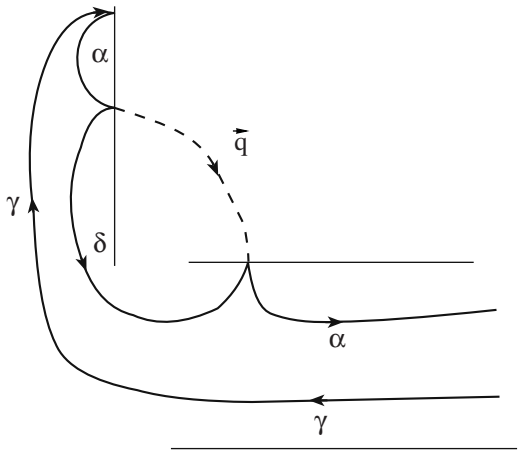

Fig. 1. Simplest graph of the angular part responsible for dimensional-phonon absorption.

$$I_{\alpha\alpha'}(\vec{q}) = \delta(k_{x\alpha'} - k_{x\alpha} + q_x) C_{\alpha\alpha'}(q_y) C_{\alpha\alpha'}(q_z). \quad (5)$$

Here, ω_0 is the frequency of the optical LO-phonon; $k_{x\alpha}$ is the similar wave vector of the electron (along the wire axis) in the state α; q_x, q_y, and q_z are the *OX*–, *OY*–, and *OZ*–components of the wave vector of the phonon $\vec{q}$, respectively; $b^+_{\vec{q}}$, $b_{\vec{q}}$, a^+_α, and $a_{\alpha'}$ are the phonon and electron operators of creation and annihilation; and α_0 is the dimensionless constant of the electron–phonon interaction. $C_{\alpha\alpha'}(q)$ are given in paper [5] and, due to their bulkiness, the expressions are not presented here.

For calculation of the absorption, let us apply the method developed in [6]. In the case of the normal incidence of the electromagnetic wave of the *S*-polarization (from the range of $z < 0$ into the range of $z > 0$, *OXZ* incidence plane) on the wire, for the function $\alpha(\omega, 0)$ determining the frequency dependence of absorption, we obtain

$$\alpha(\omega, 0) = \frac{8\pi e^2}{\sqrt{\varepsilon_\infty} m_0^2 c a L \hbar^2} \sum_{\substack{\alpha\gamma \\ \delta\vec{q}}} |N_{\alpha\gamma}|^2 \times \mathrm{Re} \frac{-i n_\gamma |C_{\vec{q}}|^2 |I_{\alpha\delta}(\vec{q})|^2}{\omega_{\alpha\gamma}(\omega_{\alpha\gamma} + \omega_0)[S + i(\omega_{\delta\gamma} + \omega_0)]}; \quad (6)$$

$$|N_{\alpha\gamma}|^2 = \frac{32 n_\alpha^2 n_\gamma^2}{(n_\alpha^2 - n_\gamma^2)^2} [1 - (-1)^{n_\alpha + n_\gamma}], \quad S = -i\omega + \sigma, \quad \sigma \longrightarrow +0. \quad (7)$$

Here, ω and c are the frequency and velocity of light in vacuum, m_0 is the free electron mass, ε_∞ is the high-frequency dielectric constant of the semiconductor, and n_γ is the function of the distribution of the electrons in the γ state. At derivation of (6), there was taken into account the simplest graph (Fig. 1).*

DIMENSIONAL PHONON RESONANCE

Let us consider the electromagnetic wave absorption caused by the electron transitions into the one-dimensional band with $n = 2$ with simultaneous LO-phonon emission assuming that $m = n_\gamma = 1$.

Transiting in (6) from summation over $\vec{q}$ to integration and integrating over q_y and q_z, we obtain

$$\frac{\alpha(\omega, 0)}{\alpha(0)} = \int_0^\infty n_1(t) dt \int_0^\infty du \ln[t^2 - 2tu + u^2] \delta(\Gamma + t^2 - u^2), \quad (8)$$

$$\alpha(0) = \frac{512\eta}{9\sqrt{\varepsilon_\infty}} \cdot \frac{e^2}{\hbar c} \frac{m^{*2}\omega_0^2}{m_0^2 \Omega(\Omega + \omega_0)}, \quad \Omega = \frac{3\hbar\pi^2}{2m^* a^2}, \quad (9)$$

$$\Gamma = \frac{[\omega - \omega_0 - \Omega]}{\omega_0}. \quad (10)$$

At low temperatures, $n_1(t)$ may be substituted by the step $n_1(t) = \theta(E_F - E_1 - \hbar\omega_0 t^2)$, where $\theta(x)$ is the Heaviside function, and $E_F - E_0 = \dfrac{\hbar\pi^2 N_0^2}{32m^*}$.

Thus, integral (8) is truncated by $t_0 = \left[\dfrac{\hbar\pi^2 N_0^2}{32m^*\omega_0}\right]^{1/2}$, so that

$$\frac{\alpha(\omega, 0)}{\alpha(0)} = \int_0^{t_0} \frac{dt}{\sqrt{\Gamma + t^2}} \ln[\Gamma + 2t^2 - 2t\sqrt{\Gamma + t^2}], \quad \Gamma > 0, \quad (11)$$

$$\frac{\alpha(\omega, 0)}{\alpha(0)} = \int_{\sqrt{|\Gamma|}}^{t_0} \frac{2dt}{\sqrt{t^2 - |\Gamma|}} \ln\left[t - t\sqrt{1 - \frac{|\Gamma|}{t^2}}\right], \quad \Gamma < 0, \quad (12)$$

and $\alpha(\omega, 0) = 0$ if $\sqrt{|\Gamma|} \geq t_0$. Using the asymptotic decomposition, by the expression under the integral sign, it can be shown that, at $\Gamma \longrightarrow 0$, the absorption contains a logarithmic singularity; that is,

$$\frac{\alpha(\omega, 0)}{\alpha(0)} \sim \ln|\Gamma|. \quad (13)$$

If $\Gamma \gg t^2$, then, as follows from (11),

$$\frac{\alpha(\omega, 0)}{\alpha(0)} \cong \frac{t_0}{\Gamma}. \quad (14)$$

* From now on, the terminology and graph technique presented in [7] are used.

RESONANCE ELECTRON–PHONON INTERACTION

Let us assume that $E_2 - E_1 \approx \hbar\omega_0$, and $\omega = 2\omega_0$. Then, the electromagnetic wave energy is consumed by the electron transfer to the upper level and by the LO-phonon creation. Since the distance between the levels is equal to the phonon energy, there appears a resonance coupling between the levels due to the real electron transfer to the lower level with the phonon emission. This interaction removes degeneration of levels of the electron–phonon system (the level $n = 2$ and the level $n = 1$ plus phonon), and this leads to the appearance of two spectrum branches. In this case, as can be seen from (13), the simplest graph (Fig. 1) logarithmically diverges at the frequency $\omega = 2\omega_0$; this means divergences of the higher-order graphs for the angular part. Summation of the perturbation theory series over the electron–phonon interaction leads, as a rule, to substitution of the value

$$[S + i(\omega_{\delta\gamma} + \omega_0)] \text{ on } [S + i(\omega_{\delta\gamma} + \omega_0) - W].$$

As is shown in [4], the "outgoing" terms of the kinetic equation are small; therefore, they may be disregarded.

a) Analysis of the perturbation theory series for the function W.

The function W determining the absorption behavior in the resonance region is a sum of irreducible graphs, wherein phonon lines are situated on the upper horizontal section to the left of the external phonon line (Fig. 1).

In the case $\omega = 2\omega_0$, it suffices to be restricted to the simplest graph (Fig. 2a).

It is in accord with

$$W_a = \sum_{\delta_1, \vec{q}} \frac{(i\hbar)^{-2}\left|C_{\vec{q}_1}\right|^2 \left|I_{\delta\delta_1}(\vec{q}_1)\right|^2}{S + i(\omega_{\delta_1\gamma} + 2\omega_0)}. \quad (15)$$

Using the expression for the matrix element, we obtain

$$W_a = -\frac{i\alpha_0\omega_0}{2\pi^2} \times \int_{-\infty}^{+\infty} d\vartheta \int_{-\infty}^{+\infty} dx \int_{-\infty}^{+\infty} dy \frac{|C_{21}(y)|^2 |C_{11}(x)|^2}{(u^2 - 2u\vartheta + \vartheta^2 + x^2 + y^2)} \times [\Gamma + \lambda + t^2 - \vartheta^2 + i\delta]^{-1}, \quad (16)$$

where $\lambda = \dfrac{[\Omega - \omega_0]}{\omega_0}$.

In calculation of the integral over ϑ in (16), it is possible (with an accuracy to the $\alpha_0^{1/3}$ order terms) to neglect the dependence on u and ϑ in the multiplier $(u^2 - 2u\vartheta + \vartheta^2 + x^2 + y^2)$, whereupon the integral can be easily calculated and

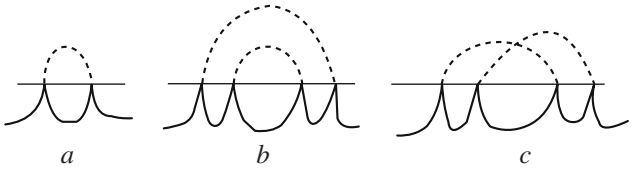

Fig. 2. Graphs renormalizing the upper electron line in the angular part.

$$W_a = -\frac{4\alpha_0\omega_0}{3}[\Gamma + \lambda + t^2]^{-1/2}. \quad (17)$$

b) Frequency dependence of the absorption.

In order to obtain the frequency dependence of the absorption, $[S + i(\omega_{\delta\gamma} - \omega_0)]$ should be substituted by $[S + i(\omega_{\delta\gamma} - \omega_0) - W]$ in (6). As a result, we obtain

$$\frac{\alpha(\omega, 0)}{\alpha(0)} = \begin{cases} \dfrac{\pi}{\sqrt{f_1(\Gamma)(\Gamma + \eta^{2/3})}} \cdot -\eta^{2/3} \le \Gamma \le 0; \\ \Gamma \le -\eta^{2/3}; \\ \dfrac{\pi f_2(\Gamma)}{\left\{\left(\Gamma - \dfrac{\eta^{2/3}}{2}\right)^2 + \dfrac{3}{4}\eta^{4/3}\right\}^{1/2}} \cdot \Gamma > 0; \end{cases}, \quad (18)$$

$$\text{where} \quad \eta = \frac{4\alpha_0}{3}, \quad f_1(\Gamma) = \frac{\Gamma^2 - \eta^{2/3}\Gamma + \eta^{4/3}}{\Gamma^2 + \eta\sqrt{-\Gamma}}, \quad f_2(\Gamma) = \left(\frac{\sqrt{\Gamma^4 + \eta^2\Gamma + \Gamma^2}}{2(\Gamma + \eta^{2/3})}\right)^{1/2}. \quad (19)$$

One can see from the given formulae that the dimensional phonon resonance line splits into two maxima situated at the points $\Gamma_1 = -\eta^{2/3}$ and $\Gamma_2 = \frac{1}{2}\eta^{2/3}$ as in the case of the magnetooptic absorption in bulk semiconductors [8].

These two maxima correspond to the two branches of the spectrum of the electron–phonon system. The spectrum is determined by the equation [8]

$$\varepsilon + \frac{i\eta}{\sqrt{\varepsilon + \lambda}} = 0,$$

which is obtained by setting to zero the denominator $[S + i(\omega_{\delta\gamma} - \omega_0) - W]$ and by substitution of W by W_a.

The above developed theory predicts splitting of the peak of the dimensional phonon resonance in the frequency range $\omega = 2\omega_0$ into two components, the distance between them being determined by the resonance electron–phonon interaction.

REFERENCES

1. Hang, H. and Koch, S.W., Quantum Theory of the Optical and Electronic Properties of Semiconductors, World Scientific, 1993.
2. Vorob'ev, L.E., Ivchenko, E.L., Firsov D.A., and Shalygin, V.A., Opticheskie svoistva nanostruktur (Optical Properties of Nanostructures), St. Petersburg: Nauka, 2002.
3. Bass, F. and Matulis, A.Yu., Dimensional Phonon Jumps of Light Absorption in Semiconductor Films, *Fiz. Tverd. Tela* (Leningrad), 1970 vol. 12, pp. 2039–2043.
4. Korovin, L.I. and Eshpultov, B.E., Pinning Structure of Dimensional Phonon Resonance in Inversion Layers, *Fiz. Tverd. Tela* (Leningrad), 1981, vol. 23, no. 10, pp. 3056–3062.
5. Ridley, B.K., Quantum Processes in Semiconductors, Second edition, Oxford: Clarendon, 1988.
6. Korovin, L.I. and Eshpultov, B.E., Interband Magnetooptic Absorption of Semiconductor Surface Layer, *Fiz. Tverd. Tela* (Leningrad), 1979, vol. 21, pp. 3703–3712.
7. Konstantinov, O.V. and Perel', V.I., Graph Technique for Calculation of Kinetic Quantities, *Zh. Eksp. Teor. Fiz.*, 1960, vol. 39, pp. 197–210.
8. Korovin, L.I. and Pavlov, S.T., On Influence of Optical Phonons on Interband Magnetooptic Absorption in Semiconductors, *Zh. Eksp. Teor. Fiz*, 1967, vol. 53, pp. 1708–1718.